Vacuum Assisted Resin Transfer Molding (VARTM): Model Development and Verification

Xiaolan Song

Dissertation submitted to the Faculty of the

Virginia Polytechnic Institute and State University

in partial fulfillment of the requirements for the degree of

Doctor of Philosophy

in

Engineering Mechanics

Dr. Alfred C. Loos, Chairman

Dr. Donald G. Baird

Dr. Romesh C. Batra

Dr. Michael W. Hyer

Dr. Saad A. Ragab

April 14, 2003

Blacksburg, Virginia

Keywords: VARTM, Simulation, Resin Flow, Compaction of Preform

Vacuum Assisted Resin Transfer Molding (VARTM): Model Development and Verification

Xiaolan Song

(ABSTRACT)

In this investigation, a comprehensive Vacuum Assisted Resin Transfer Molding (VARTM) process simulation model was developed and verified. The model incorporates resin flow through the preform, compaction and relaxation of the preform, and viscosity and cure kinetics of the resin. The computer model can be used to analyze the resin flow details, track the thickness change of the preform, predict the total infiltration time and final fiber volume fraction of the parts, and determine whether the resin could completely infiltrate and uniformly wet out the preform.

Flow of resin through the preform is modeled as flow through porous media. Darcy's law combined with the continuity equation for an incompressible Newtonian fluid forms the basis of the flow model. During the infiltration process, it is well accepted that the total pressure is shared by the resin pressure and the pressure supported by the fiber network. With the progression of the resin, the net pressure applied to the preform decreases as a result of increasing local resin pressure. This leads to the springback of the preform, and is called the springback mechanism. On the other side, the lubrication effect of the resin causes the rearrangement of the fiber network and an increase in the preform compaction. This is called the wetting compaction mechanism. The thickness change of the preform is determined by the relative magnitude of the springback and wetting deformation mechanisms. In the compaction model, the transverse equilibrium equation is used to calculate the net

compaction pressure applied to the preform, and the compaction test results are fitted to give the compressive constitutive law of the preform. The Finite Element/Control Volume (FE/CV) method is adopted to find the flow front location and the fluid pressure. The code features the ability of simultaneous integration of 1-D, 2-D and 3-D element types in a single simulation, and thus enables efficient modeling of the flow in complex mold geometries.

VARTM of two flat composite panels was conducted to verify the simulation model. The composite panels were fabricated using the SAERTEX multi-axial warp knit carbon fiber fabric and SI-ZG-5A epoxy resin. Panel 1 contained one stack of the carbon fabric, and Panel 2 contained four stacks of the fabric. The parameters verified included the flow front location and preform thickness change. For Panel 1, the flow front locations were accurately predicted while the predicted resin infiltration was much slower than measured for Panel 2. The disagreement is attributed to the permeability model used in the simulation, which failed to consider the interface flow in the unstitched preform containing more than one stack of the fabric under very low compaction force. The predicted transverse displacements agree well with the experimental measurement qualitatively, but not quantitatively. The reasons for the differences were discussed, and further investigations are recommended to develop a more accurate compaction model.

The simulation code was also used to investigate the VARTM of a new form of sandwich structure with through-the-thickness reinforcements, which is being considered for use in primary aircraft structure. The infiltration of three foam core sandwich preforms with different stitch densities was studied. The objective of the study was to determine whether the preforms could be completely infiltrated and how the stitch density affects the infiltration process. The visualization experiments were conducted to verify the simulation. The model accurately predicted the resin infiltration patterns. The calculated filling times underpredicted experimental times by 4 to 14%. The model revealed the resin flow details and found that increasing the stitch spacing shortens the total filling time, but increases the nonuniformity of the flow front shape. Extreme nonuniformity of the flow front shape could result in the formation of the voids.

Dedication

To my parents, for their dedication and inspiration

Acknowledgments

First, I would like to express my gratitude and appreciation to my advisor Dr. Alfred Loos for his invaluable guidance and generous financial support throughout my Ph.D. studies. I would like also to thank my committee members, Dr. Donald Baird, Dr. Romesh Batra, Dr. Michael Hyer, and Dr. Saad Ragab, for their time and expertise. It is an honor to have worked with and learned from them.

I would like to thank NASA Langley Research Center for funding the research presented. It has been a very pleasant experience to work with Mr. Brian Grimsley, Dr. Pascal Hubert, and Mr. Roberto Cano from NASA Langley. Mr. Brian Grimsley performed the VARTM experiments using the SAERTEX carbon fabric and the SI-ZG-5A epoxy resin. I would also like to thank Dr. Jay Sayre for his help in training, and Ms. Rebecca McGrane for providing the experimental results for the VARTM of the sandwich panels.

I would like to thank my boyfriend, Dr. Hsu-Kuang Ching, for his love and encouragement. His pleasant personality has made my life joyful.

Most importantly, my deepest thanks go to my parents, Dakai Song and Jihua Xu, for their dedication and inspiration that enabled me to reach this milestone in my life. I also appreciate the continuous love and support from my sister, Rui Song.

Contents

List of Figures

List of Tables

Chapter 1

Introduction

The Resin Transfer Molding (RTM) process is a cost-effective fabrication method for the manufacture of polymer composites. In a traditional RTM process, catalyzed thermosetting resin is injected into an enclosed metal mold containing a previously positioned reinforcement preform. The preform is compacted to the specified fiber volume fraction when the matched metal mold is closed. The resin wets out the fiber until the mold is filled, and the part is then cured inside the mold. A schematic diagram of the process is shown in Fig. 1.1.

RTM offers several advantages over other composite fabrication methods such as autoclave and compression molding of prepreg tape laminates. First, high fiber volume fraction composites can be fabricated with low void contents. Second, parts with highly complex shapes can be molded by incorporating many components into a single preform. This helps to reduce the cost and weight of the structure. Third, hand lay-up of prepreg tape is eliminated. Production rates are increased and operating costs are reduced. Finally, RTM is a closed mold process that reduces the workers' exposure to harmful volatiles, i.e., styrene, associated with many of the room temperature processing resins. However, the matched metal tooling used in the RTM procedure is expensive, and the tooling design becomes difficult when fabricating large and complex shaped parts.

**Press or Clamps to Hold
Halves of Tool together**

Mold Tool

**Resin
Injected
under
Pressure**

**Optional
Vacuum
Assistance**

Mold Tool

**Dry
Reinforcement
Preform**
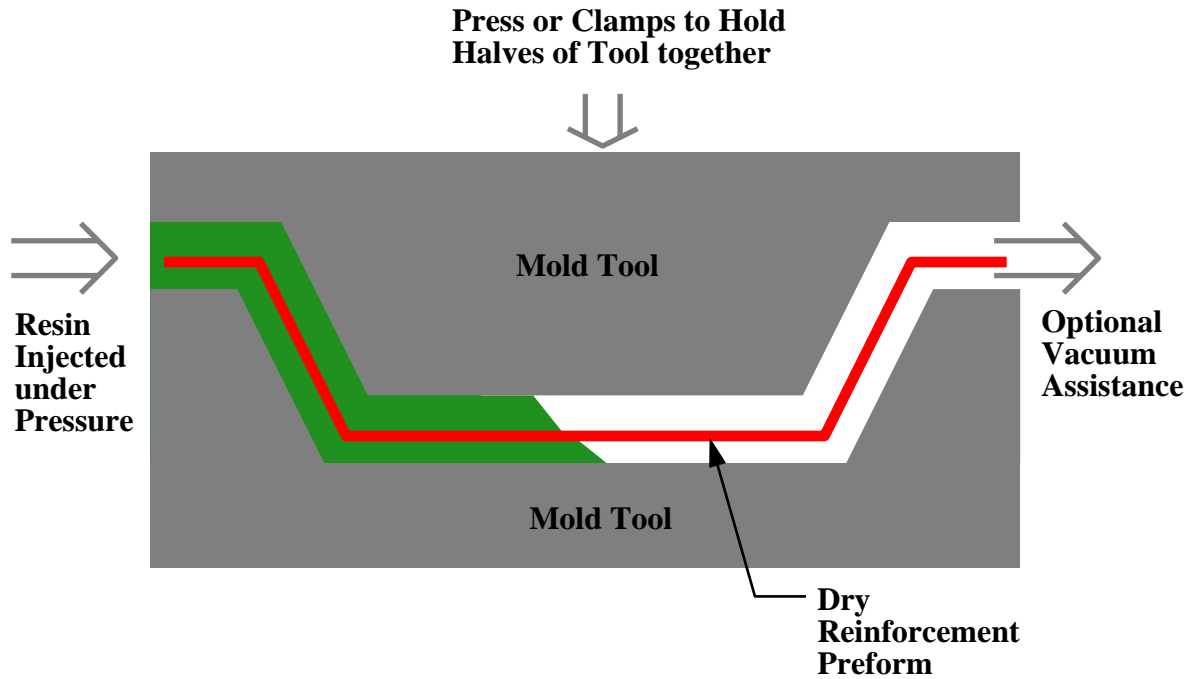
Figure 1.1: RTM processing schematic diagram

Vacuum Assisted Resin Transfer Molding (VARTM) has been developed as a variant of the traditional RTM process to reduce the cost and design difficulties associated with large metal tools. In VARTM, the upper half of a conventional mold is replaced by a vacuum bag. This eliminates the need for making a precise matched metal mold as in the conventional RTM process. Fig. 1.2 shows a generalized schematic diagram of the VARTM process. First, the vacuum pump is turned on to expel air from the preform assembly. After the system has been equilibrated and all air leaks have been eliminated, the resin is allowed to flow into the preform. A pressure of 1 atm provides both the driving force for the resin to impregnate the reinforcement and the compression force to compact the preform to the desired fiber volume fraction. The vacuum is left on until the resin has completely gelled. The part may then be cured at room temperature or in an oven. Due to the low injection pressure (1 atm), a resin distribution medium with high permeability is often incorporated into the vacuum bag lay-up to facilitate the resin flow in the preform. Because the distribution medium provides a low resistance resin pathway, the resin easily fills the distribution medium, and then leaks
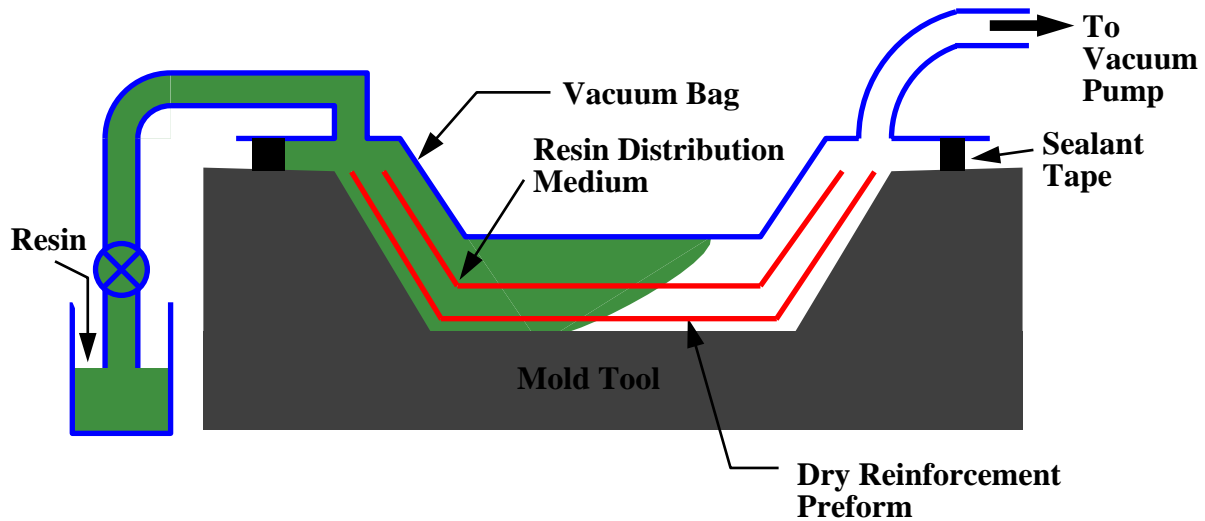
Figure 1.2: VARTM processing schematic diagram

downward and wets the preform out. The use of distribution medium reduces the processing time significantly, and ensures complete wet-out of the preform.

VARTM offers numerous cost advantages over traditional RTM, such as lower tooling cost and shorter start-up time. Because the top half of the tool is a flexible vacuum bag, a matched metal mold is no longer required. This makes VARTM attractive for the manufacture of large-scale components. Along with the advantages, VARTM also has inevitable disadvantages. It is a relatively complex process to perform well. The flexible nature of the vacuum bag makes it difficult to control the final thickness of the preform, and thus, the fiber volume fraction of the composite.

Due to the complex nature of the VARTM process, the trial and error method is inefficient and expensive for the process design and optimization. The objective of this study was to develop and verify a comprehensive VARTM simulation model as a cost effective design tool. The model includes three submodels: the viscosity and cure kinetics of the resin, the resin flow in the porous reinforcement preform, and the compaction of the preform during the infiltration procedure. The modeling software, 3DINFIL 5.0, has been developed to analyze the flow details, track the thickness change of the preform, predict the total infiltration time

and final fiber volume fraction of the parts, and determine whether the resin completely infiltrates and uniformly wets out the preform. The accuracy of the model was verified by comparing experimental results from VARTM of flat preforms and sandwich structures with model predictions.

A review of recent research in modeling of the VARTM procedure is presented in Chapter 2. Chapter 3 details the resin viscosity and kinetics, flow, and preform compaction models. The numerical technique used for the flow model, the finite element/control volume (FE/CV) method is discussed in Chapter 4. Comparisons between the model predictions and experimental results are shown in Chapter 5 and Chapter 6. Conclusions and recommendations for future work are given in Chapter 7.

Chapter 2

Literature Review

2.1 Resin Flow

Complete filling of the mold with adequate wetting of the fibrous media is the primary objective in resin transfer molding (RTM) and vacuum assisted resin transfer molding (VARTM). Incomplete impregnation of the reinforcement preform results in expensive defective parts, which must be scrapped. Therefore, the simulation of the resin flow through the preform is an important step in modeling these composites manufacturing processes to ensure that the process can be finished before the resin gels. Simulation codes can be used to track flow fronts and estimate the fill times. Modeling the resin flow during the impregnation processes provides insight into the process physics and highlights potential problems before production. In addition, flow prediction enables optimization of the process variables, such as vent location, and injection port location and type.

Many computer models have been developed to simulate the mold filing process in RTM. All these studies treat the propagation of the resin through the reinforcement preform as an incompressible fluid through a porous media. Darcy's law is used to describe the flow. Darcy's law in conjunction with the continuity equation forms the basis for the numerical

simulation of the infusion process. Different numerical techniques have been used to model this flow, such as finite difference method [1, 2], boundary element method [3], and finite element method [4–11]. Of these, the Finite Element/Control Volume (FE/CV) method has been widely used because of the lower computational cost. In this approach, the mold is first discretized into finite elements. A control volume is constructed around each node by subdividing the elements into smaller volumes. The pressure distribution in the resin filled region is obtained by use of the finite element method and Darcy's law is applied to calculate the flow rates. The concepts of the control volume and fill factor are then employed to track the location of the flow front [4]. The advantages of FE/CV method is that the flow simulation for complex geometries can be done rapidly and efficiently without the need of remeshing the resin-filled domain.

Most RTM processes deal with parts of a shell-like geometry. Because the part thickness is much smaller than its other dimensions, resin flow in the thickness direction has been neglected and two-dimensional RTM flow models have been developed by several independent research groups [5–7]. The calculated domain is a three-dimensional (3D) geometry, but the flow in the thickness direction is neglected, therefore these models are often called $2\frac{1}{2}$-dimensional ($2\frac{1}{2}$D) flow models. The major advantage of the $2\frac{1}{2}$D model is that the computational cost can be greatly reduced with acceptable simulation accuracy achieved.

Bruschke and Advani [6] created a two-dimensional FE/CV model to predict the resin flow pattern for mold filling in anisotropic media. A key feature of the simulation is the ability to model the influence of non-isothermal permeability of the fiber preform on the filling process. The results of the simulation are compared with experiments performed in a flat rectangular mold. A Newtonian fluid was injected into the mold at the center with the pressure at the inlet held constant. Four sets of experiments were conducted. In the first set of experiments, a lay-up of nine unidirectional mats with [0, ±45, 90, 0, 90, ∓45, 0] orientations was resin infused to study the effect of stacking layers with different orientations. The second set of experiments used a round insert to observe the influence of geometric complexity on the flow field. In the third set of experiments, the preform consists of two pieces of unidirectional

mats put together. The local permeability at the interface between the pieces is different from the bulk material and the preform becomes non-homogeneous. The interface between the pieces was called the cutline. This set of experiments was designed to investigate the influence of local non-homogeneity along the cutline. The last set of experiments examined the resin flow in a mold with two different gap-heights. In all the experiments, the upper half mold tool plate was made of glass for the purpose of flow visualization. The flow front locations were recorded on video tape to compare with the numerical results. In most cases, the predicted and experimental flow front corresponded well. However, the flow fronts in the experiment moved faster along the mold walls and the cutline. This showed the existence of low-resistance flow paths at these locations. This phenomenon is called race-tracking.

In most RTM process, resins injected into the mold cavity are highly reactive. The resin kinetic and viscosity changes during the infusion process are significant and need to be considered in the mold filling simulation. A computer simulation package including resin flow, heat transfer and chemical reaction based on the FE/CV method was developed at the Ohio State University [7, 8]. It can be used to simulate a two-dimensional non-isothermal molding process.

Calhoun et al. [9] conducted experiments at the Dow Chemical Company to verify the RTM flow model developed at Ohio State University. The experiment design was completely decoupled from the model development to eliminate any possible bias. Rectangular panels were injected using RTM process. Two different injection schemes were studied. The first scheme was designed to form a one-dimensional flow with a line source on one end of the panel and a line sink on the other. The second flow scheme used runners around the preform edge to produce a converging flow front to a point sink at the center. In the experiments, pressure transducers were used to monitor the pressure change during the infusion procedure at different locations in the preform. It was found that the mold filling time could be predicted within experimental error but the pressure distribution needed to be scaled to match the experiment data. The difference between experiment and simulation was likely due to the local variations of the preform permeability. It was also demonstrated that the

flow modeling was extremely sensitive to the preform porosity and permeability. The race-tracking phenomenon was observed in the one-dimensional flow experiment and different edge permeabilities were tried to simulate the phenomenon. When the edge permeability was set to be 100 times the bulk permeability, the simulated and experimental pressure profiles agreed well with each other.

Two-dimensional flow models work well to simulate the infusion of parts with small thickness. However, thicker parts require extensive resin flow through the thickness and thus the three-dimension effect in the mold filling process must be considered. Lim and Lee [10] developed a computer code to simulate the three-dimensional RTM mold filling process, including the temperature and cure effects. The validity of the numerical code was verified using simple problems with analytical solutions known. Experiments were also performed to further validate the numerical results. In the experiment, a cubic shaped preform was injected from the inlet gate at the center of the bottom surface. An optical fiber was used to monitor the resin flow inside the thick preform. The simulated resin flow front location as a function of time was compared with the experimental data. The agreements were found to be satisfactory. Numerical simulations for the filling process of complex geometries, such as an automobile headlamp bezel with a membrane and centrifugal pump casing, were done to illustrate the effectiveness of the numerical code.

In order to model the infusion process for a variety of conditions of industry interest, such as runner distribution systems, shell geometries, and 3-D flows, Phelan [11] developed a computer simulation model which incorporated a variety of element types. The model featured the ability of simultaneous integration of 1-D, 2-D, and 3-D element types in a single simulation. The model used the Flow Analysis Network (FAN), which is referred as FE/CV method by other researchers, to track the movement of the flow front. The model predicted the flow front position as a function of time and the pressure distribution during the filling process. The filling of a complex automotive part, the front-end structure of a Ford Escort was presented. The simulation proved to be a useful tool to quickly screen potential gating problem and control the pressure levels during the filling process.

Researchers have employed computer simulation models as a design tool to develop new injection schemes for the RTM procedure [12, 13]. Chan and Morgan [12] proposed a multiple port resin injection scheme to reduce the mold filling times. The ports were opened in sequence during RTM. A one-dimensional flow model was developed to illustrate the advantages of the proposed method. Results from the numerical study showed that the progressive opening of the injection gates reduced the filling time remarkably. Kang et al. [13] investigated two different multiple gate injection schemes. One is to open the gates in a sequential manner as the resin front advances. The other is to open all the gates simultaneously and control the pressures of each gate individually. Mold filling was simulated numerically using the FE/CV method. Experiments were conducted to verify the simulation results. The resin flow front shapes observed from the experiments compared well with the numerical results. Numerical simulation for the mold filling of the front panel of a tourist bus was performed to illustrate the efficiency of the proposed injection schemes. Both of the controlled multiple gate injection methods were proven to significantly reduce the injection time as well as to prevent the formation of air bubbles due to air entrapment.

The Finite Element/Control Volume (FE/CV) method has been successfully used to track resin flow in the RTM process. However, this popular numerical scheme also has some inherent drawbacks. First, the exact location of the flow front is difficult to determine as a consequence of the fixed mesh system. This ambiguity in the resin flow front location limits the accuracy of FE/CV method [14]. Mass conservation problems have also been reported with the use of this numerical approach [11, 15]. Researchers have addressed these numerical problems and put forward methods to improve the conventional FE/CV method [14, 16].

Kang and Lee [14] proposed a new algorithm, referred to as the Floating Imaginary Nodes and Elements (FINE) method, to get a smoother flow front and reduce the error in the pressure at the flow front of a FE/CV simulation of resin flow in a porous medium. With the FINE method, imaginary new nodes were added at the estimated flow front and the flow front elements were divided into two separate regions: the area of resin and the area of air. Thus, the flow front element was refined in an adaptive manner at each time step.

Two examples were studied to evaluate the validity of the FINE method. First, a square mold with a circular hole at the center was considered. Resin was injected from the center of the bottom edge of the square mold at a constant pressure. In the second case, resin was injected at constant flow rate into the square mold through a circular hole at the center. The simulations by the FINE method were compared with the analytical solutions and the numerical results by the conventional FE/CV method. It was shown that the FINE method improved the solution accuracy considerably with a marginal increase of the computational cost.

Violation of the law of mass conservation was reported with the use of the FE/CV approach. When the Galerkin formulation is used with isoparametric finite elements to obtain the pressure field, the balance of resin mass cannot be achieved [11]. A numerical model, 'the flow redefinition model', was proposed by Joshi et al. [16] to eliminate the problem. In the model, the intra-control volume and inter-control volume flow balances were enforced by arranging the control volumes in a descending order of their representative pressure and adjusting the outflow to match the inflow for all the control volumes in the same sequence. To validate the model, the authors studied the central injection mold filling problems where analytical solutions exist. Significant improvements in the fill time prediction were achieved using the flow redefinition model.

All the numerical simulations mentioned above use the conventional physics, which is based on Darcy's law and the continuity equation for the incompressible fluid. The flow of resin through the fiber packed mold cavity is modeled as the saturated flow of a Newtonian liquid through a single scale porous medium. However, it was noted that for the woven, stitched, or braided fiber mats, the preform behind the flow front was not fully saturated and the conventional physics is inadequate to simulate the resin impregnation process [17–19]. Simple, one-dimensional mold filling experiments were conducted with resin injected at a constant flow rate. In such experiments, it was found that the inlet pressure history deviated significantly from the linear plot predicted by the conventional physics. This anomalous flow behavior observed in the preforms made of the woven, stitched, or braided fiber mats was

attributed to the dual-scale medium with the presence of large gaps between dense fiber tows [17, 18].

A two layered model [20, 21] was proposed to simulate the unsaturated flow in woven fiber preforms. The movement of the resin through such fiber mats was modeled as the flows through the inter-tow and intra-tow pore spaces separately, and these flows were coupled by a sink term, which conserved the global mass. A dimensionless number, 'pore volume ratio', was proposed to quantify the strength of the 'sink' effect. The pore volume ratio was defined as the ratio of pore volumes in the fiber bundles and the gap regions between the bundles. The model recreated the non-linear drooping inlet pressure history of the woven mats obtained in the experiments. However, the effect of the dimensionless number proposed in the model, 'pore volume ratio', could not be validated empirically. The study of the unsaturated flow in the woven, stitched, or braided fiber mats is still in its infancy, and more research efforts are needed to advance this study [19].

Vacuum Assisted Resin Transfer Molding (VARTM) is a variant of traditional RTM process in which one of the solid tool faces is replaced by a flexible vacuum bag. The process is also named as Vacuum Bag Resin Transfer Molding (VBRTM), Vacuum Bag Molding (VBM), and Resin Infusion under Flexible Tooling (RIFT), etc. Williams et al. [22] reviewed the progress of VARTM from its first development as the Marco method in 1950 to the Seemann Composites Resin Infusion Manufacture Process (SCRIMP) today. A series of SCRIMP patents were awarded in the USA in the early to mid nineties [23–25]. The process is simple and resembles other vacuum infusion techniques in that the laminate is contained under a vacuum bag made of air impervious films such as nylon or silicone film, and resin is drawn in under vacuum. The novel aspect of SCRIMP is the use of patented resin distribution systems to facilitate mold filling and improve production efficiency. Generally, there are two types of resin distribution systems to facilitate the resin infusion in the SCRIMP process. One uses a distribution medium with high permeability placed on top of the fiber preform. The distribution medium is also referred to as the high permeability layer (HPL) or the high-permeable medium (HPM). Resin flows easily through the distribution medium

and then wets out the reinforcement preform from above. The use of a high-permeable distribution medium creates a transverse (i.e., top-to-bottom) flow in the fiber mat, which reduces the resin infusion time. The other type of SCRIMP uses grooves cut on a low-density core to distribute the resin. The preform is placed on top of the core and resin infuses the entire structure from the grooves. The core is part of the final product. The permeability of the grooves is much higher than that of the distribution medium, thus the part can be infiltrated more quickly. However, SCRIMP based on the distribution medium has attracted more attention in industrial applications and research investigations because of the ease to process and design flexibility.

Tari et al. [26] investigated the effect of the high permeability layer (i.e., distribution medium) on the resin flow field in VARTM through analysis, simulation and experiment. In the analysis, it was assumed that the shape of the flow front does not change as it travels down the mold. Fig. 2.1 shows a schematic diagram of the flow front associated with the use of a high permeability layer (HPL). In the flow front region, the pressure through the thickness of HPL was assumed constant and in the fiber mat, the flow in the in-plane direction was neglected compared to the transverse flow. For the flow front region, application of Darcy's law and the continuity equation to the flow in the HPL and fiber mat yielded a closed form solution for the flow front shape. Assuming no cross flow between the HPL and fiber mat in the region behind the flow front, the location of the flow front was solved as a function of time. The 2-D finite element model, RTMSIM developed at UCLA, was employed to simulate the resin flow in the cross-section parallel to the flow advancement. In the experiments, bi-directional fiber mats with different thicknesses were resin infiltrated in a rectangular Plexiglas mold. A commercially available loose weave nylon cloth was used as the HPL. The side and top views of the flow front were recorded using two video cameras. The experiment results validated the assumption that the flow front shape does not change during the mold filling procedure. The numerical simulation gave accurate results as to the shape of the flow front. The resin flow in the HPL led the flow in the fiber mat. The lags observed experimentally were compared to those predicted by
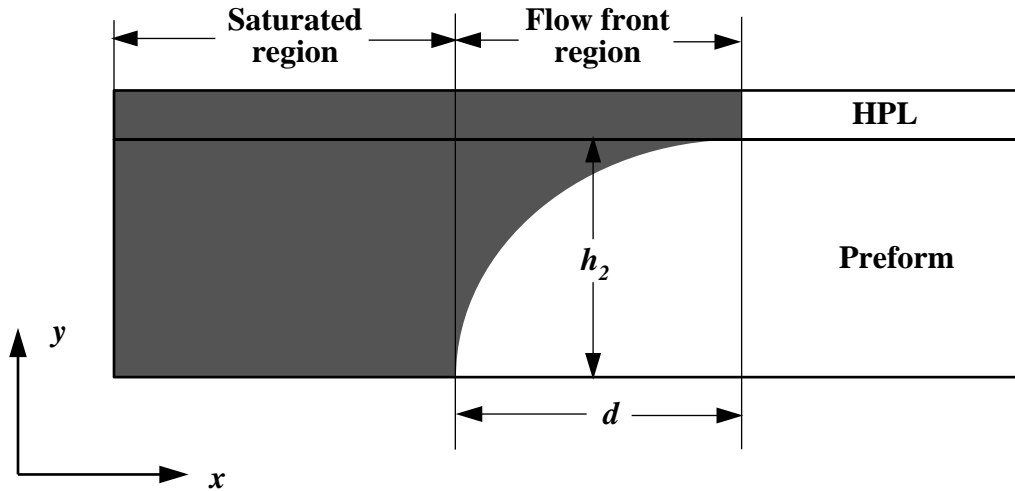
Figure 2.1: Schematic diagram of flow front associated with using a HPL

the theory and simulation. The simulation results were within 13 percent of the measured values. The model overpredicted the length of the lag because the theory did not consider the contribution to the fiber saturation from in-plane flow. This study showed that the use of HPL created a transverse flow in the fiber mat, and thus greatly reduced mold filling time.

Hsiao et al. [27] proposed a more accurate closed form solution for flow in the distribution medium and fiber mat during the VARTM process by taking the in-plane flow in the fiber mat into consideration. The flow was divided into a saturated region with no cross flow and a flow front region where the resin was infiltrating into the preform from the distribution medium. The flow front region moved with a uniform velocity and kept a steady shape. The law of conservation of mass and Darcy's law were applied in each region. It was found that the flow front was parabolic in shape and the length of the saturated region was proportional to the square root of the time elapsed. The results obtained were compared with full-scale 3D numerical simulations and an error analysis carried out. The value of the parameter, $\epsilon = K_{2xx}h_2{}^2/K_{2yy}d^2$, was a measure of the error between the analytical model and the numerical simulations. In the formulation, K_{2xx} and K_{2yy} are the permeabilities of the fiber mat in the direction of flow advancement and thickness direction, respectively. h_2 represents the thickness of the fiber mat and d is the flow front length (Fig. 2.1). The error in the

total infiltration time remains small as ϵ increased. However, the error in the flow front length grows rapidly while ϵ increases. The reason for this is that the theory neglected the transition region between the saturated region and the flow front region. The contribution of this region to the through-thickness flow was effectively lumped into the flow front region, and thus gave rise to the error. As the transition region increases in significance with increasing ϵ, it increasingly affects the flow front region and the error in the flow front length grows rapidly. A parametric study was conducted to investigate the influence of a number of process variables on the fill time and flow front velocity. It was found that the fill time decreases and the velocity increases when the thickness of the distribution medium relative to that of the preform increases. The porosity of the distribution medium was found not to affect the filling time and the flow front velocity significantly. The flow front velocity was found to be much more sensitive to the permeability of the distribution medium than that of the preform.

Sun et al. [28] investigated the flow mechanism in the SCRIMP process based on the distribution medium through flow visualization experiments and numerical simulations. Flow visualization of SCRIMP mold filling was carried out under various molding conditions. It was found that the resin flowed faster in the distribution medium than in the fiber reinforcement, and the flow front lead-lag remained nearly constant during the entire mold filling process. Experiments were conducted to evaluate the importance of the distribution medium in mold filling. Two preforms were injected under similar conditions. The only difference was that the distribution medium was placed on top of the preform in one experiment while no distribution medium was used in the other experiment. The use of distribution medium reduced the filling time by 85 percent. It was very clear that the distribution medium is essential to SCRIMP mold filling. A 3D FE/CV model was employed for the numerical simulation of the mold filling process. The numerical results for the filling time compared well with the experimental measurements. A parametric study was carried out to investigate the influence of the flow properties of the distribution medium and preform on the filling time. The simulation results indicated that the mold filling time was a strong function of

the permeability of the distribution medium, but was not sensitive to that of the preform. Experimental results and the 3D FE/CV simulation demonstrated that the in-plane flow in the preform could be neglected when the permeability of the preform is much less than that of the distribution medium and the length along the flow direction is much larger than the thickness of the composite part. Based on this observation, a leakage flow model was presented to consider the flow as a 2D in-plane flow in the distribution medium with a sink term to account for the resin leakage into the preform. The leakage flow model reduced the computational cost by more than 90 percent and yet provided a reasonable estimation of the mold filling time in SCRIMP based on the distribution medium.

2.2   Compaction of the Preform

Investigation of resin flow in the porous preform in the VARTM process helps industry to ensure that complete impregnation of the preform before resin gellation occurs. Another major concern of the manufacturers is the prediction of the final thickness and thereby, the fiber content of the composite laminate, which is governed by the compaction behavior of the preform. Due to the flexible nature of the vacuum bag, there is no direct control over the thickness or fiber volume fraction of the composite part in the VARTM procedure. The compaction of the reinforcement preform is complex and depends on the compressibility and relaxation of the reinforcement under pressure, and the interaction between the reinforcement and the resin flow. Researchers [29, 30] have conducted experiments to investigate the mechanisms governing compaction of the preform during the VARTM process. The experimental observations are interesting and elaborated in the following paragraphs.

The flexible nature of the vacuum bag, coupled to the varying pressure inside the mold cavity, results in the laminates with a nonuniform final thickness. Rigas et al. [29] investigated variations of the thickness in composite parts manufactured by the VARTM process. A set of experiments were conducted using a 22-ply, S2 glass, plain weave fabric. All of the

preforms were 50.8 cm x 50.8 cm and the distribution media were 45.7 cm x 45.7 cm. The panels were manufactured using a line feed source at one end and a line vacuum source at the other end. Final part thicknesses were measured at different locations after the parts were fully cured. It was found that the final cured thickness of a part changes along the resin progression direction. As the distance from the vacuum source increases, the part thickness increases, and correspondingly, the fiber volume fraction of the laminates decreases. The thickness variation across the panel was close to 6 percent.

Williams et al. [30] conducted a preliminary experimental study of fabric compression during the VARTM process. Nine layers of plain weave E-glass fabric of 660 mm x 360 mm were injected with unsaturated polyester resin. Two LVDTs, LVDT1 and LVDT2, were installed to record the thickness change at the locations of 30 mm and 180 mm away from the resin inlet, respectively. Two pressure transducers were positioned at the same locations. Four traces were obtained from four nominally identical runs. It was observed that the changes in thickness are consistent for the four experiments. Both LVDTs recorded an initial, almost instantaneous compaction of the preform as the vacuum was applied, and the reduction in thickness continued at a slower rate after the initial change. At LVDT1 location, two of the experiments recorded a rapid decrease in thickness at the resin front. This might be explained by the initial lubricating effect of the fluid. However, the lubricating effect was not apparent in the other two experiments. A possible explanation for the absence of the lubrication effect would be that the fabric layers were more closely nested at the beginning of the experiment, thus limiting the ability of the fiber network to rearrange. After the flow front passed, a steady increase in thickness was observed at LVDT1 location. However, when the resin reached LVDT2 location, the decrease in thickness was evident and was maintained as the flow continued until the mold filled. After the mold is filled, the resin inlet was closed while the vacuum was left on. This resulted in a steady decrease in resin pressure, accompanied by a further compaction of the laminate at LVDT1 location, but the thickness did not change at LVDT2 location. The mechanisms governing these experimental observations are the subject of the further investigation.

Detailed knowledge about the response of reinforcing fabrics subjected to compressive forces is very important in the investigation of the compaction behavior of the preform during the VARTM process. Kim et al. [31] presented the results of compression and relaxation tests using different fiber samples, including E-glass, graphite cloth, mat and unidirectional material, and combinations of two different fiber orientations. In the compression test, a normal force up to 8.6 MPa was applied to compress the fiber samples at a cross-head speed of 2 mm/min. The curve of compression force versus sample thickness was measured. Accordingly, the relation between the stress and the fiber volume fraction was determined. For the relaxation test, the machine was stopped after an initial stress was applied to the samples. Stress was then measured as a function of time while sample thickness was held constant. It was concluded that the compressive response of the reinforcing materials strongly depends on the fiber orientation and stacking sequence. When loading and unloading the fiber samples, hysteresis effects were observed. Hysteresis may be due to structure relaxation from fiber rearrangement or to fiber breakage. Repeating compression on the same sample resulted in further compaction of the reinforcement material. It was also shown that the lubricated fiber samples were compacted more than the dry reinforcement under the same compression force. Effect of the fiber orientation on the stress relaxation was studied. Relaxation behavior decreases with fiber alignment. Random mats and 0/90 cloth showed much more relaxation than unidirectional fibers. Data of relaxation was fitted with a Maxwell-Wiecher viscoelastic model.

Robitaille and Gauvin [32] gathered the published experimental data for the compaction and relaxation of random mats and woven fabrics to identify general trends related to the compaction of textile reinforcements used in composite processing. Analytical compaction models in the literature were also reviewed, but no published compaction model can fully describe the observed behavior of the reinforcements due to the complexity of the problem. An alternative to analytical models is to interpolate the experimental data directly. The following two equations were used to fit the experimental results obtained from compaction

and relaxation experiments:

$$V_f = AP^B \tag{2.1}$$

$$\frac{P}{P_0} = 1 - Ct^{(1/D)} \tag{2.2}$$

Fiber volume fraction V_f is a function of the compaction pressure P for compaction curves, and the ratio of the current compaction pressure P to the initial compaction pressure P_0 is a function of the time t for relaxation curves. Eight observed parameters were defined based on curve fitting of the experimental data: the initial fiber volume fraction at which the compaction pressure P begins to rise (A), the stiffening index of the reinforcements (B), the average rigidity of the reinforcements (M), the maximum fiber volume fraction reached during part production (Rv_f), the pressure decay after 1 second (C) and after 300 seconds (P_{300}), and the rate of reduction of the pressure during relaxation (D). Thus, comparisons of the experimental curves were conducted and the effects of various processing parameters were identified. In compaction, as the number of layers rises, the representative rigidity M is increased, the initial fiber volume fraction A is increased, and the stiffening index B is decreased both for random mats and woven rovings. In addition, the representative fiber volume fraction Rv_f decreases with a rise of the number of layers for woven materials. For successively applied compaction cycles, A is increased, B is decreased, and Rv_f is increased for both random mats and woven rovings. The representative rigidity M is also increased for woven rovings. Compaction curves progressively move to higher V_f values. In relaxation, the parameter P_{300} is increased (less relaxation) as the applied pressure rises, is decreased as the compaction speed rises, and is decreased as the number of layers rises for both random mats and woven materials.

Reorganization of the fiber networks was shown to have a major impact on the compaction behavior of textile reinforcements subjected to successive cycles [33]. Robitaille and Gauvin [34] demonstrated the reorganization of the fiber network and the effect of friction. The results of sequences of successive compaction cycles applied to dry textiles and to textiles saturated in distilled H_2O and silicon oil were presented. It was shown that the major

reorganization mechanism during the first compaction cycles was lateral spreading of the rovings. It resulted in a significant rise of maximum fiber volume fraction. The fiber volume fraction continued to rise afterwards, but the compaction behavior became essentially dependent on the frictional characteristics of the fiber contacts. It was concluded that the application of a limited number of compaction cycles prior to the resin injection could be used to reduce the volume of the resin rich areas.

More recently, Chen et al. [35] developed a nonlinear compaction model for fibrous preforms. A key physical constant, preform bulk compressibility (C_b) was defined to establish the constitutive law between the applied pressure and the preform bulk volume:

$$\frac{\Delta V}{V_0} = -C_b \Delta P \tag{2.3}$$

where, V_0 is the initial bulk volume and ΔV the bulk volume change. A typical pressure-thickness curve from the compression test can be divided into three regimes: an initial linear regime, a final linear regime, and a nonlinear regime in between. Regime 1 was initiated when a minimum amount of pressure was applied to slightly compact the woven fabric layers. The fiber cross-sections were brought into closer contact, the bulk deformation of the preform came almost entirely from the compressibility of the interstitial space. In the next stage, Regime 2, the larger voids had been filled, and the deformation was contributed by the compression of both the solid and the deforming voids. It was characterized by the nonlinear stage as observed in the experiments. In Regime 3, the cross-sectional geometry of the preform has achieved a self-similarity such that the porosity approached a constant. A micromechanical conceptual model was proposed to determine the preform bulk compressibility in these three regimes. The bulk compressibility C_b is expressed as a function of porosity and five parameters: the initial fiber volume fraction, the maximum attainable fiber volume fraction, the initial pore volume compressibility, the fiber compressibility, and an experimental index. The model prediction was verified by compaction experiments on plain-woven fabric preforms and unidirectional non-woven materials. Excellent agreement

between the theory and experiments had been obtained.

The research work in reinforcement compaction was mainly carried out for the resin transfer molding (RTM) process where the compaction pressure goes as high as 1 MPa, and higher compaction rates are involved. Only a few investigations [29,36,37] on the compression behavior of fibrous reinforcement during VARTM, i.e., under low compaction pressure (≤ 1 atm) were published.

Hammami and Gebart [36] conducted compaction tests with the maximum compaction pressure not exceeding 1 bar. It was found that for low compaction pressures (≤ 1 bar), the number of layers does not have significant influence on the compaction behavior of the preform. Two stacking sequences, i.e., $[(0^o/90^o)_5]$ and $[(0^o)_5/(90^o)_5]$ were tested to investigate the effect of stacking sequence on the compaction response of the reinforcement. The results were that the stacking sequence did not make significant difference for the compaction of dry reinforcements. However, alternating the reinforcement layers helped achieve a higher fiber volume fraction for the compaction of fiber samples saturated with resin. The compressive response of the preform was modeled by interpolating the experimental data using dual kriging method. A 1-D model was presented to simulate the VARTM process. In this model, Darcy's law and continuity equation were used to model the resin flow, and an equation of transverse equilibrium was introduced to take into account the compaction of the preform under the vacuum force. Compared with the infusion experiments, the model obtained a good estimate of the total filling time for VARTM procedure, but the authors did not present any results about the thickness change of the preform.

Rigas et al. [29] performed several experiments on the compressibility of fiberglass preforms under low compaction pressures. It was found that by mechanically loading and unloading the preform, a maximum fiber volume fraction may be attained prior to applying vacuum for resin infusion. The lubrication effect of the resin was also illustrated. In the experiment, a 16% increase in the fiber volume fraction was observed for the preform saturated with resin, compared to the dry fabric under the same load.

2.3   Summary

In our research group, a three-dimensional model, 3DINFIL [38, 39] was developed for the simulation of the resin transfer molding (RTM) and resin film infusion (RFI) procedures. The physical processes modeled include the flow of a resin through a three-dimensional anisotropic preform, heat-transfer in the preform and tooling components, and cure kinetics of the resin. The liquid resin was assumed to be an incompressible, Newtonian fluid. The governing differential equation for the flow model was based on Darcy's law and solved by the Finite Element/Control Volume (FE/CV) technique.

Sayre [40] used the computer model 3DINFIL to simulate the isothermal resin flow in VARTM process. Experiments were conducted to verify the accuracy of the predicted flow front patterns and infiltration times. The flow front patterns were determined to be qualitatively accurate in both the distribution medium and the preform. Simulation results for infiltration times over-predicted the experimental measurement by 8 to 10 %. The difference may be attributed to an inaccurate porosity and permeability model of the preform used in the simulation. In 3DINFIL, the flow model was developed for RTM/RFI process and the porosity and permeability were assumed to be constant during the injection procedure. However, in VARTM process, the flexible nature of the vacuum bag coupled with the varying pressure inside the mold cavity results in a variation of the preform thickness during the impregnation. This complex compaction behavior of the preform leads to the variation of the porosity and permeability of the preform during infusion process.

Therefore, the objective of this research was to modify the existing RTM/RFI model to include VARTM simulation capabilities and to verify this model with VARTM experiments. The new model, 3DINFIL 5.0, features a numerical compaction model incorporated with the resin flow model to predict the final thickness and fiber volume fraction of the composite part, details of resin flow in the porous preform, and the total infiltration time. A variety of element types, including 1D rod element, 2D triangle element, 2D quadrilateral element, 3D tetrahedral element, 3D pentahedral element, and 3D hexahedral element, have been

incorporated into the computer code, enabling efficient modeling of the VARTM process in a variety of conditions, such as shell geometries, parts with inserts, panels of complex shapes, and sandwich structures.

Chapter 3

Model Development

The VARTM process consists of two important mechanisms: flow of the resin through the preform, and compaction and relaxation of the preform under the vacuum force. In addition, the resin viscosity and cure kinetics are important for the accurate simulation of the infusion process and to determine whether the mold can be filled before the resin gellation. Correspondingly, flow model, compaction model, and resin model are developed in this chapter to simulate the VARTM fabrication procedure of the composites.

3.1 Flow Model

The flow model is developed to track the flow of the resin through the distribution medium and the preform. Both the high-permeable distribution medium and the preform can be modeled as heterogeneous and anisotropic porous media. The resin fluid is assumed to be Newtonian (its viscosity is independent of shear rate), and incompressible. Assuming that the flow is quasi-steady state, the governing equations for the flow problem are the continuity equation for an incompressible fluid, and Darcy's law of flow through a porous

medium [26–29]:

$$\nabla \cdot \vec{v} = 0 \tag{3.1}$$

$$\vec{v} = \frac{\vec{q}}{\phi} = -\frac{\mathbf{S}}{\phi\mu}\nabla P_r \tag{3.2}$$

where $\vec{v}$ is the interstitial velocity vector of the resin, $\vec{q}$ the superficial velocity vector, ϕ the porosity of the porous preform, μ the viscosity of the fluid, $\mathbf{S}$ the permeability tensor of the preform, and P_r is the resin pressure. Substituting eqn. (3.2) into (3.1) gives the governing differential equation of the flow:

$$\nabla \cdot \left(\frac{\mathbf{S}}{\phi\mu}\nabla P_r\right) = 0 \tag{3.3}$$

The boundary conditions necessary to solve eqn. (3.3) are:

- A flow front pressure condition: $P_{r_{flowfront}} = 0$

- A constant pressure condition at the inlet: $P_{r_{inlet}} = 1\,atm$

- The velocity normal to the mold wall is zero: $\vec{v} \cdot \vec{n} = 0$, where $\vec{n}$ is the vector normal to the boundary wall

Note that this is a moving boundary problem. The finite element/control volume (FE/CV) method is utilized to track the progression of the flow front. At each time step, the Galerkin finite element method is used to solve for the pressure distribution in the fluid. The resin velocities are then calculated using eqn. (3.2). With resin velocities obtained, the flow front location at that time is determined by means of the control volume technique. The details of the FE/CV technique will be addressed in Chapter 4.

3.2   Compaction Model

3.2.1   Compaction Model Formulation

In addition to the governing equations deriving the flow model, i.e., Darcy's law and the continuity equation, a new equation is introduced to account for the transverse equilibrium inside the mold cavity during impregnation [36]:

$$P_c = P_r + P_n \tag{3.4}$$

where P_c is the total compaction pressure, P_r is the resin pressure, and P_n is the net pressure applied to the preform. For the VARTM process, the external pressure applied is the atmospheric pressure. It is well accepted that during the flow of the resin in the fiber preforms, the total vacuum pressure is shared by the resin pressure and the pressure supported by the fiber network [41, 42].

At each time step, once the resin pressure distribution is obtained from the resin flow model, the pressure supported by the preform is computed using eqn. 3.4. The normal strain in the preform along the transverse direction (ε) is a function of the net pressure applied to the preform. There is no general constitutive model which can fully describe the response of the reinforcement under the compression force. Compaction tests are often conducted to determine curves of compressive strain versus compression pressure. With the initial fiber volume fraction of the preform (V_{f_0}) and thickness of the panel (t_0) given, the fiber volume fraction V_f, displacement w, and thickness t could be found by the following equations:

$$w = \int_{y=0}^{t_0} \varepsilon \, dy \tag{3.5}$$

$$t = \int_{y=0}^{t_0} (1 + \varepsilon) \, dy \tag{3.6}$$

$$V_f = V_{f0} \frac{t_0}{t} \tag{3.7}$$

The flexible nature of the vacuum bag coupled with the varying pressure inside the mold cavity results in the fiber volume fraction and thickness change of the preform during the impregnation process.

3.2.2 Compressibility of the Reinforcement

Since no general constitutive model is available, the relationship between the compressive strain in the preform and the applied pressure is obtained by fitting the compaction test results to an empirical model. Two important phenomena are observed during the compaction experiments. First, because of the resin lubrication effect, the wet fiber sample saturated with resin is compacted more than the dry reinforcement under the same pressure. Second, the compressive response of the preform under the compaction force is not elastic, and the hysteresis occurs during unloading process [29, 43].

During the VARTM infusion process, before the resin front approaches, the dry reinforcement is under vacuum compression. Thus, the compressive strain of the preform can be calculated from the compaction response of the dry preform during the loading process. After the resin passes, the local net pressure applied to the preform decreases as a result of the increasing resin pressure. This is equivalent to an unloading process. Accordingly, the strain in the wet preform is determined by the compaction response of the resin saturated preform during the unloading process. Therefore, the compressive strain varies with the net pressure applied to the preform in the form of eqn. 3.8.

$$\varepsilon = \begin{cases} f_1(P_n) & \textit{dry compaction, loading} \\ f_2(P_n) & \textit{wet compaction, unloading} \end{cases} \tag{3.8}$$

For a standard VARTM process, the resin pressure is maintained at 1 atm in the injection reservoir and 0 atm at the flow front (vacuum side). Fig. 3.1 presents the two different effects

of the flowing resin on the compaction behavior of the preform. In dry condition (3.1a), the preform essentially supports the external pressure, $P_n = P_{atm}$, and a maximum debulking deformation of the dry preform is reached. During infiltration, two deformation mechanisms are present in the wet area of the preform: the wetting compaction (3.1b) and the springback (3.1c). The wetting compaction is caused by a rearrangement of the fiber network, which is created by the lubrication effect of the wetting fluid [30]. Under a given external pressure, the lubrication of the dry preform will cause an increase in the preform compaction (ε) by an additional amount of wetting deformation (ε_w). On the other hand, the presence of the resin leads to an increase of the local resin pressure (P_r). According to eqn. 3.4, the net pressure applied to the preform P_n has to decrease since the total external pressure is constant (P_{atm}). Consequently, the preform compaction (ε) decreases by an amount of springback deformation (ε_s).The two competing mechanisms, wetting compaction and springback, work together to determine the local preform compaction behavior. It is clear that at any time during the infiltration process, the net compaction of the preform will depend on the relative magnitude of the wetting and springback deformation mechanisms.

3.3   Resin Model

The VARTM process uses thermosetting polymeric resins. As the process progresses, the resin begins to cure and change viscosity. The VARTM fabrication method is often used to manufacture large structures that require long processing times, and the completion of the impregnation process before resin gellation becomes a major challenge. Therefore, a model is necessary to predict the cure and viscosity change of the resin.
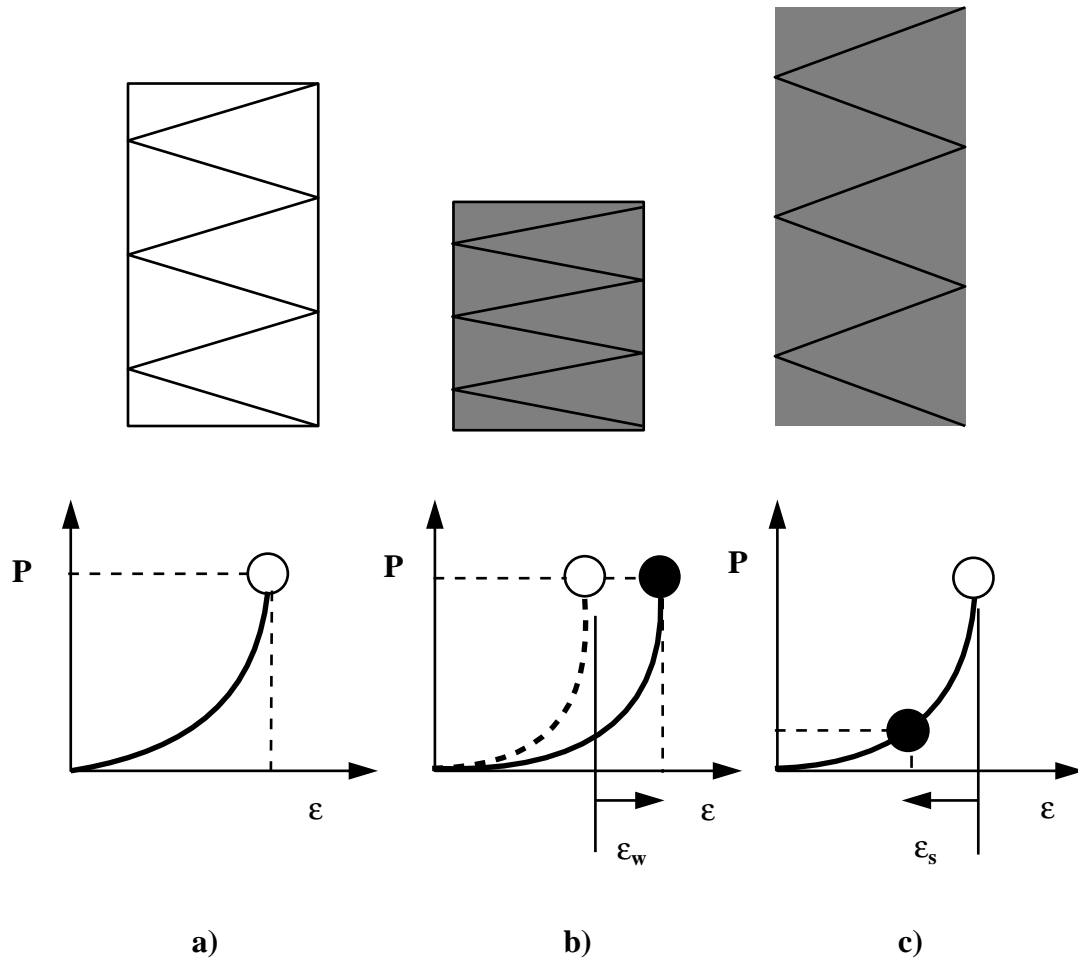
Figure 3.1: Compaction mechanisms during VARTM, a) dry compaction, b) wetting compaction and c) springback

3.3.1 Cure Kinetics Sub-Model

A typical expression for the cure kinetics model is given as follows [44]:

$$\frac{d\alpha}{dt} = f(T, \alpha)(1 - \alpha)^n \tag{3.9}$$

where $d\alpha/dt$ is defined as the reaction or cure rate, α the degree of cure, T the resin temperature, $f(T, \alpha)$ a function that depends on the reaction type, and n is the experimentally determined constant. The cure rate is a function of resin temperature and degree of cure. The VARTM process is often carried out at room temperature. Neglecting the heat liberated from the curing resin, the resin temperature is assumed to be constant and equal to the room temperature. Differential Scanning Calorimetry and Differential Thermal Analyzer are the two common approaches to develop a kinetic model.

If diffusion of chemical species and convection of the fluid is neglected, the degree of cure at each point inside the material can be determined by integrating the expression for the cure rate with respect to time in the following manner:

$$\alpha = \int_0^t (\frac{d\alpha}{dt}) dt \tag{3.10}$$

3.3.2 Viscosity Sub-Model

To accurately predict the resin infiltration process, the viscosity of the resin must be known as a function of both position and time. Resin viscosity is a complex function of shear rate, degree of cure and temperature. There is no existing analytical model which can adequately describe this relation. A reasonable approach is to assume that the resin is a Newtonian fluid and to measure the viscosity at low shear rates. The measured viscosity can then be fit to a mathematical expression relating temperature and time to viscosity. The viscosity

model used in this study was developed by Castro and Macosko [45]:

$$\mu(T, \alpha) = \mu_0(T) \left[\frac{\alpha_g}{\alpha_g - \alpha} \right]^{A(T)+B(T)\alpha} \tag{3.11}$$

where μ is the viscosity, μ_0 the viscosity at zero shear rate, T the temperature, α_g the degree of cure at gel, α the degree of cure, and A and B are parameters which depend on the resin temperature.

3.4   Summary

In this study, a comprehensive model was developed to simulate the VARTM process. The software package, 3DINFIL 5.0, consists of three models: flow model, compaction model, and resin model. Fig. 3.2 illustrates the inputs and outputs for each model, and the interaction between the three models.

At each time step, the resin pressure distribution is computed by the flow model and used as an input to the compaction model. On the other hand, the output of the compaction model, the porosity and permeability of the preform, are updated and influence the resin flow in the preform. The viscosity and degree of cure are also updated in the resin model at each iteration and passed to the flow model. The viscosity is the required input for the resin flow simulation. At each point, the degree of cure (α) is compared with the degree of cure at gel (α_g). Once the resin gels ($\alpha \geq \alpha_g$), the infusion process can not continue any more and the simulation must be stopped. If the resin gels before the mold is filled, the process parameters must be adjusted to ensure the complete filling of the mold. The flow model, compaction model, and resin model are coupled together as a comprehensive VARTM simulation tool to monitor the resin flow pattern in the distribution medium and preform, track the thickness change of the preform, predict the infiltration time and final thickness of the composite part, and determine whether complete filling can be achieved before the resin gels.

INPUT   **MODEL**   **OUTPUT**

Temperature T → | **Resin Model** | → *Viscosity* μ
Degree of cure α

μ , α

Resin viscosity μ
Preform porosity ϕ
Preform permeability S → | **Flow Model** | → *Flow pattern*
Infiltration time
Resin pressure P_r

P_r ϕ , **S**

Resin pressure P_r
Preform compressibility → | **Compaction Model** | → *Preform thickness t*
Preform fiber content V_f
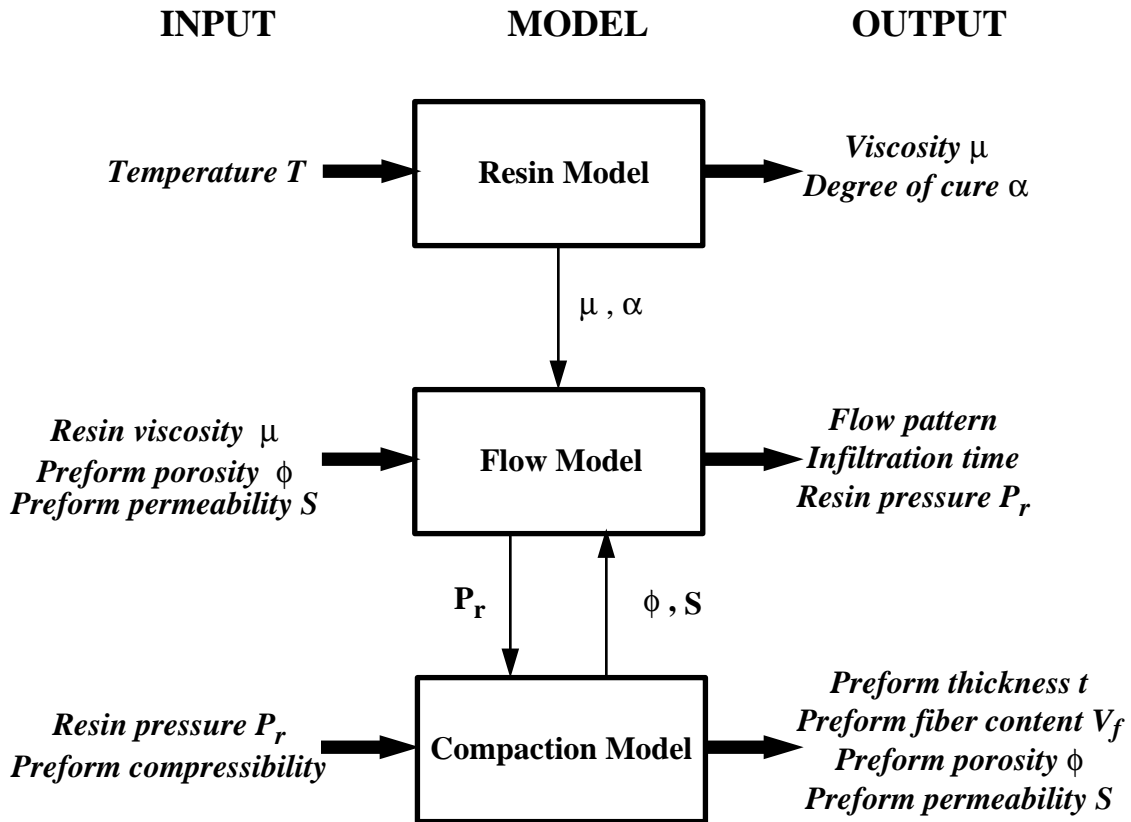*Preform porosity* ϕ
Preform permeability S

Figure 3.2: Inputs and outputs of flow model, compaction model, and resin model

Chapter 4

Finite Element/Control Volume Method

The finite element/control volume (FE/CV) method was selected to solve the resin flow problem because of the advantage that this fixed mesh method eliminates the need for remeshing the resin-filled domain for each time step, thus the flow simulation for a complex geometry can be done rapidly and efficiently.

In the FE/CV approach, the mold is first discretized into finite elements. By subdividing the elements into smaller sub-volumes, a control volume is constructed around each node. The concept of fill factor is introduced to monitor the fluid volume in each control volume. It is defined as a ratio of the volume of the fluid in the control volume to the total volume of the control volume. The fill factor takes on values from 0 to 1, where 0 represents that the control volume is empty and 1 when it is filled. The control volumes can be empty, partially filled, or completely filled. The numerical flow front is constructed of the nodes that have partially filled control volumes. At each time step, fill factors are calculated based on the resin velocity and flow into each nodal control volume. If the resin does not gel, the flow front is thus updated until all the control volumes are full and the infiltration is complete. A flow chart illustrating the numerical procedure is shown in Fig. 4.1.
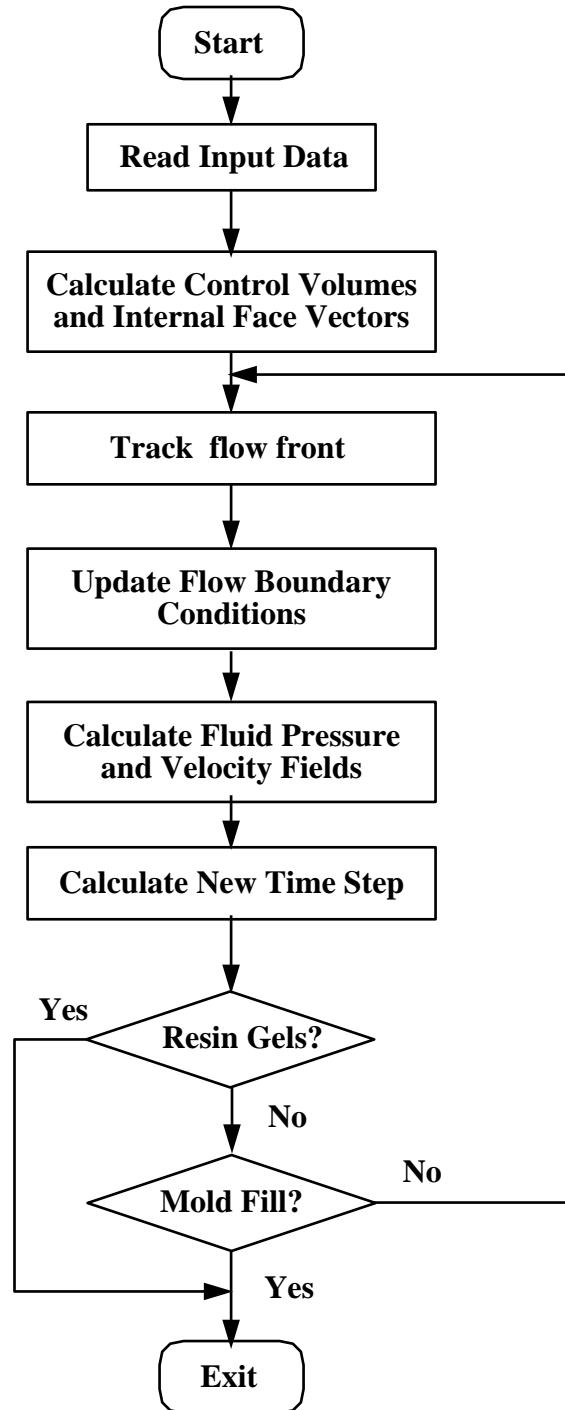
Figure 4.1: Flow chart of the numerical procedure of FE/CV technique

4.1   Galerkin Finite Element Formulation

The governing equation and the boundary conditions for the flow problem are summarized as follows.

$$\nabla \cdot (\frac{\mathbf{S}}{\phi \mu} \nabla P_r) = 0 \quad in \quad \Omega \tag{4.1}$$

$$P_r = \hat{P}_r \quad on \quad \Gamma_1 \tag{4.2}$$

$$\vec{v} \cdot \vec{n} = 0 \quad on \quad \Gamma_2 \tag{4.3}$$

where

$$\Gamma_1 \cup \Gamma_2 = \partial \Omega \quad and \quad \Gamma_1 \cap \Gamma_2 = \Phi \tag{4.4}$$

The boundary of Ω is denoted as $\partial \Omega$, and Γ_1 and Γ_2 are complementary parts of $\partial \Omega$.

Following the standard procedure of Galerkin's method [46], the finite element formulation of the flow problem can be obtained:

$$K_{ij} P_j = 0 \tag{4.5}$$

where P_j is the pressure at each node. K_{ij} is the global resin flow matrix and it can be assembled from the element resin flow matrices:

$$[K_{ij}] = \sum [K_{mn}]^e \tag{4.6}$$

where

$$K_{mn}^e = \int_{\Omega_e} \frac{S_{\alpha\beta}}{\mu\phi} N_{m,\alpha} N_{n,\beta} d\Omega_e \tag{4.7}$$

Here, N_m and N_n are shape functions defined over the element domain Ω_e.

The variation of pressure in a finite element is assumed as

$$P(x_\alpha) = N_m(x_\alpha)P_m \tag{4.8}$$

where, N_m is the shape function, and P_m is the nodal pressure. After the pressures at all the nodes have been solved, the velocities at the centroid of each element is calculated using Darcy's law:

$$v_\alpha = -\frac{S_{\alpha\beta}}{\phi\mu}N_{m,\beta}P_m \tag{4.9}$$

After the velocity of the resin is obtained, the control volume technique is used to track the flow front position.

4.2   Control Volume Technique

The control volume technique is a numerical approach for tracking flow font location in fluid dynamics problems involving flow with a free-surface [4]. Compared to the moving mesh methods that track the flow using remeshing schemes, the control volume technique allows for approximate tracking of the flow front using a fixed mesh. The first step to implement the control volume technique is to form a network of the control volumes, which are formed from the finite element mesh. Collectively, the control volumes have the properties of not overlapping, and completely filling the mold cavity. The flow front is advanced in this technique by calculating the macroscopic fluxes passing from full to empty control volumes. The principal advantages of this approach are computational efficiency and stability.

There are three basic components to the control volume technique: (1) control volume formation, (2) flux calculation, and (3) flow front advancement. These are discussed in detail below.
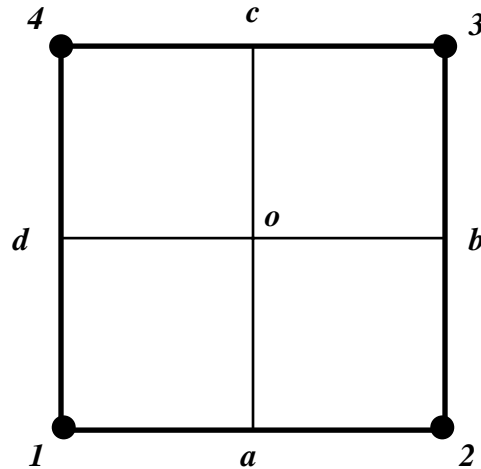
Figure 4.2: Intra-element notation used in the CV technique for linear quadrilateral elements

4.2.1   Control Volume Formation

Each node in the finite element mesh is surrounded by a 'control volume' that is composed of a collection of sub-volumes from surrounding elements. The size and shape of each control volume are determined by the structure of the mesh.

The mold cavity is first discretized using finite elements, and then each individual element is further divided into sub-volumes. Each sub-volume is associated with one of the nodes on the element. The number of sub-volumes is equal to the number of nodes in the element. The control volume for a particular node is composed of all of the sub-volumes associated with that node. An example of the control volume formation in case of quadrilateral elements is illustrated in Fig. 4.2 and 4.3. In Fig. 4.2, a 4-noded quadrilateral element is divided into four sub-volumes. Points 1, 2, 3 and 4 are the nodes of the element. Point o is the element centroid and the midpoints of the four sides of the quadrilateral element are denoted as point a, b, c, and d, respectively. The element is divided into four sub-volumes defined respectively by the regions, *1aod*, *2boa*, *3cob* and *4doc*. Fig. 4.3 illustrates the formation of the control volume for node i by assembling all the sub-volumes associated with the node.
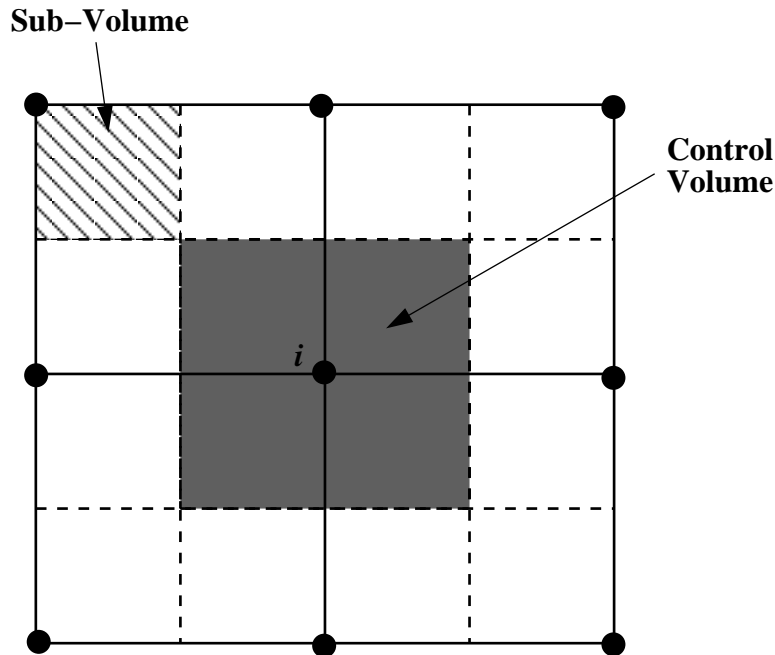
Figure 4.3: Assemblage of a control volume for node i from the sub-volumes

4.2.2   Flux Calculation

In a manner analogous to the control volume formation, there are two parts to the flux calculation. First, the local fluxes into each of the sub-volumes are calculated, then the total fluxes into each control volume are calculated by assembling the individual local flux contributions.

At each time step, the finite element method is first utilized to calculate the resin pressure and velocity as described in Section 4.1. It is assumed that the velocity of the resin is constant throughout each linear element and can be used to compute the local fluxes into each sub-volume. Fig. 4.4 illustrates the calculation of the resin flow into a sub-volume for a quadrilateral element. Points 1, 2, 3 and 4 are the nodes of the quadrilateral element denoted as element 'e'. The sub-volume associated with node 2 is defined by the region *a2bo* (shaded area). The resin flows into sub-volume *a2bo* through the internal boundaries *oa* and *ob*. With the resin velocity $\vec{v}_e$ given, the local flux into the sub-volume, Q_{e2}, can be
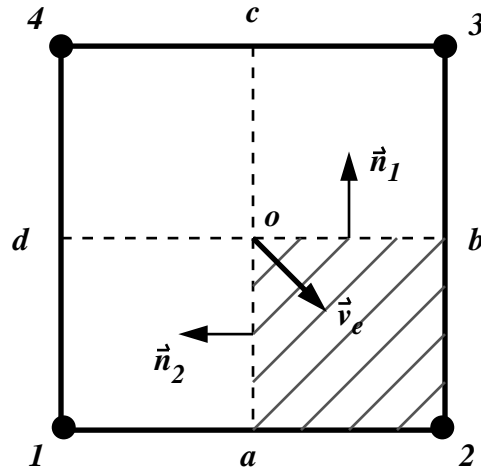
Figure 4.4: Calculation of the local flux into the sub-volume

calculated as

$$Q_{e2} = (-\vec{v}_e \cdot \vec{n}_1 |ob|t) + (-\vec{v}_e \cdot \vec{n}_2 |oa|t) \tag{4.10}$$

where $\vec{n}_1$ and $\vec{n}_2$ are the unit outer normal vectors of the surface ob and oa, respectively, and t is the thickness of the element.

In eqn. 4.10, the first term on the right hand side is the volumetric flow rate across surface ob, and the second term is the volumetric flow rate across surface oa. Eqn. 4.10 can be also written as

$$Q_{e2} = -\vec{v}_e \cdot (\vec{n}_1 |ob| + \vec{n}_2 |oa|)t \tag{4.11}$$

With a new concept of internal face area vector defined as [11]

$$\vec{a}_{e2} = (\vec{n}_1 |ob| + \vec{n}_2 |oa|)t \tag{4.12}$$

eqn. 4.11 can be further simplified as

$$Q_{e2} = -\vec{v}_e \cdot \vec{a}_{e2} \tag{4.13}$$

Generally, the local flux into each sub-volume associated with node 'n' in element 'e' can

be calculated by

$$Q_{en} = -\vec{v}_e \cdot \vec{a}_{en} \tag{4.14}$$

Once the local flux into sub-volumes are calculated, the fluxes into each control volume can be computed by assembling the individual element contributions:

$$Q_n = \sum_{e=1}^{m} Q_{en} \tag{4.15}$$

where Q_n is the total flux into the control volume associated with node 'n', and m is the total number of sub-volumes associated with the node.

4.2.3   Flow Front Advancement

A concept of fill factor is introduced to monitor the progression of the flow front [4]. The fill factor is defined as a ratio of the fluid volume in the control volume to the total volume of the control volume. After the flow rates into each control volume have been calculated, the fill factors can be updated. Given the current time step (Δt), the fill factors from the previous step (f_n^i), the calculated flow rate (Q_n), and the volume of each control volume (V_n), the new fill factors can be calculated with

$$f_n^{(}i+1) = f_n^i + \frac{\Delta t Q_n}{V_n} \tag{4.16}$$

The fill factor takes on values from 0 to 1, where 0 represents totally empty and 1 totally full. When the control volume is partially full, the fill factor is between 0 and 1. The numerical flow front is constructed of the nodes that have partially full control volumes as shown in Fig. 4.5. The accurate location of the fluid in the control volume is not known, so the exact shape of the flow front can not be obtained. The resolution of the flow front is determined by the mesh density.
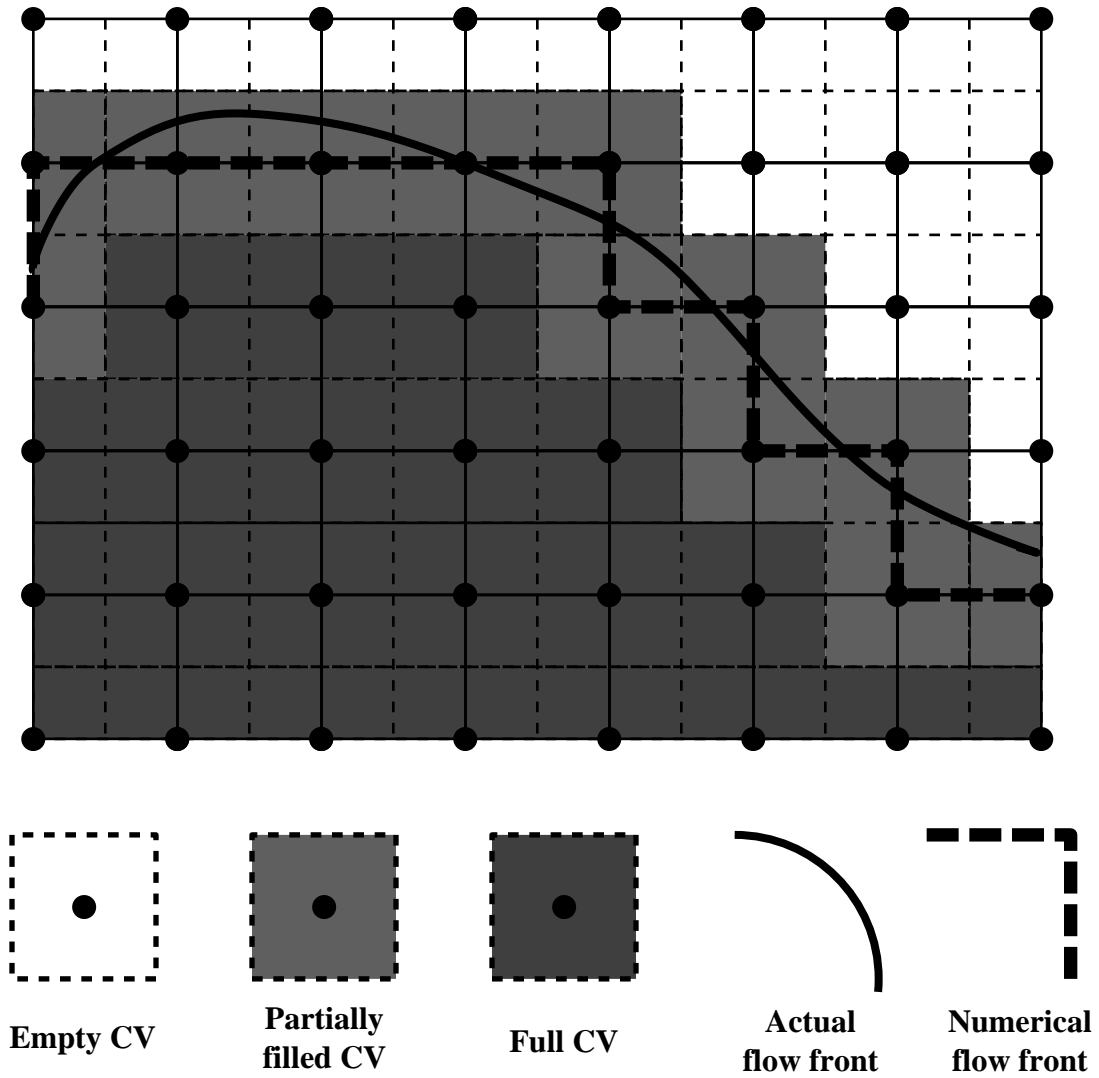
Figure 4.5: Actual and numerical flow front

The time step for the next iteration must be calculated before the solution can proceed. The optimal time step would be where the fluid just fills one control volume. If a larger step were chosen, the flow front would over-run the control volume and result in a loss of mass from the system. The time to fill the partially full control volume 'n' is calculated with the following relation:

$$\Delta t_n = \frac{(1 - f_n)V_n}{Q_n} \tag{4.17}$$

Once Δt_n has been calculated for all the partially filled control volumes, the smallest Δt_n is chosen as the time step for the next iteration.

4.3   Implementation of the Control Volume Technique

The most important parts to the implementation of the control volume method is to divide each individual element into sub-volumes, calculate the volume of each sub-volume, and calculate the internal face area vector for each sub-volume. In this section, the details of these techniques for the various element types are discussed.

4.3.1   One-Dimensional Rod Elements

The notation for rod elements is shown in Fig. 4.6. Points 1 and 2 are the nodes of the rod element and o is the element centroid. The two sub-volumes associated with node 1 and 2 are defined by the line segments *1o* and *2o*. The volume of the two sub-volumes can be calculated as

$$
\begin{aligned}
V_{e1} &= |1o|S \tag{4.18} \\
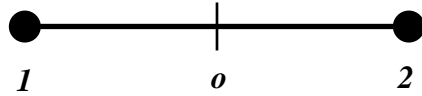V_{e2} &= |2o|S \tag{4.19}
\end{aligned}
$$

Figure 4.6: Intra-element notation used in the CV technique for linear 1D rod elements
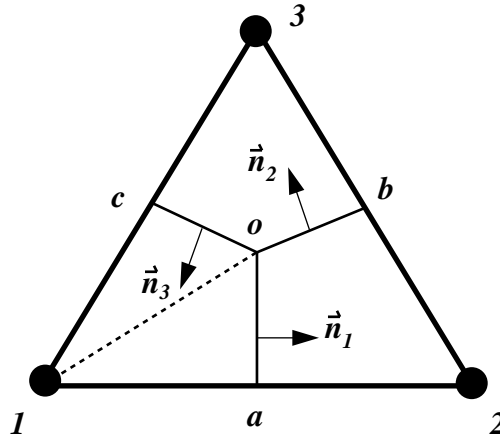

Figure 4.7: Intra-element notation used in the CV technique for linear 2D triangular elements

where, S is the cross-sectional area of the rod. The internal face area vectors of the two sub-volumes are

$$\vec{a}_{e1} = \frac{\vec{1o}}{|1o|}S \tag{4.20}$$

$$\vec{a}_{e2} = \frac{\vec{2o}}{|2o|}S \tag{4.21}$$

4.3.2 Two-Dimensional Triangular Elements

The point definitions for triangles are shown in Fig. 4.7. Points 1, 2, and 3, are the nodes of the triangle element. Points a, b, and c are the midpoints of the sides, and point o is the element centroid. The three sub-volumes associated with node 1, 2, and 3, are defined by the regions, *1aoc*, *2boa*, and *3cob*, respectively.

The region *1aoc* can be divided into two triangles, *1ao* and *1oc* by the segment *o1*. The volume of the region *1aoc* is the sum of the volumes of the two triangle regions:

$$V_{e1} = \frac{1}{2}(|\vec{o1} \times \vec{oa}| + |\vec{o1} \times \vec{oc}|)t \tag{4.22}$$

where, t is the thickness of the element. Similarly, the volumes of the other two sub-volumes can be calculated as:

$$V_{e2} = \frac{1}{2}(|\vec{o2} \times \vec{oa}| + |\vec{o2} \times \vec{ob}|)t \tag{4.23}$$

$$V_{e3} = \frac{1}{2}(|\vec{o3} \times \vec{ob}| + |\vec{o3} \times \vec{oc}|)t \tag{4.24}$$

As shown in Fig. 4.7, $\vec{n}_1$, $\vec{n}_2$, and $\vec{n}_3$ are three vectors perpendicular to $\vec{oa}$, $\vec{ob}$, and $\vec{oc}$, respectively. These vectors have the properties that

$$|\vec{n}_1| = |\vec{oa}| \tag{4.25}$$

$$|\vec{n}_2| = |\vec{ob}| \tag{4.26}$$

$$|\vec{n}_3| = |\vec{oc}| \tag{4.27}$$

Therefore, the internal face area vectors defined for the three sub-volumes are

$$\vec{a}_{e1} = (\vec{n}_1 - \vec{n}_3)t \tag{4.28}$$

$$\vec{a}_{e2} = (\vec{n}_2 - \vec{n}_1)t \tag{4.29}$$

$$\vec{a}_{e3} = (\vec{n}_3 - \vec{n}_2)t \tag{4.30}$$

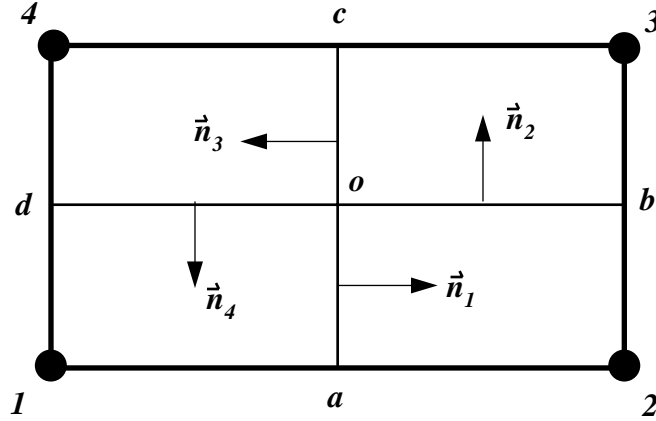where, t is the thickness of the element.

Figure 4.8: Intra-element notation used in the CV technique for linear 2D quadrilateral elements

4.3.3   Two-Dimensional Quadrilateral Elements

The point definitions for quadrilaterals are shown in Fig. 4.8. Points 1 - 4 are the nodes of the quadrilateral element. Points a, b, c and d are the midpoints of the sides, and point o is the element centroid. The four sub-volumes associated with nodes 1, 2, 3, and 4 are defined by the regions: *1aod*, *2boa*, *3cob*, and *4doc*, respectively. The volumes of the four sub-volumes can be calculated as:

$$V_{e1} = \frac{1}{2}(|\vec{o1} \times \vec{oa}| + |\vec{o1} \times \vec{od}|)t \tag{4.31}$$

$$V_{e2} = \frac{1}{2}(|\vec{o2} \times \vec{oa}| + |\vec{o2} \times \vec{ob}|)t \tag{4.32}$$

$$V_{e3} = \frac{1}{2}(|\vec{o3} \times \vec{ob}| + |\vec{o3} \times \vec{oc}|)t \tag{4.33}$$

$$V_{e4} = \frac{1}{2}(|\vec{o4} \times \vec{oc}| + |\vec{o4} \times \vec{od}|)t \tag{4.34}$$

where, t is the thickness of the element.

$\vec{n}_1$, $\vec{n}_2$, $\vec{n}_3$, and $\vec{n}_4$ are vectors perpendicular to $\vec{oa}$, $\vec{ob}$, $\vec{oc}$, and $\vec{od}$, respectively. The

Table 4.1: Definition of sub-volumes for tetrahedral elements

Sub-Volume Number	Sub-Volume Vertices	Internal Surfaces
1	$1ao_1c - do_2oo_3$	1,3,4
2	$2bo_1a - eo_4oo_2$	1,2,5
3	$3co_1b - fo_3oo_4$	2,3,6
4	$4do_3f - eo_4oo_2$	4,5,6

vectors satisfy the following equations:

$$|\vec{n}_1| = |\vec{oa}| \tag{4.35}$$

$$|\vec{n}_2| = |\vec{ob}| \tag{4.36}$$

$$|\vec{n}_3| = |\vec{oc}| \tag{4.37}$$

$$|\vec{n}_4| = |\vec{od}| \tag{4.38}$$

Therefore, the internal face area vectors defined for the four sub-volumes are

$$\vec{a}_{e1} = (\vec{n}_1 - \vec{n}_4)t \tag{4.39}$$

$$\vec{a}_{e2} = (\vec{n}_2 - \vec{n}_1)t \tag{4.40}$$

$$\vec{a}_{e3} = (\vec{n}_3 - \vec{n}_2)t \tag{4.41}$$

$$\vec{a}_{e4} = (\vec{n}_4 - \vec{n}_3)t \tag{4.42}$$

where, t is the thickness of the element.

4.3.4   Three-Dimensional Tetrahedral Elements

The point definitions for tetrahedrons are shown in Fig. 4.9. Points 1 - 4 are the nodes of the element. Points a - f are the mid-points of the line segments connecting the nodes. Points o_{1-4} are the centroids of the sides of the element, and point o is the element centroid. The sub-volumes for the tetrahedron are hexahedrons with vertices defined in Table 4.1.
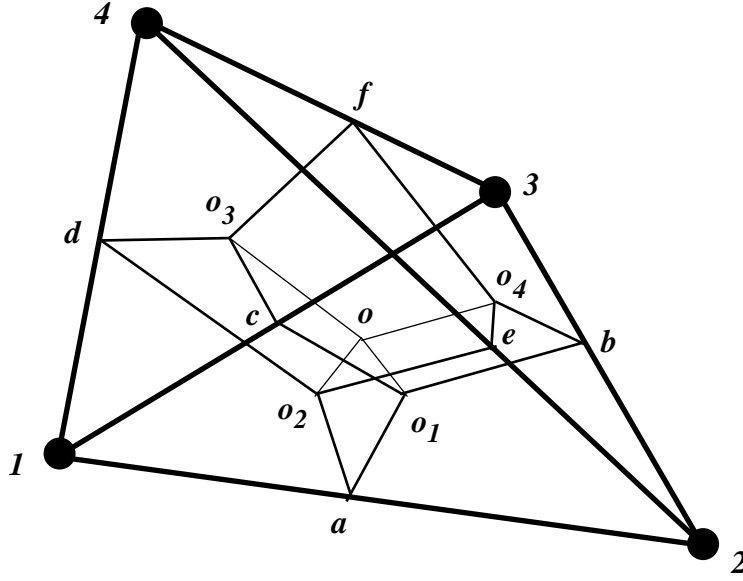
Figure 4.9: Intra-element notation used in the CV technique for linear 3D tetrahedral elements

The six interior integration surfaces s_i for the local flux calculation are defined in Table 4.2. The normal vectors of the six surfaces are defined as $\vec{n}_{1-6}$:

$$\vec{n}_1 = \frac{1}{2}(o\vec{o}_2 \times o\vec{a} + o\vec{a} \times o\vec{o}_1) \tag{4.43}$$

$$\vec{n}_2 = \frac{1}{2}(o\vec{o}_4 \times o\vec{b} + o\vec{b} \times o\vec{o}_1) \tag{4.44}$$

$$\vec{n}_3 = \frac{1}{2}(o\vec{o}_1 \times o\vec{c} + o\vec{c} \times o\vec{o}_3) \tag{4.45}$$

$$\vec{n}_4 = \frac{1}{2}(o\vec{o}_3 \times o\vec{d} + o\vec{d} \times o\vec{o}_2) \tag{4.46}$$

$$\vec{n}_5 = \frac{1}{2}(o\vec{o}_2 \times o\vec{e} + o\vec{e} \times o\vec{o}_4) \tag{4.47}$$

$$\vec{n}_6 = \frac{1}{2}(o\vec{o}_3 \times o\vec{f} + o\vec{f} \times o\vec{o}_4) \tag{4.48}$$

Note that the magnitude of each normal vector is equal to the area of the surface. The internal integral faces associated with each sub-volumes are listed in Table 4.1, and the

Table 4.2: Internal integration surface definitions for tetrahedral elements

Surface Number	Points
1	$oo_2\,ao_1$
2	$oo_4\,bo_1$
3	$oo_3\,co_1$
4	$oo_3\,do_2$
5	$oo_4\,eo_2$
6	$oo_4\,fo_3$

internal face area vectors for these four sub-volumes are calculated as

$$\vec{a}_{e1} = \vec{n}_1 + \vec{n}_3 + \vec{n}_4 \tag{4.49}$$

$$\vec{a}_{e2} = \vec{n}_2 + \vec{n}_5 - \vec{n}_1 \tag{4.50}$$

$$\vec{a}_{e3} = -\vec{n}_2 - \vec{n}_3 - \vec{n}_6 \tag{4.51}$$

$$\vec{a}_{e4} = \vec{n}_6 - \vec{n}_4 - \vec{n}_5 \tag{4.52}$$

Look at the sub-volume associated with node 1, the hexahedron $1ao_1c - do_2oo_3$. This hexahedron can be divided into three polyhedrons $1 - oo_2\,ao_1$, $1 - oo_3\,co_1$, and $1 - oo_3\,do_2$. These three polyhedrons have the same apex, point 1, and their bases are the internal surfaces 1, 3, and 4, respectively. Therefore, the volume of sub-volume related with node 1 is the sum of the volumes of the three polyhedrons:

$$
\begin{aligned}
V_{e1} &= \frac{1}{3}\vec{n}_1 \cdot \vec{1o} + \frac{1}{3}\vec{n}_3 \cdot \vec{1o} + \frac{1}{3}\vec{n}_4 \cdot \vec{1o} \\
&= \frac{1}{3}(\vec{n}_1 + \vec{n}_3 + \vec{n}_4) \cdot \vec{1o} \\
&= \frac{1}{3}\vec{a}_{e1} \cdot \vec{1o}
\end{aligned}
\tag{4.53}
$$

Similarly,

$$V_{e2} = \frac{1}{3}\vec{a}_{e2} \cdot \vec{2o} \tag{4.54}$$

$$V_{e3} = \frac{1}{3}\vec{a}_{e3} \cdot \vec{3o} \tag{4.55}$$

$$V_{e4} = \frac{1}{3}\vec{a}_{e4} \cdot \vec{4o} \tag{4.56}$$

4.3.5   Three-Dimensional Pentahedral Elements

The point definitions for the pentahedral elements are shown in Fig. 4.10. Points 1-6 are the nodes of the pentahedral element. Points a-i, are the mid-points of the line segments connecting the nodes. Points o_{1-5} are the centroids of the sides of the element, and point o is the element centroid. The sub-volumes for the pentahedral element are the hexahedrons with vertices defined in Table 4.3. The nine interior integration surfaces s_i for the local flux calculation are defined in Table 4.4. The normal vectors of the nine surfaces are defined as:

$$\vec{n}_1 = \frac{1}{2}(o\vec{o}_3 \times o\vec{a} + o\vec{a} \times o\vec{o}_1) \tag{4.57}$$

$$\vec{n}_2 = \frac{1}{2}(o\vec{o}_1 \times o\vec{b} + o\vec{b} \times o\vec{o}_4) \tag{4.58}$$

$$\vec{n}_3 = \frac{1}{2}(o\vec{o}_1 \times o\vec{c} + o\vec{c} \times o\vec{o}_5) \tag{4.59}$$

$$\vec{n}_4 = \frac{1}{2}(o\vec{o}_5 \times o\vec{d} + o\vec{d} \times o\vec{o}_3) \tag{4.60}$$

$$\vec{n}_5 = \frac{1}{2}(o\vec{o}_3 \times o\vec{e} + o\vec{e} \times o\vec{o}_4) \tag{4.61}$$

$$\vec{n}_6 = \frac{1}{2}(o\vec{o}_4 \times o\vec{f} + o\vec{f} \times o\vec{o}_5) \tag{4.62}$$

$$\vec{n}_7 = \frac{1}{2}(o\vec{o}_2 \times o\vec{g} + o\vec{g} \times o\vec{o}_3) \tag{4.63}$$

$$\vec{n}_8 = \frac{1}{2}(o\vec{o}_2 \times o\vec{h} + o\vec{h} \times o\vec{o}_4) \tag{4.64}$$

$$\vec{n}_9 = \frac{1}{2}(o\vec{o}_2 \times o\vec{i} + o\vec{i} \times o\vec{o}_5) \tag{4.65}$$

The magnitude of each normal vector is equal to the area of the surface. The internal integral faces associated with each sub-volume are listed in Table 4.3, and the internal face area vectors for the six sub-volumes are calculated as

$$\vec{a}_{e1} = \vec{n}_1 + \vec{n}_3 + \vec{n}_4 \tag{4.66}$$

$$\vec{a}_{e2} = \vec{n}_5 - \vec{n}_1 - \vec{n}_2 \tag{4.67}$$

$$\vec{a}_{e3} = \vec{n}_2 - \vec{n}_3 + \vec{n}_6 \tag{4.68}$$

$$\vec{a}_{e4} = \vec{n}_7 - \vec{n}_4 - \vec{n}_9 \tag{4.69}$$

$$\vec{a}_{e5} = \vec{n}_8 - \vec{n}_5 - \vec{n}_7 \tag{4.70}$$

$$\vec{a}_{e6} = \vec{n}_9 - \vec{n}_6 - \vec{n}_8 \tag{4.71}$$

The volumes of the six sub-volumes are calculated as

$$V_{e1} = \frac{1}{3}\vec{a}_{e1} \cdot \vec{1o} \tag{4.72}$$

$$V_{e2} = \frac{1}{3}\vec{a}_{e2} \cdot \vec{2o} \tag{4.73}$$

$$V_{e3} = \frac{1}{3}\vec{a}_{e3} \cdot \vec{3o} \tag{4.74}$$

$$V_{e4} = \frac{1}{3}\vec{a}_{e4} \cdot \vec{4o} \tag{4.75}$$

$$V_{e5} = \frac{1}{3}\vec{a}_{e5} \cdot \vec{5o} \tag{4.76}$$

$$V_{e6} = \frac{1}{3}\vec{a}_{e6} \cdot \vec{6o} \tag{4.77}$$

4.3.6   Three-Dimensional Hexahedral Elements

The point definitions for hexahedrons are shown in Fig 4.11. Points 1-8 are the nodes of the hexahedral elements, points *a-l*, are the midpoints of the line segments connecting the nodes, points o_{1-6} are the centroids of the sides of the element, and point *o* is the element centroid. The sub-volumes are the hexahedrals with vertices defined in Table 4.5. For hexahedral

Table 4.3: Definition of sub-volumes for pentahedral elements

Sub-Volume Number	Sub-Volume Vertices	Internal Surfaces
1	$1ao_1c - do_3oo_5$	1,3,4
2	$2bo_1a - eo_4oo_3$	1,2,5
3	$3co_1b - fo_5oo_4$	2,3,6
4	$4go_2i - do_3oo_5$	4,7,9
5	$5ho_2g - eo_4oo_3$	5,7,8
6	$6io_2h - fo_5oo_4$	6,8,9

Table 4.4: Internal integration surface definitions for pentahedral elements

Surface Number	Points
1	oo_3ao_1
2	oo_4bo_1
3	oo_5co_1
4	oo_5do_3
5	oo_3eo_4
6	oo_4fo_5
7	oo_2go_3
8	oo_2ho_4
9	oo_2io_5
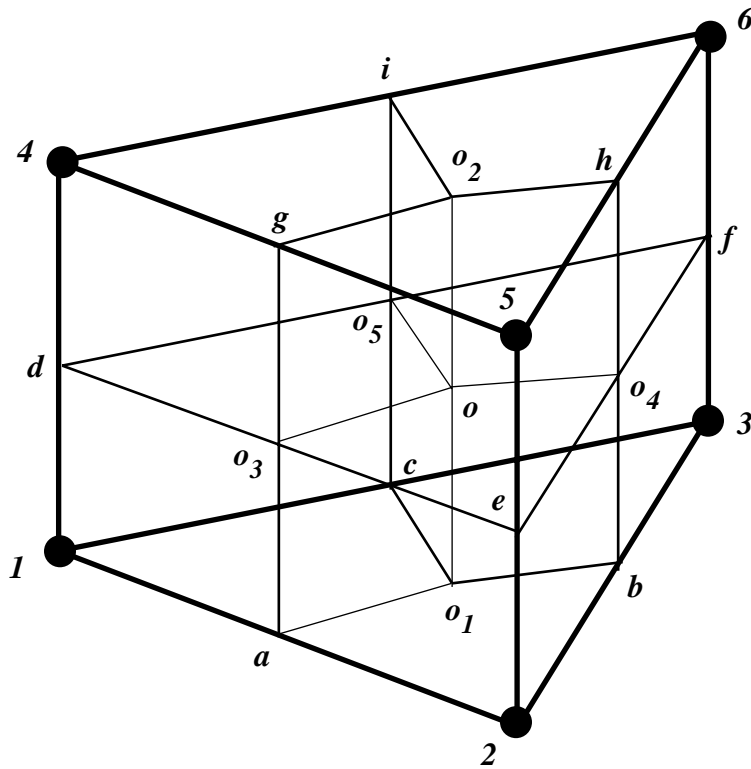
Figure 4.10: Intra-element notation used in the CV technique for linear 3D pentahedral elements

elements, there are 12 internal integration surfaces needed for the local flux calculation. These are defined in Table 4.6. The normal vectors of the 12 surfaces are defined as:

$$\vec{n}_1 = \frac{1}{2}(\vec{oo_3} \times \vec{oa} + \vec{oa} \times \vec{oo_1}) \tag{4.78}$$

$$\vec{n}_2 = \frac{1}{2}(\vec{oo_6} \times \vec{ob} + \vec{ob} \times \vec{oo_1}) \tag{4.79}$$

$$\vec{n}_3 = \frac{1}{2}(\vec{oo_4} \times \vec{oc} + \vec{oc} \times \vec{oo_1}) \tag{4.80}$$

$$\vec{n}_4 = \frac{1}{2}(\vec{oo_5} \times \vec{od} + \vec{od} \times \vec{oo_1}) \tag{4.81}$$

$$\vec{n}_5 = \frac{1}{2}(\vec{oo_5} \times \vec{oe} + \vec{oe} \times \vec{oo_3}) \tag{4.82}$$

$$\vec{n}_6 = \frac{1}{2}(\vec{oo_3} \times \vec{of} + \vec{of} \times \vec{oo_6}) \tag{4.83}$$

$$\vec{n}_7 = \frac{1}{2}(\vec{oo_6} \times \vec{og} + \vec{og} \times \vec{oo_4}) \tag{4.84}$$

$$\vec{n}_8 = \frac{1}{2}(\vec{oo_4} \times \vec{oh} + \vec{oh} \times \vec{oo_5}) \tag{4.85}$$

$$\vec{n}_9 = \frac{1}{2}(\vec{oo_2} \times \vec{oi} + \vec{oi} \times \vec{oo_3}) \tag{4.86}$$

$$\vec{n}_{10} = \frac{1}{2}(\vec{oo_2} \times \vec{oj} + \vec{oj} \times \vec{oo_6}) \tag{4.87}$$

$$\vec{n}_{11} = \frac{1}{2}(\vec{oo_2} \times \vec{ok} + \vec{ok} \times \vec{oo_4}) \tag{4.88}$$

$$\vec{n}_{12} = \frac{1}{2}(\vec{oo_2} \times \vec{ol} + \vec{ol} \times \vec{oo_5}) \tag{4.89}$$

The magnitude of each normal vector is equal to the area of the surface. The internal integral faces associated with each sub-volume are listed in Table 4.5, and the internal face

area vectors for the six sub-volumes are calculated as

$$\vec{a}_{e1} = \vec{n}_1 - \vec{n}_4 + \vec{n}_5 \tag{4.90}$$

$$\vec{a}_{e2} = \vec{n}_2 - \vec{n}_1 + \vec{n}_6 \tag{4.91}$$

$$\vec{a}_{e3} = \vec{n}_3 + \vec{n}_7 - \vec{n}_2 \tag{4.92}$$

$$\vec{a}_{e4} = \vec{n}_4 + \vec{n}_8 - \vec{n}_3 \tag{4.93}$$

$$\vec{a}_{e5} = \vec{n}_9 - \vec{n}_5 - \vec{n}_{12} \tag{4.94}$$

$$\vec{a}_{e6} = \vec{n}_{10} - \vec{n}_6 - \vec{n}_9 \tag{4.95}$$

$$\vec{a}_{e7} = \vec{n}_{11} - \vec{n}_7 - \vec{n}_{10} \tag{4.96}$$

$$\vec{a}_{e8} = \vec{n}_{12} - \vec{n}_8 - \vec{n}_{11} \tag{4.97}$$

The volumes of the eight sub-volumes are calculated as

$$V_{e1} = \frac{1}{3}\vec{a}_{e1} \cdot \vec{1o} \tag{4.98}$$

$$V_{e2} = \frac{1}{3}\vec{a}_{e2} \cdot \vec{2o} \tag{4.99}$$

$$V_{e3} = \frac{1}{3}\vec{a}_{e3} \cdot \vec{3o} \tag{4.100}$$

$$V_{e4} = \frac{1}{3}\vec{a}_{e4} \cdot \vec{4o} \tag{4.101}$$

$$V_{e5} = \frac{1}{3}\vec{a}_{e5} \cdot \vec{5o} \tag{4.102}$$

$$V_{e6} = \frac{1}{3}\vec{a}_{e6} \cdot \vec{6o} \tag{4.103}$$

$$V_{e7} = \frac{1}{3}\vec{a}_{e7} \cdot \vec{7o} \tag{4.104}$$

$$V_{e8} = \frac{1}{3}\vec{a}_{e8} \cdot \vec{8o} \tag{4.105}$$

Table 4.5: Definition of sub-volumes for hexahedral elements

Sub-Volume Number	Sub-Volume Vertices	Internal Surfaces
1	$1ao_1d - eo_3oo_5$	1,4,5
2	$2bo_1a - fo_6oo_3$	1,2,6
3	$3co_1b - go_4oo_6$	2,3,7
4	$4do_1c - ho_5oo_4$	3,4,8
5	$5io_2l - eo_3oo_5$	5,9,12
6	$6jo_2i - fo_6oo_3$	6,9,10
7	$7ko_2j - go_4oo_6$	7,10,11
8	$8lo_2k - ho_5oo_4$	8,11,12

Table 4.6: Internal integration surface definitions for hexahedral elements

Surface Number	Points
1	oo_3ao_1
2	oo_6bo_1
3	oo_4co_1
4	oo_5do_1
5	oo_5eo_3
6	oo_3fo_6
7	oo_6go_4
8	oo_4ho_3
9	oo_2io_3
10	oo_2jo_6
11	oo_2ko_4
12	oo_2lo_5
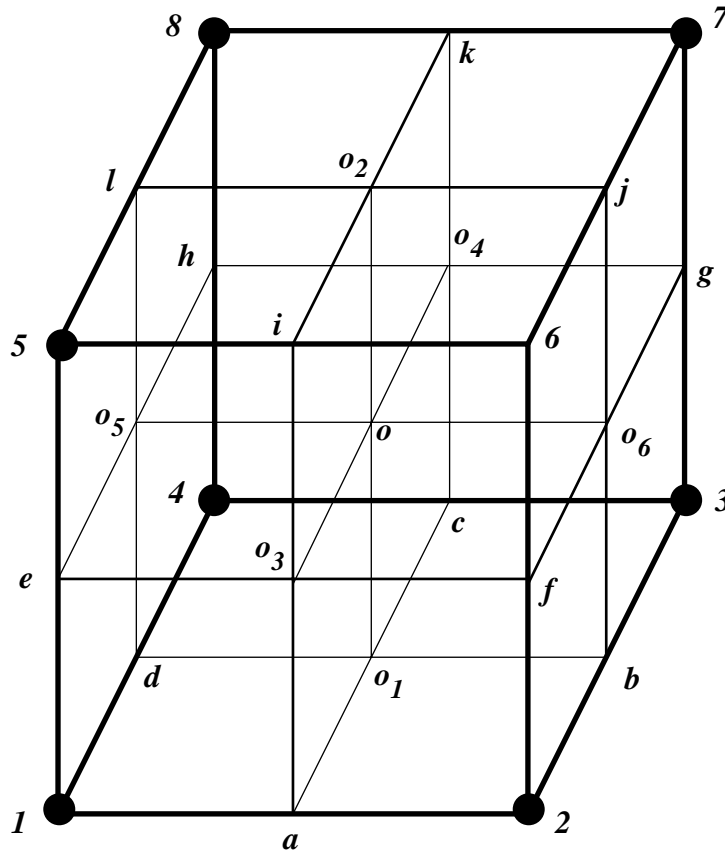
Figure 4.11: Intra-element notation used in the CV technique for linear 3D hexahedral elements

Chapter 5

VARTM of Flat Panels

Two composite panels were fabricated by the VARTM process using SAERTEX multi- axial warp knit carbon fiber fabric and the SI-ZG-5A epoxy resin. Panel 1 contained one stack of the carbon fabric, and panel 2 contained four stacks of the fabric. Each stack of the SAERTEX fabric consists of seven layers of unidirectional carbon fibers, which are laid up in a quasi-isotropic stacking sequence and knitted together [43].

VARTM of the preforms was simulated using the simulation model developed in Chapter 3 (3DINFIL 5.0). To assess the accuracy of the model, the predicted flow patterns and the changes in preform thickness during resin infiltration were compared with the values measured in the experiments.

5.1 Material Characterization

5.1.1 SI-ZG-5A Epoxy Resin

SI-ZG-5A epoxy resin is a commercially available anhydride-cure epoxy blend developed for VARTM process at A.T.A.R.D laboratories. It features low viscosity at room temperature,

which is essential for the VARTM process due to the low injection pressure.

The cure kinetics model for SI-ZG-5A was obtained using isothermal and dynamic differential scanning calorimeter (DSC). Isothermal measurements were made between 60^oC and 140^oC. A modified auto-catalytic equation was chosen to model the curing reaction for the resin [50]:

$$\frac{d\alpha}{dt} = \frac{K\alpha^m(1-\alpha)^n}{1 + e^{C(\alpha-(\alpha_{c0}+\alpha_{cT}T))}} \tag{5.1}$$

where

$$K = Ae^{(-\Delta E/RT)} \tag{5.2}$$

The auto-catalytic equation was modified to account for a shift from kinetics to diffusion control. In the equation, C is the diffusion constant, α_{C0} is the critical degree of cure at $T = 0^oK$, and α_{CT} is the constant to account for the increase in critical resin degree of cure with temperature. The experimentally determined values for all the constants in eqns. 5.1 and 5.2 are listed in Table 5.1.

A Rheometric Ares System-Five Parallel-Plate Rheometer was used to measure the resin viscosity. The resin viscosity was found to fit the following equation:

$$\mu = A_\mu e^{(E_\mu/RT)}\frac{\alpha_g}{\alpha_g - \alpha}^{(A+B\alpha)} \tag{5.3}$$

where α_g is the gel point degree of cure. The constants used in the model are given in Table 5.2.

Combining equations 5.1 and 5.3, the viscosity of the resin can be predicted for given temperatures. Fig. 5.1 shows the viscosity as a function of time at 20^oC, 25^oC, and 30^oC. At room temperature, the viscosity of SI-ZG-5A changes less than 5% after 100 minutes. Because in the present study, the infiltration procedure can be finished less than 5 minutes, the viscosity of the resin is assumed to be constant. The viscosity for SI-ZG-5A was measured as $0.34Pa \cdot s$ before the injection.

Table 5.1: Parameters used in SI-ZG-5A kinetics model

Parameter	Value	Unit
ΔE	61.0	$KJ/mole$
A	4.11×10^5	s^{-1}
m	0.551	
n	1.0	
C	40	
α_{C0}	0.216	
α_{CT}	1.3×10^{-3}	K^{-1}

Table 5.2: Parameters used in SI-ZG-5A viscosity model

Parameter	Value	Unit
E_μ	54.8	$KJ/mole$
A_μ	8.3×10^{-11}	$Pa \cdot s$
A	4	
B	6.25	
α_g	0.60	
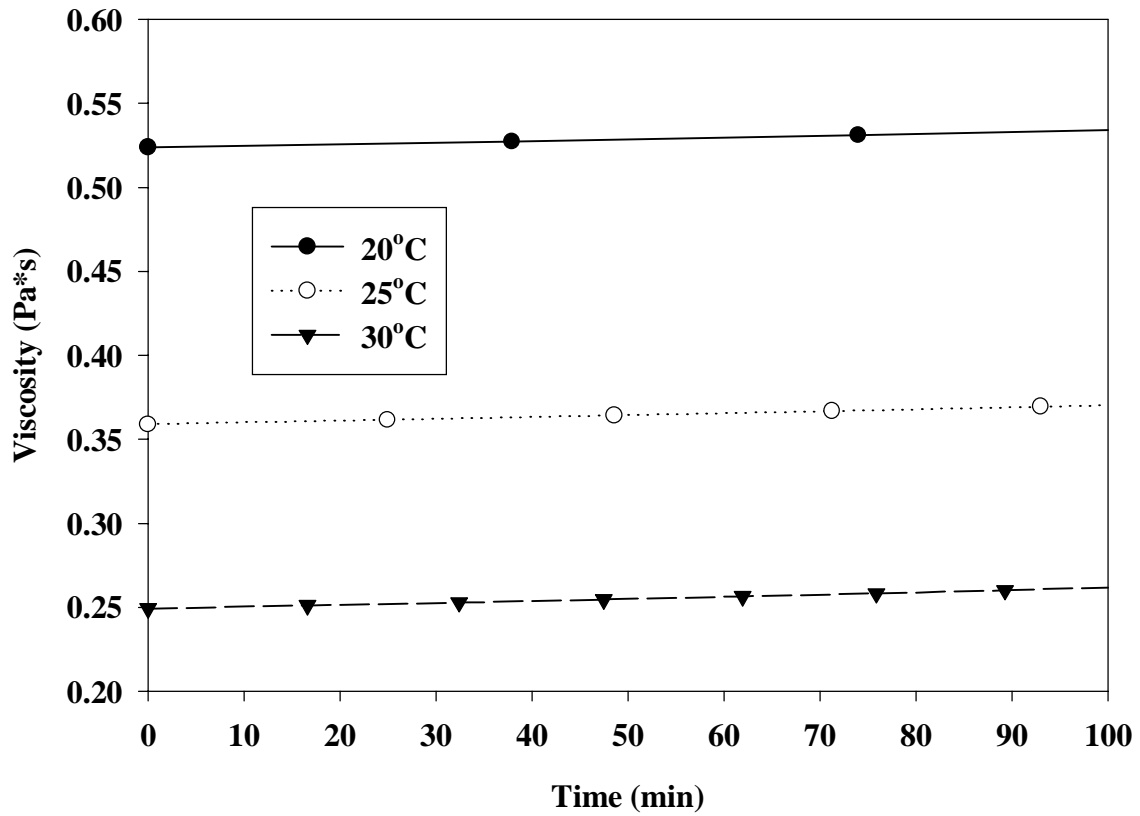
Figure 5.1: Calculated viscosity of the SI-ZG-5A resin

5.1.2   SAERTEX Multi-Axial Warp Knit Carbon Fiber Preform

The permeability of the SAERTEX Multi-Axial Warp Knit (MAWK) carbon preform was measured in the three mutually perpendicular principal material directions. These directions are in-plane along knitting, in-plane normal to knitting, and through the thickness (TTT) direction. The power law equation was chosen to fit the permeability data as a function of the fiber volume fraction:

$$S = a(V_f)^b \tag{5.4}$$

where, S is the permeability in m^2, V_f is the fiber volume fraction, and a and b are fit constants. The fit constants are presented in Table 5.3, and Fig. 5.2 shows the plots of the permeabilities versus fiber volume fraction.

Compaction tests were conducted to develop an understanding of the compressive response of the SAERTEX fabric under the low compaction pressure during VARTM processing. Both dry and wet compaction tests were performed. For the wet preform test, the preform was initially impregnated with SI-ZG-5A resin. The test results of the compaction pressure versus the resulting strain are shown in Figs. 5.3 and 5.4. Note that test data were not recorded during the loading portion of the wet compaction experiment for the 4-stack fabric preform. Because of the resin lubrication effect, the compression response of the wet fibrous preform was found to be quite different from that of the dry fiber mat. The hysteresis phenomenon was observed during the unloading process. During the VARTM infusion process, before the flow front passes by, the dry reinforcement is under vacuum compression and the strain of the preform can be calculated from the compaction response of the dry preform during the loading process. After the resin passes by, the local net pressure applied to the preform decreases as a result of increasing resin pressure. This is equivalent to an unloading process. Therefore, the unloading portion of the wet compaction test essentially simulates the actual VARTM process but in a quasi-static condition. Empirical equations of preform strain as a function of pressure for unstitched MAWK fabric are obtained by fitting the compaction test data to the mathematical expression shown in eqn. 5.5 for 1-stack of

Table 5.3: Fit constants used in unstitched SAERTEX carbon fabric permeability model

	a	**b**
In-plane along knitting	2.0×10^{-13}	-7.62
In-plane normal to knitting	4.0×10^{-13}	-5.36
TTT	6.0×10^{-15}	-7.29

fabric and eqn. 5.6 for 4-stacks of fabric:

$$
\varepsilon = \begin{cases} 0.22(1 - e^{(-0.026P_n)}) & dry\ compaction,\ loading \\[2mm] 0.028 + 0.20\frac{P_n}{1.87+P_n} & wet\ compaction,\ unloading \end{cases}
\tag{5.5}
$$

$$
\varepsilon = \begin{cases} 0.24(1 - e^{(-0.025P_n)}) & dry\ compaction,\ loading \\[2mm] 0.082 + 0.24\frac{P_n}{3.82+P_n} & wet\ compaction,\ unloading \end{cases}
\tag{5.6}
$$

where, ε is the strain of the preform, and P_n is the net pressure applied to the preform.

Fig. 5.5 and Fig. 5.6 show the compaction pressure versus the corresponding fiber volume fraction for the dry and wet preforms. The curves shown correspond to the loading portion of the dry compaction test and unloading portion of the wet compaction test. The maximum achievable fiber volume fraction of the dry preform under full vacuum was 54% and 52% for 1- stack and 4-stack fabric, respectively. However, the wet preforms could be compacted to the fiber volume fraction of 58%. This result illustrates the significant lubrication effect of the wetting fluid on the compaction behavior of the preform as discussed in Chapter 3.

5.1.3   Distribution Medium

The distribution medium used in this study contains three layers of nylon mesh screen. The nylon screen is in-plane isotropic. The in-plane and transverse permeabilities of the distribution medium were measured to be $8.31E - 09\ m^2$ and $5.49E - 10\ m^2$, respectively. The porosity of the distribution medium is 0.75.
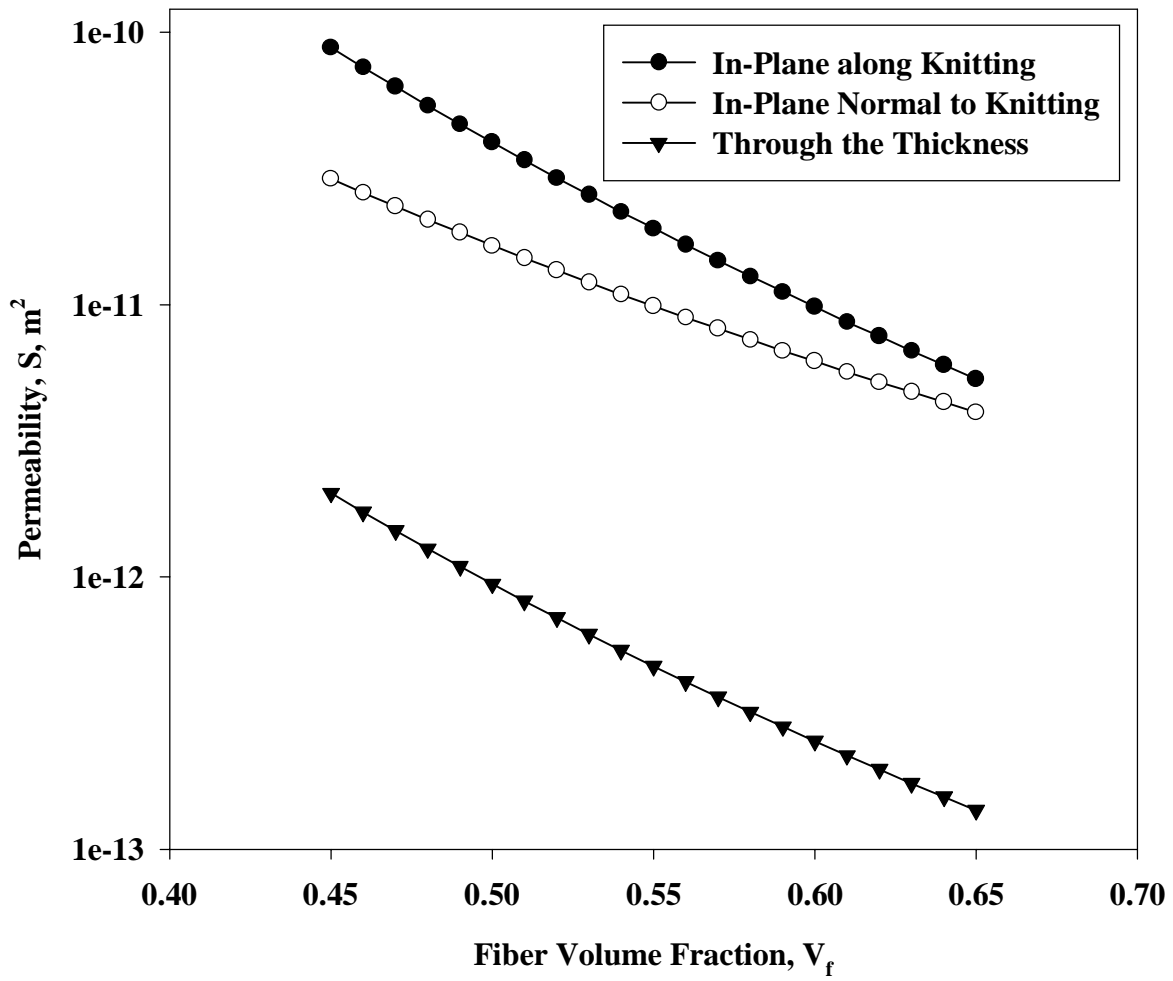
Figure 5.2: Permeability of unstitched SAERTEX carbon fabric
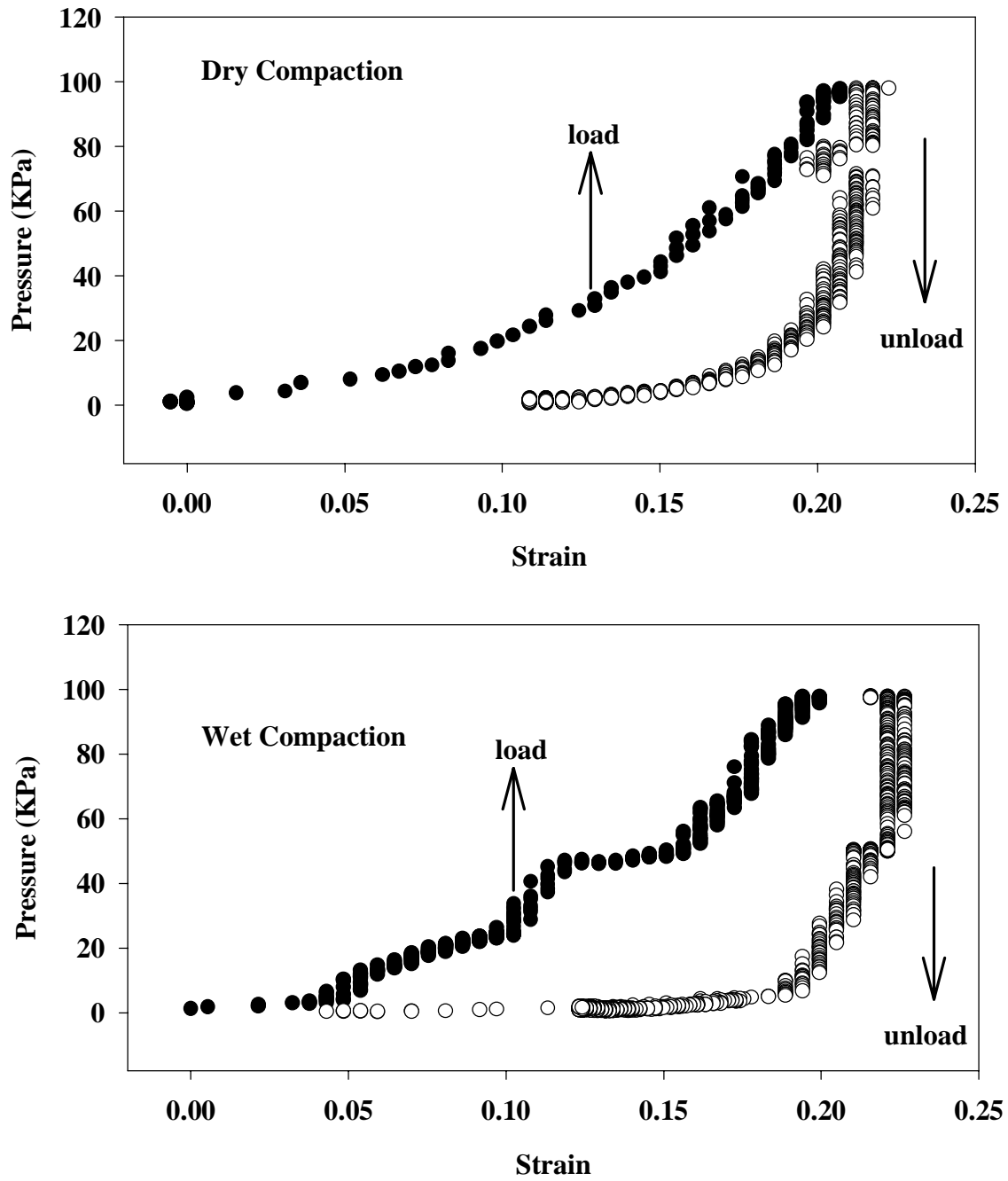
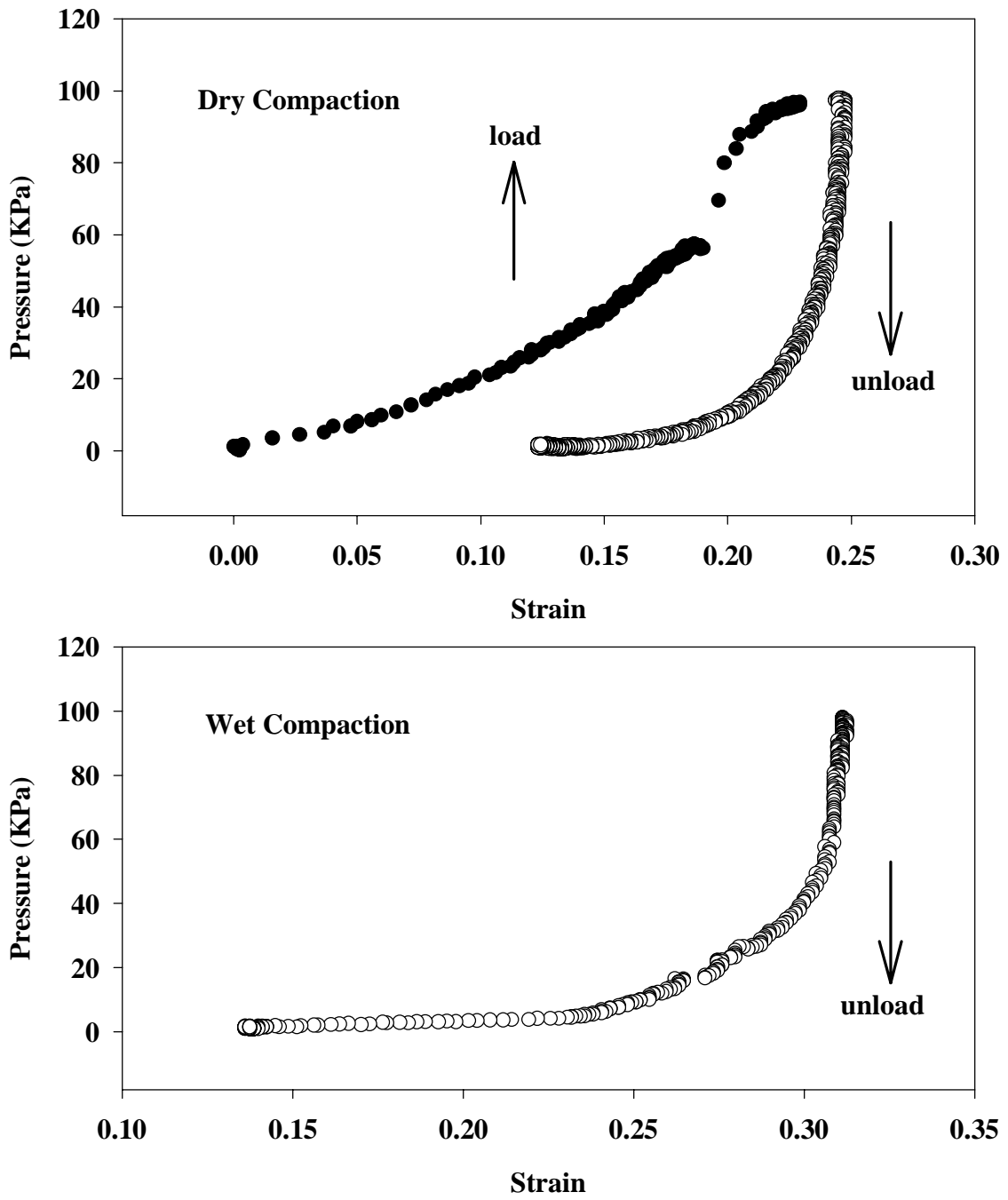Figure 5.3: Compaction test results for 1-stack SAERTEX fabric

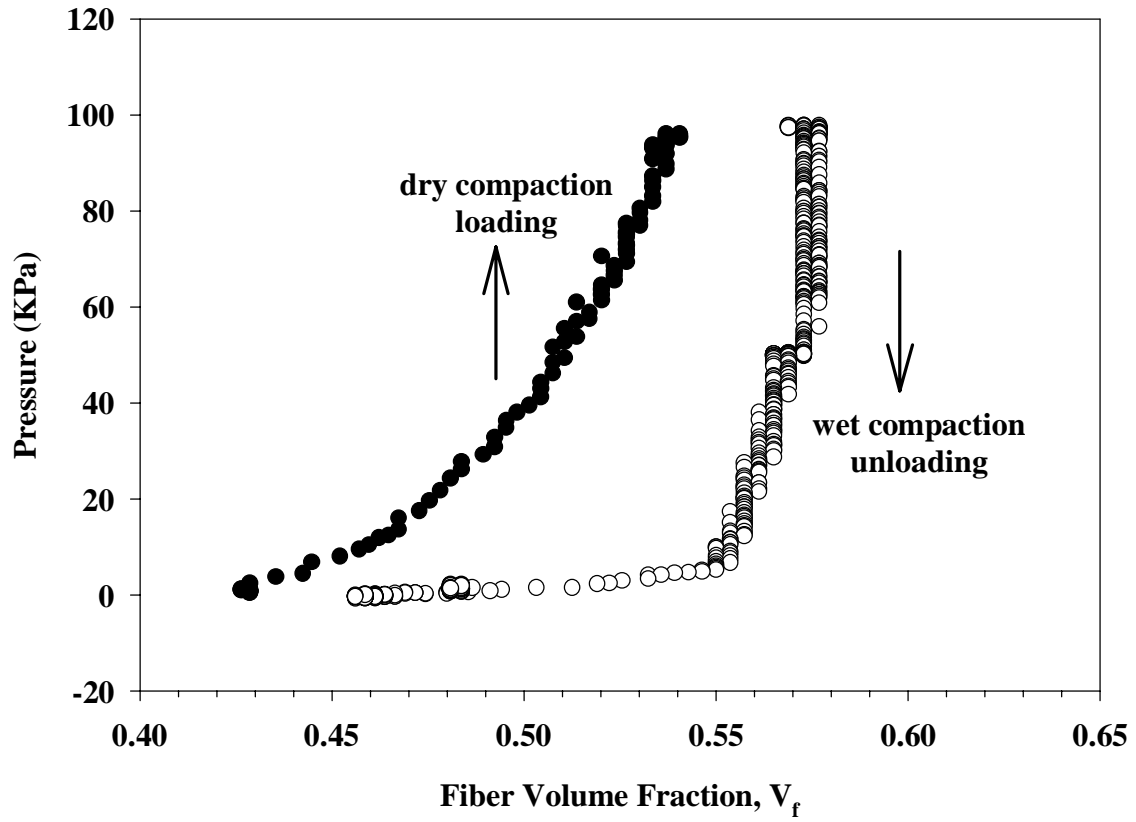Figure 5.4: Compaction test results for 4-stack SAERTEX fabric

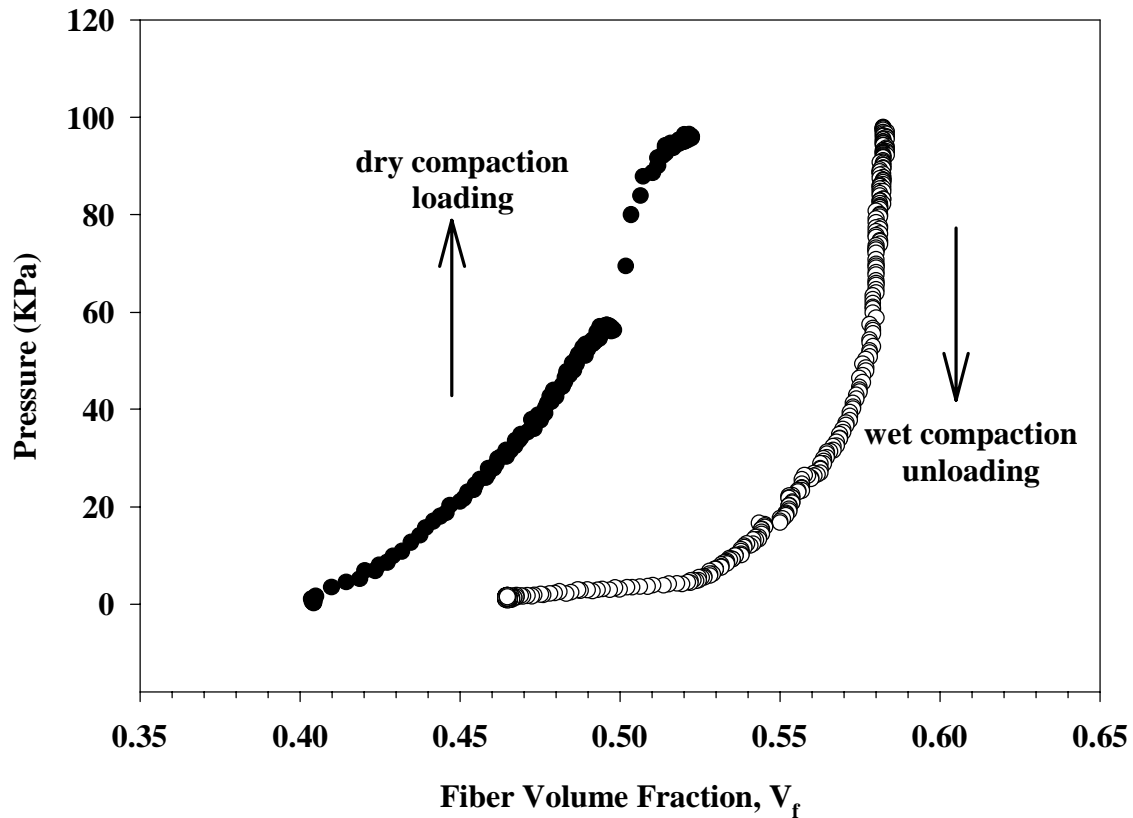Figure 5.5: Fiber volume fraction achieved for 1-stack SAERTEX fabric in the dry and wet compaction tests

Figure 5.6: Fiber volume fraction achieved for 4-stack SAERTEX fabric in the dry and wet compaction tests

5.2 Experiments

Two flat panels (60.96 cm by 30.48 cm) were fabricated by the VARTM process using SAER-TEX multi-axial warp knit carbon fiber fabric and the SI-ZG-5A epoxy resin [43]. Panel 1 contained one stack of the fabric while Panel 2 contained four stacks of the fabric. The initial preform thickness was 0.19 cm for Panel 1 and 0.82 cm for Panel 2.

A 1.27 cm thick aluminum tool was instrumented to allow for measurement of pressure and displacement of the preform during the VARTM infiltration. The pressure sensors and Linear Variable Displacement Transducers (LVDT) were installed to monitor the pressure and thickness change of the panels at different locations (see Fig. 5.7). The pressure sensors,

labeled $P1$ through $P3$ were mounted at the tool surface beneath the fiber preform. $P1$ was 2.5 cm from the preform edge on the resin inlet side, $P2$ was at the center of the preform, and $P3$ was 2.5 cm from the preform edge on the vacuum side. LVDTs, labeled $D1$ through $D3$, were supported above the vacuum bagged preform by a rigid beam. $D1$ was 3.9 cm from the preform edge on the resin inlet side, $D2$ was at the center of the preform, and $D3$ was 3.9 cm from the preform edge on the vacuum side. The preform was cut and placed on the tool. A layer of Armalon fabric was placed above the preform to serve as the release film. The distribution medium was laid on top of the preform and release layer. The medium was cut smaller than the preform allowing a 1.27 cm gap between the edge of the medium and the edge of the preform along the length. The distribution medium ended at a distance of 2.54 cm before the end of the preform. These gaps prevent race-tracking of the resin as it flows through the media and the preform. A 5.08 cm portion of the medium was set off of the panel at the inlet side for inlet tube placement (Fig. 5.7). The outlet tube located on the vacuum side of the part was connected to a resin trap and vacuum pump. The bagging procedure was completed when the preform, medium and tubing were sealed to the aluminum tool using a conformable vacuum bag and sealant tape.

SI-ZG-5A resin was degassed at room temperature under full vacuum for approximately one hour prior to injection. Once the system was equilibrated and all air leaks were eliminated, the resin was allowed to flow into the distribution medium and fiber preform. The flow front at the top surface of the part was recorded using a digital video camcorder. The bottom flow front position was obtained from the tool mounted pressure sensor responses recorded during the test. Typically, the presence of the flow front at the tool surface is indicated by a decrease in the vacuum measured by the sensor. When the preform was fully impregnated, as evidenced through visual inspection, the inlet and then the outlet tube were clamped. The part was then placed in an oven to cure.
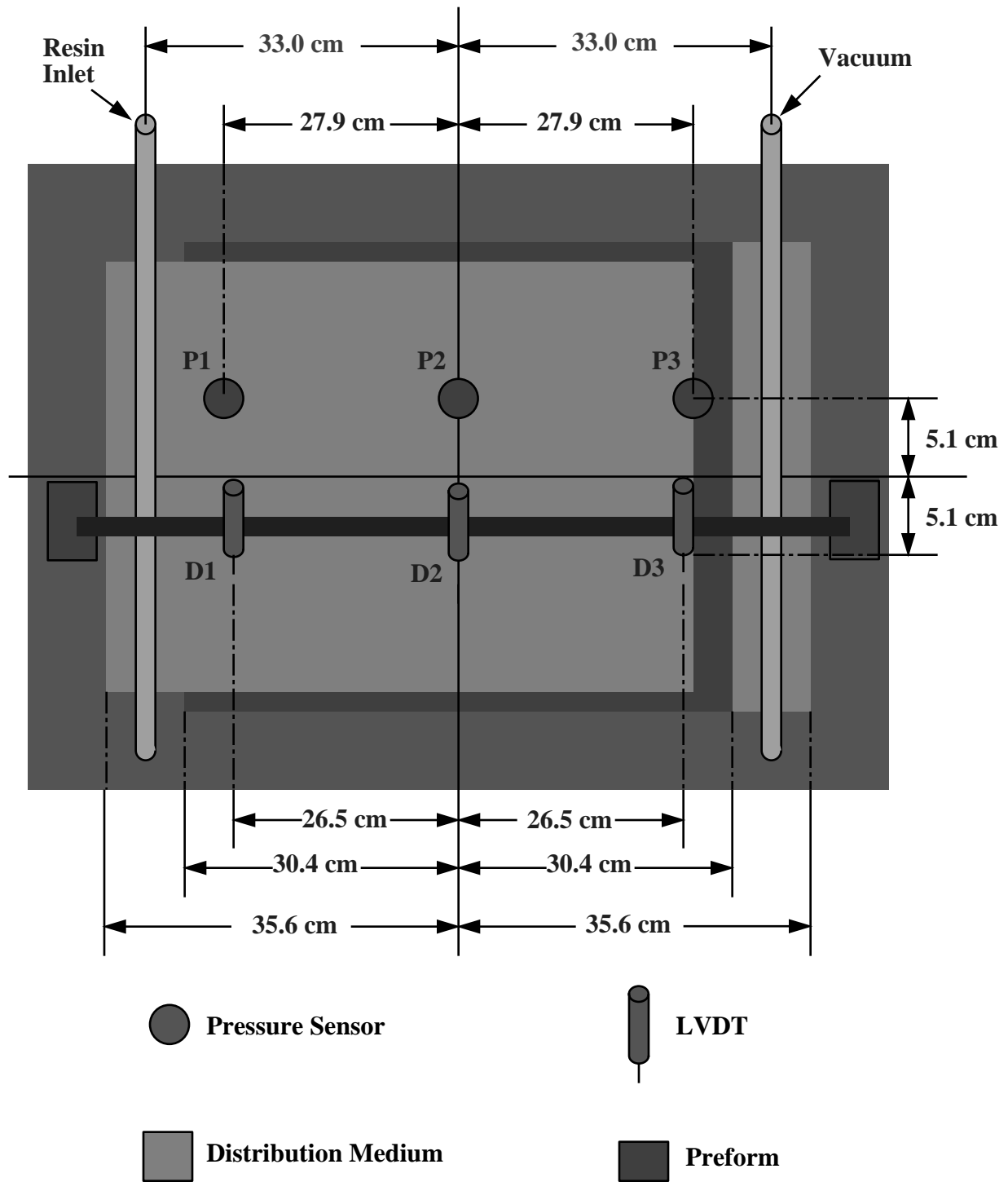
Figure 5.7: The VARTM instrumented system [43]

5.3   Simulation

In this study, except the side edges of the panels where there is no distribution medium, the resin flow condition is uniform across the width of the panels. Therefore, the resin velocity in the width direction is negligible and the resin progression during the VARTM process is reduced to a two-dimensional flow problem.

The design of the infusion scheme in this study is worthy of special attention. As shown in Fig. 5.8 (a), the distribution medium is set off of the panel at the inlet side and wraps around the left edge of the panel. Therefore, the resin can flow into the preform from two directions, from above through the top surface and from the left edge of the preform. However, in the experiment, because no clamping system was used to ensure contact between the medium and preform around the sharp corners of the preform, the distribution medium could be detached from the preform at the left edge as shown in Fig. 5.8 (b). In this study, both cases (Fig. 5.8 (a) and (b)) were considered and two different models were created and named as Model I and Model Ⅱ, correspondingly. Another model as shown in Fig. 5.8 (c) was also created to compare the effect of the different infusion schemes. This model is denoted as Model Ⅲ. In model Ⅲ, no portion of the distribution medium is set off of the panel, and the resin tube is placed above the preform at the left end. Interesting simulation results of the three models will be discussed in this section.
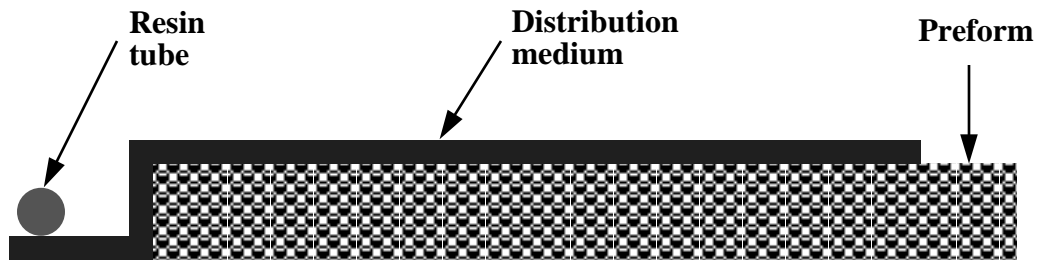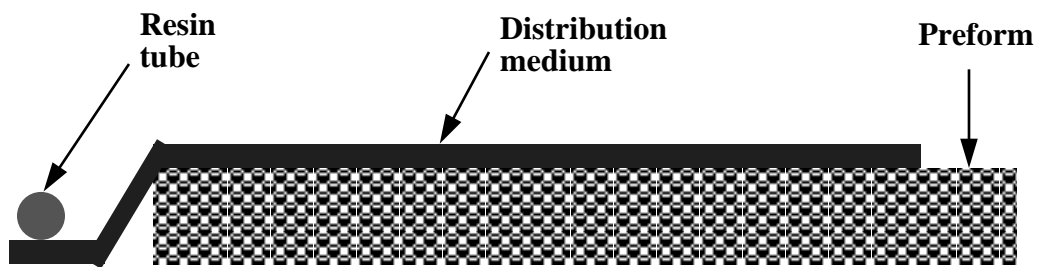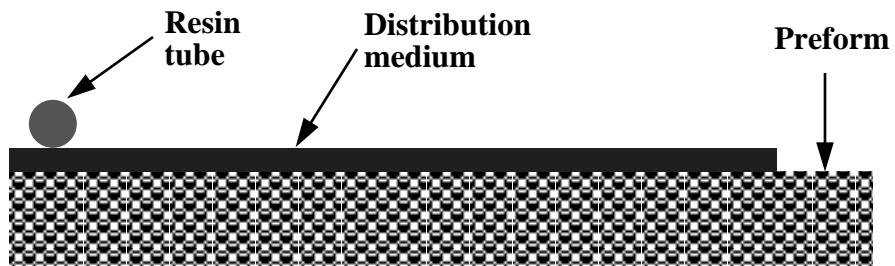
Figure 5.8: Three different VARTM infusion schemes, (a) Model I (b) Model II (c) Model III

5.3.1   Panel 1

Shown in Figures 5.9, 5.10, and 5.11 are comparisons between the calculated and measured infiltration times versus corresponding top and bottom flow front positions for model I, model II, and model III, respectively. The simulation results of model II agree with the experimental data very well while model I overpredicted the infiltration time by approximately 1.7 times. This indicates that in the experiment, the distribution medium did not perfectly conform to the shape of the preform at the left end and model II precisely simulated the actual VARTM lay-up. From Fig. 5.10, the flow front on the top surface leads the resin front on the bottom surface before the end of the distribution medium. However, after the end of the distribution medium, both the top and bottom flow fronts slow significantly, and the bottom flow front catches up with the top resin front. This illustrates the importance of the distribution medium in reducing the infiltration time. Initially one might think that the infusion scheme in model I could shorten the infiltration time because the resin enters the preform through the distribution medium from above and the left end simultaneously. However, this results in the competition for the resin between the flow along the distribution medium (Q_1) and the flow into the preform from the left end (Q_2) as shown in Fig. 5.12. As shown in Fig. 5.9, this competition delays the resin infiltration into the preform by 90 seconds and leads to a significant increase of the total infiltration time compared to the infusion scheme in Model II. The resin infusion scheme in Model III was shown to require least time to fill the panel. The total filling time predicted by model II and model III is 151 and 140 seconds, respectively.

Fig. 5.13 shows the displacements measured by the three LVDTs. Fig. 5.14 presents the displacements at these three locations calculated by model II, which was shown to accurately predict the resin infiltration. The measured and calculated displacements are compared in Figures 5.15–5.17. The calculated thickness change of the preform agrees well with the experimental measurements qualitatively. Before the resin inlet opens, the dry preform is compacted under vacuum and initial displacements are induced. After the infusion process begins, the presence of the resin affects the compaction of the preform by two different
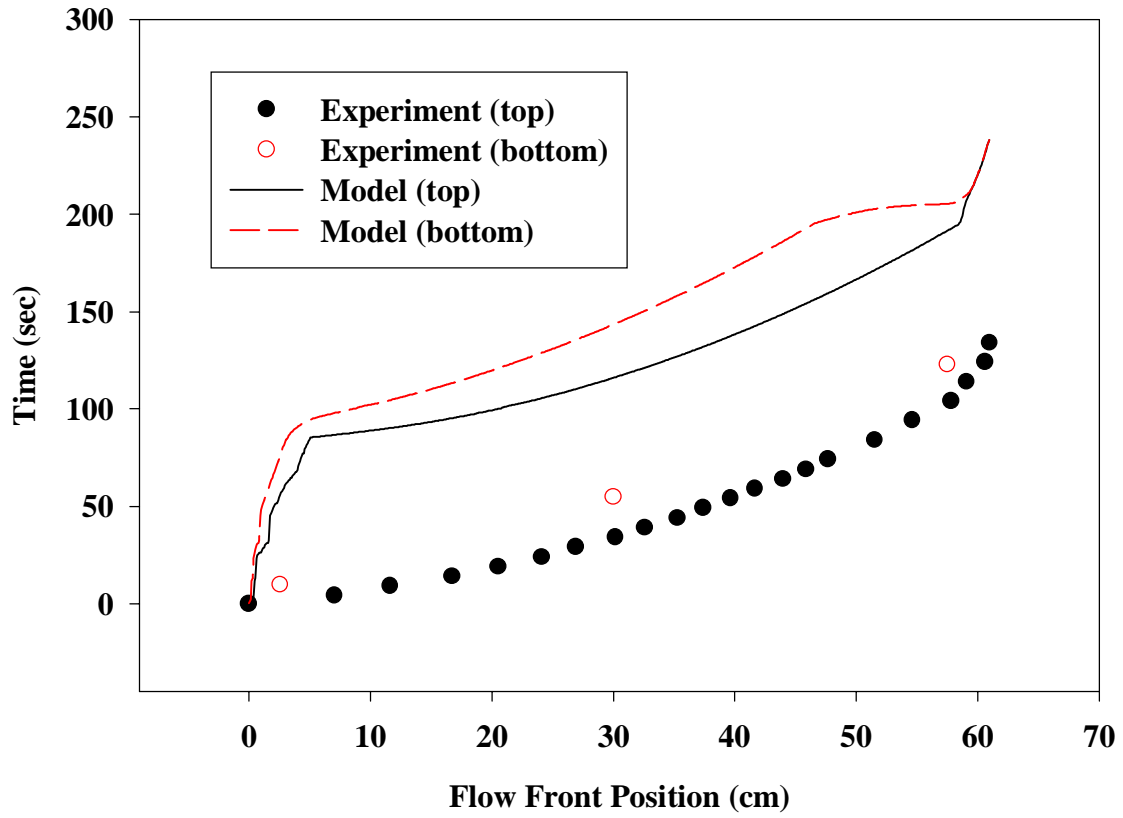
Figure 5.9: Flow front location comparison between Model I prediction and experiment measurement for Panel 1
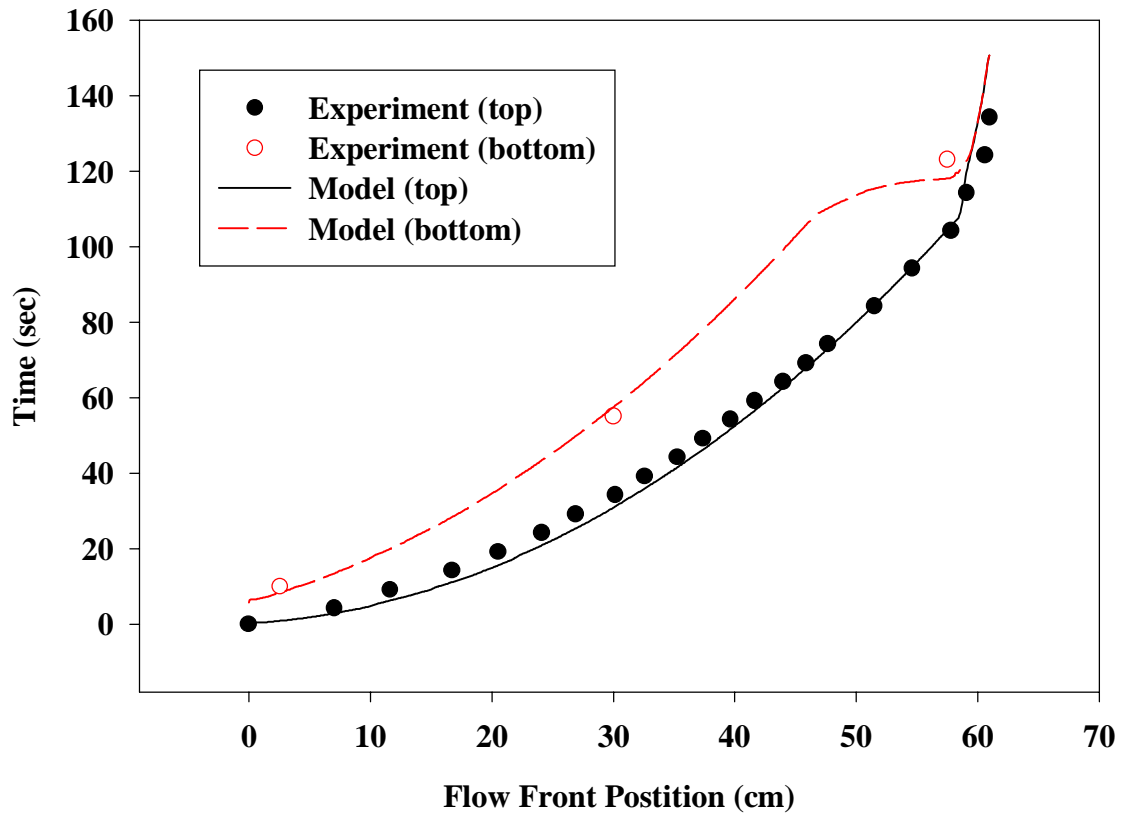
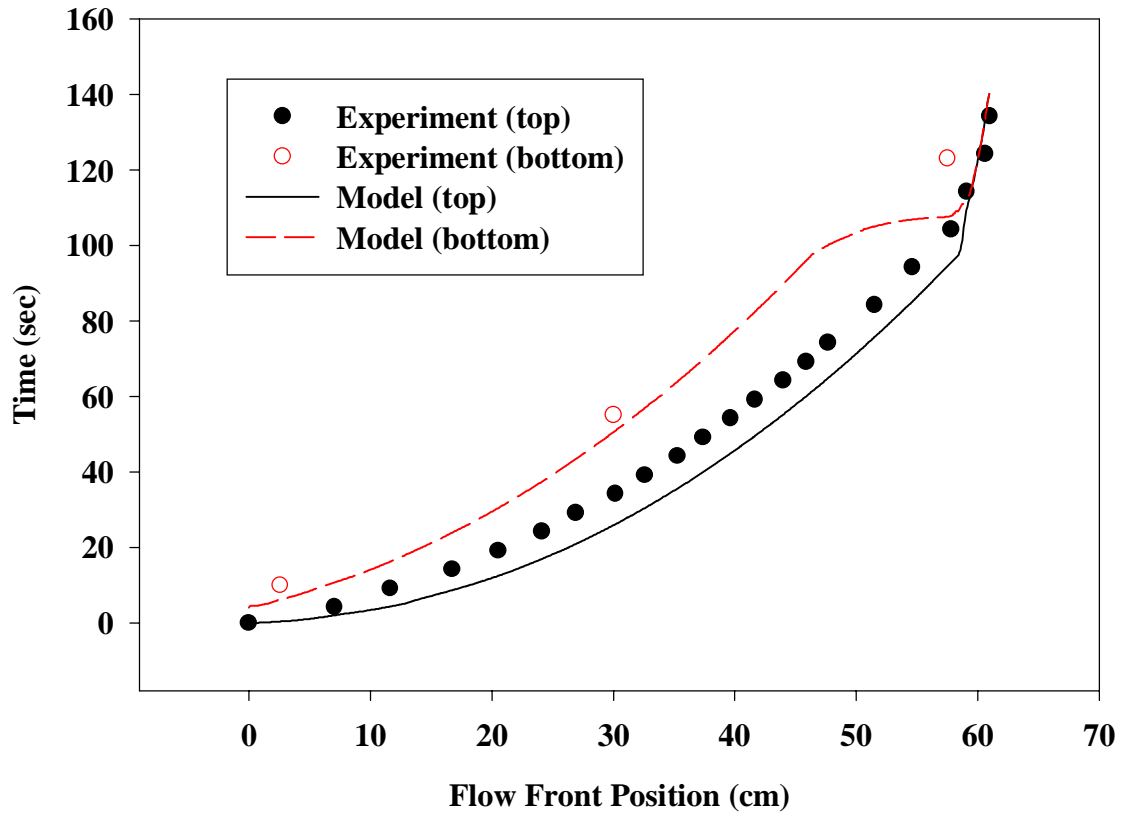Figure 5.10: Flow front location comparison between Model Ⅱ prediction and experiment measurement for Panel 1

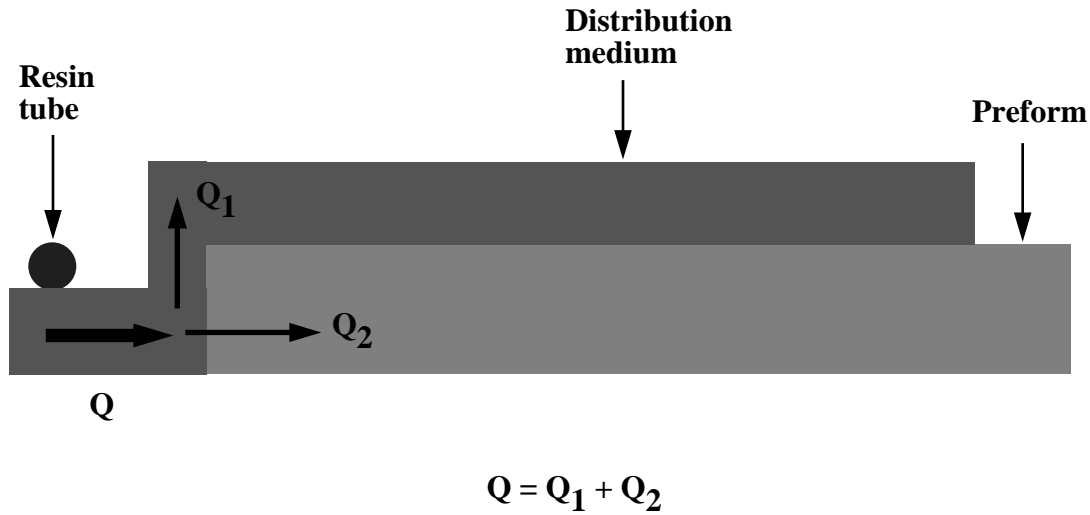Figure 5.11: Flow front location comparison between Model Ⅲ prediction and experiment measurement for Panel 1

$$Q = Q_1 + Q_2$$

Figure 5.12: Competition for resin during VARTM with the infusion scheme in Model I

mechanisms [43]. First, the lubrication effect of the resin causes rearrangement of the fiber network and an increase in the preform compaction. This mechanism is called the wetting compaction effect of the resin. On the other hand, the increase of the resin pressure leads to a decrease of the pressure applied to the preform. Consequently, the amount of the preform compaction decreases. This is called the springback mechanism. During the infiltration process, the net compaction of the preform depends on the relative magnitude of the wetting and springback deformation mechanisms. Therefore, both the simulation and the experiment find that the compaction responses of the preform at the three LVDT positions are different. D1 moderately decreased after the resin passed by, while D2 increased after the flow front approached. The model also predicted a temporary increase of the displacement D3 due to wetting compaction, although it was not observed in the experiment. After the flow front reached the end of the distribution medium, D1, D2, and D3 all decreased rapidly due to the sharp increase in the resin pressure. The sudden increase in preform thickness was observed at 115 seconds in the experiment, and the phenomenon was predicted to occur at 116 seconds in the simulation. Both the simulation and the experiment find that at the end of the infiltration process, $D1 < D2 < D3$. This indicates that the panel is less compacted on the resin inlet side and more compacted on the vacuum side.
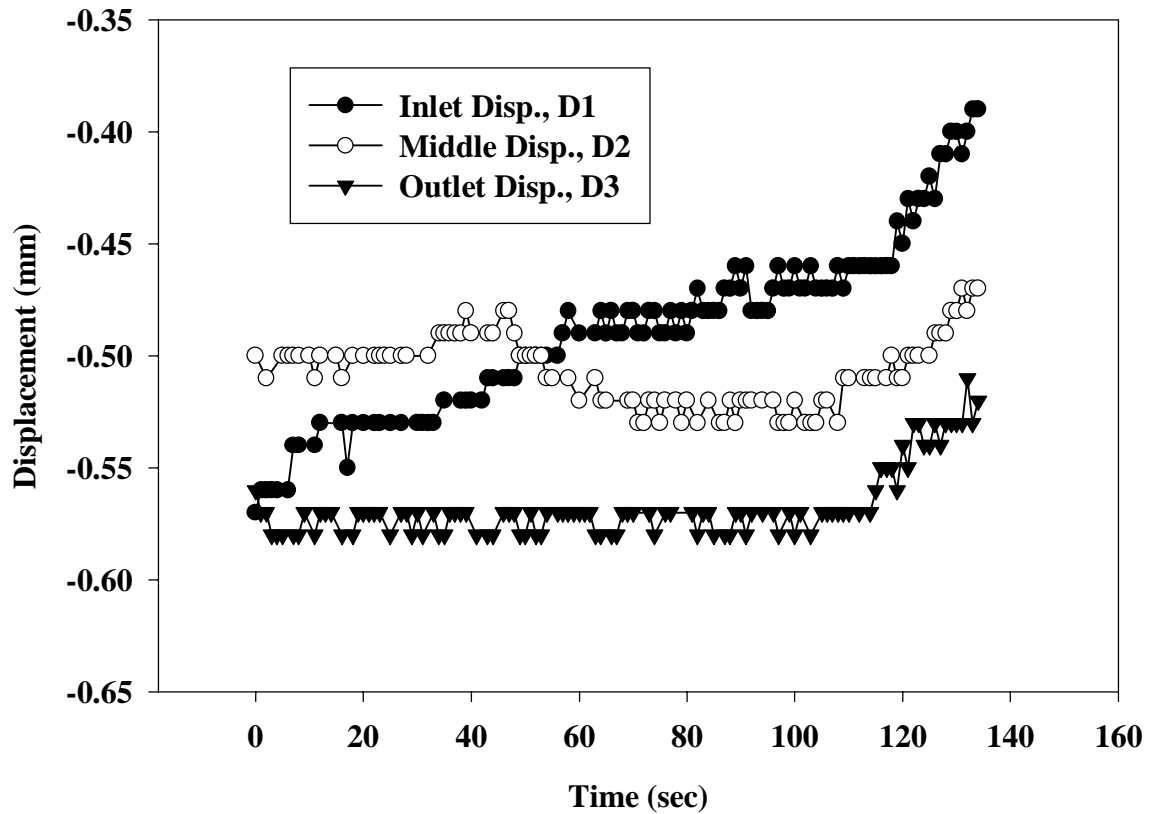
Figure 5.13: Measured displacements of Panel 1

The computed displacements do not match the measured value quantitatively. There are three reasons to explain about the differences. First, the initial thickness of the preform is not uniform. This also explains the difference between the measured initial displacements of the dry preform under the full vacuum at the three LVDT locations. The value of the initial thickness of the preform used in the simulation is the averaged thickness of the panel and this induces error. Second, the compressibility of the preform (i.e., the equations of the compressive strain as a function of the pressure) used in the simulation was measured under quasi-static conditions, which may not truly represent the actual dynamic VARTM compaction conditions. Also, the error in fitting the compaction test results contributes to the disagreements.
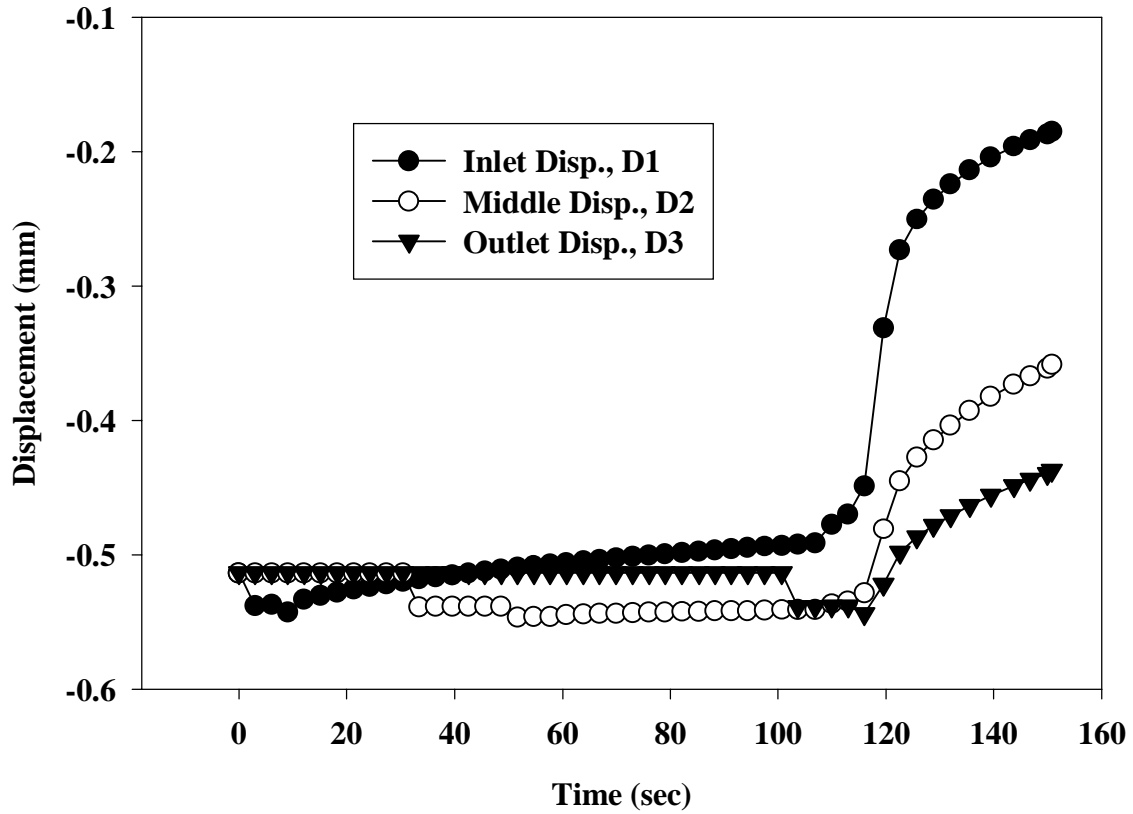
Figure 5.14: Predicted displacements of Panel 1
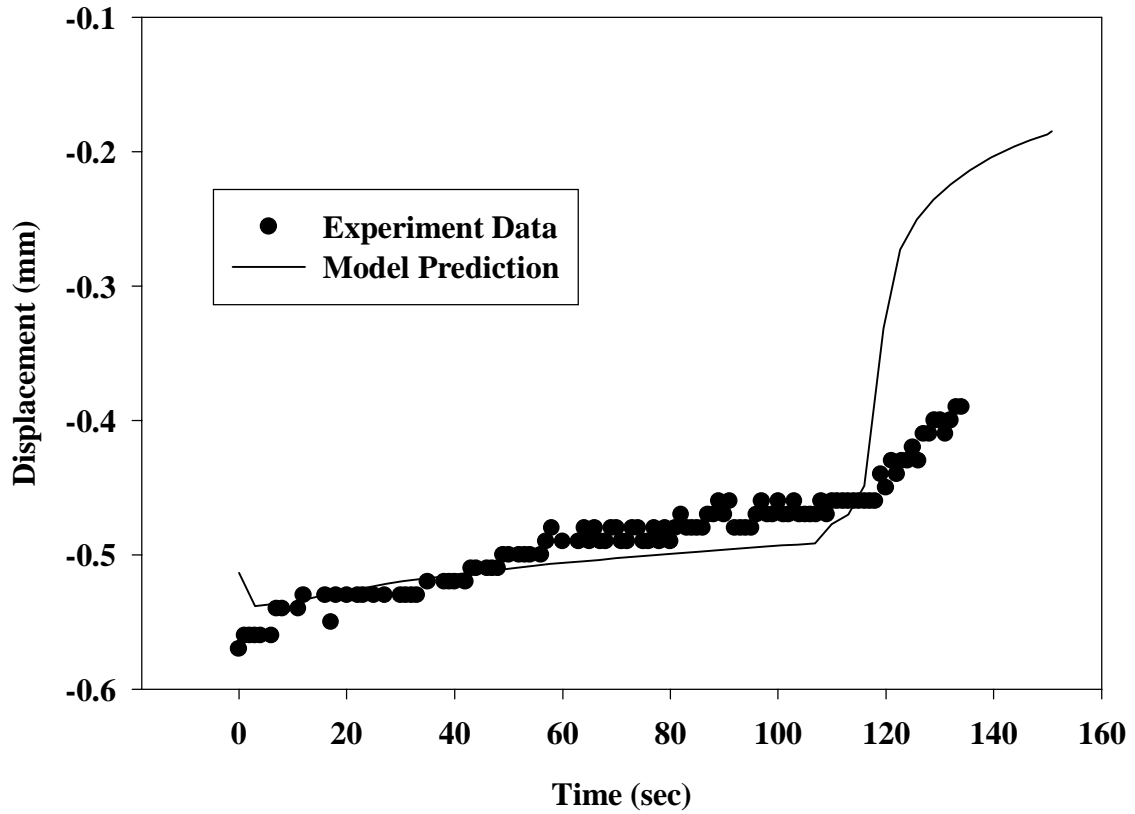
Figure 5.15: Comparison between measured and predicted D1 for Panel 1
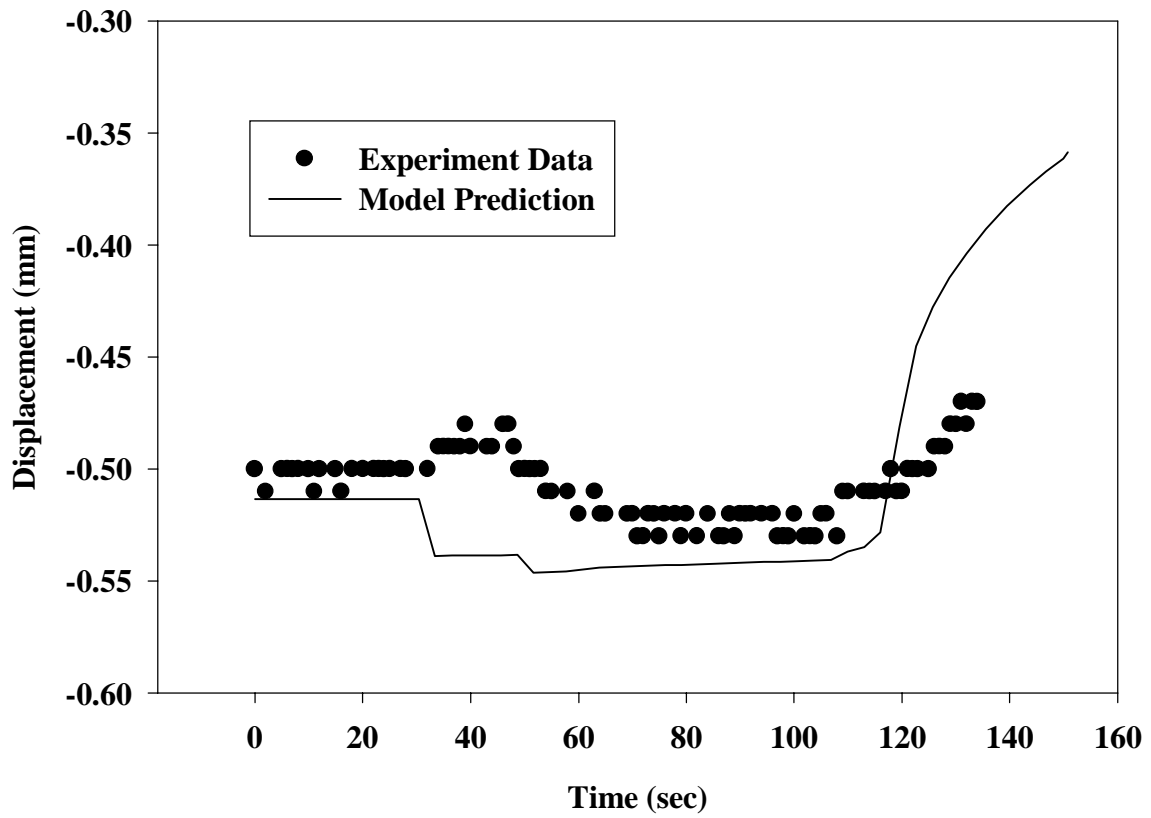
Figure 5.16: Comparison between measured and predicted D2 for Panel 1
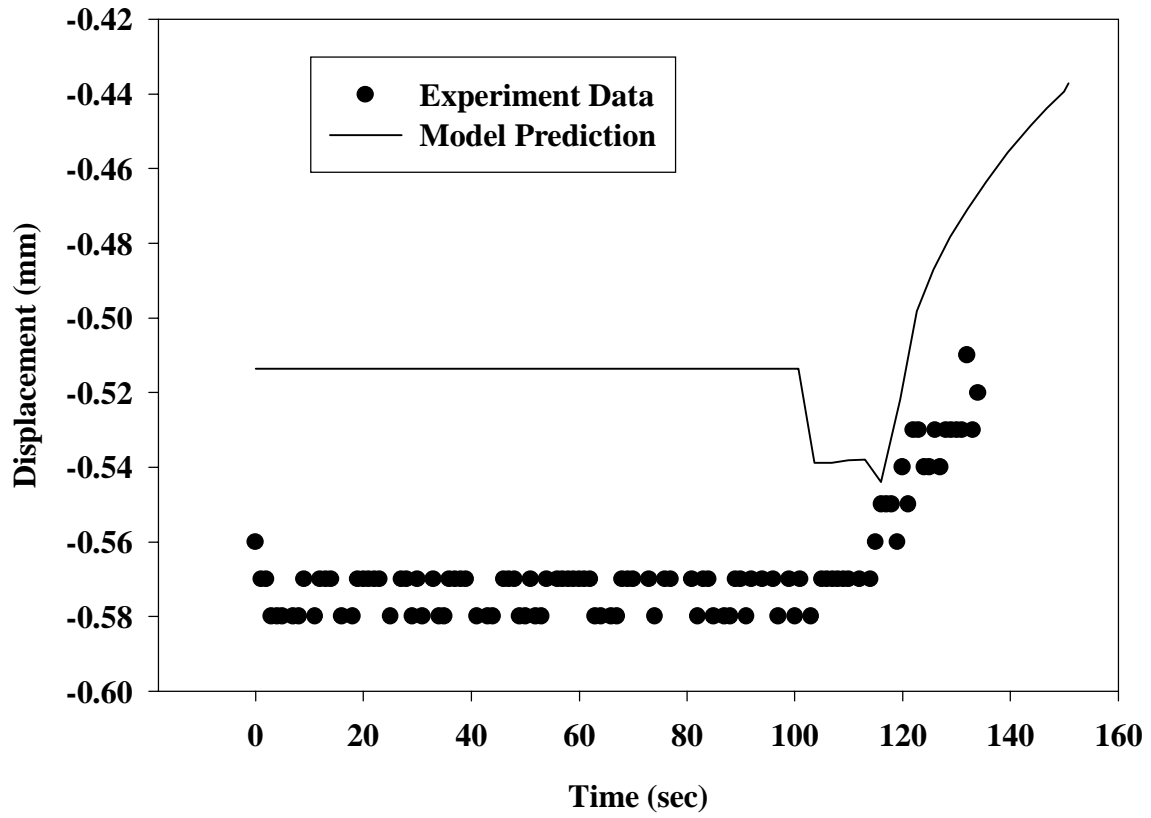
Figure 5.17: Comparison between measured and predicted D3 for Panel 1

5.3.2 Panel 2

As discussed in Section 5.3.1, model II shown in Fig. 5.8 (b) best represents the actual VARTM lay-up in the experiment, and is thereby adopted to simulate the infiltration of Panel 2, which contains 4 stacks of the SAERTEX carbon fabric.

The computed and measured infiltration times of the top and bottom resin front positions are compared in Fig. 5.18. The flow pattern predicted by the model agrees well with the measured values on the top surface before the end of the distribution medium. However, on the bottom surface, the predicted resin infiltration was much slower than measured. The reason for the disagreement is that for the unstitched preform containing more than one stack of the fabric, the permeability model used in the simulation is not accurate enough. The current permeability model is obtained by the permeability tests, and the mechanical load frame used in the tests can not hold a low compaction load. As a result, the permeability of the MAWK fabric can only be measured at a 45% or higher fiber volume fraction. The permeability of the preform with a lower fiber content was extrapolated from data points for 45% and higher fiber volume fractions. However, for preforms containing more than one stack of the fabric, when the pressure applied becomes low and the fiber volume fraction of the preform drops below 45%, the gaps between the stacks could increase significantly and form flow pathways for the resin at the interply interfaces. That is, the effective permeability of the whole structure could increase drastically when the fiber content is below 45%, and the empirical permeability model obtained from fiber volume fraction data 45% or higher does not apply any more. Note that the fiber volume fraction of the uncompressed 4-stack fabric preform is 40%. During the infiltration process, the pressure applied to the preform keeps decreasing as a result of increasing local resin pressure. Therefore, the compaction pressure becomes very low and the fiber volume fraction of the preform is then likely to be in the range between 40% and 45%, where the current permeability model can not predict the permeability of the preform accurately, which leads to the inaccurate prediction for the resin flow pattern in the preform. The 1-stack fabric preform does not have this interply interface

flow problem. Hence the permeability model works well in the simulation of VARTM process for Panel 1.

The measured and predicted transverse displacements of Panel 2 at the three LVDT positions are presented in Fig. 5.19 and Fig. 5.20, respectively. The predicted thickness change agrees well with the experiment measurement qualitatively. For Panel 2, at all the three locations, the wetting compaction mechanism dominated over the springback mechanism when the resin front approached and wetted out the preform. However, the local resin pressure kept increasing with the progression of the flow front. This led to the persistent decrease of the net pressure applied to the preform. After the maximum displacements were reached, the displacements decreased as a result of the significantly decreased compression force. Both the simulation and the experimental results show that, like Panel 1, Panel 2 is also less compacted on the resin inlet side and more compacted on the vacuum side.
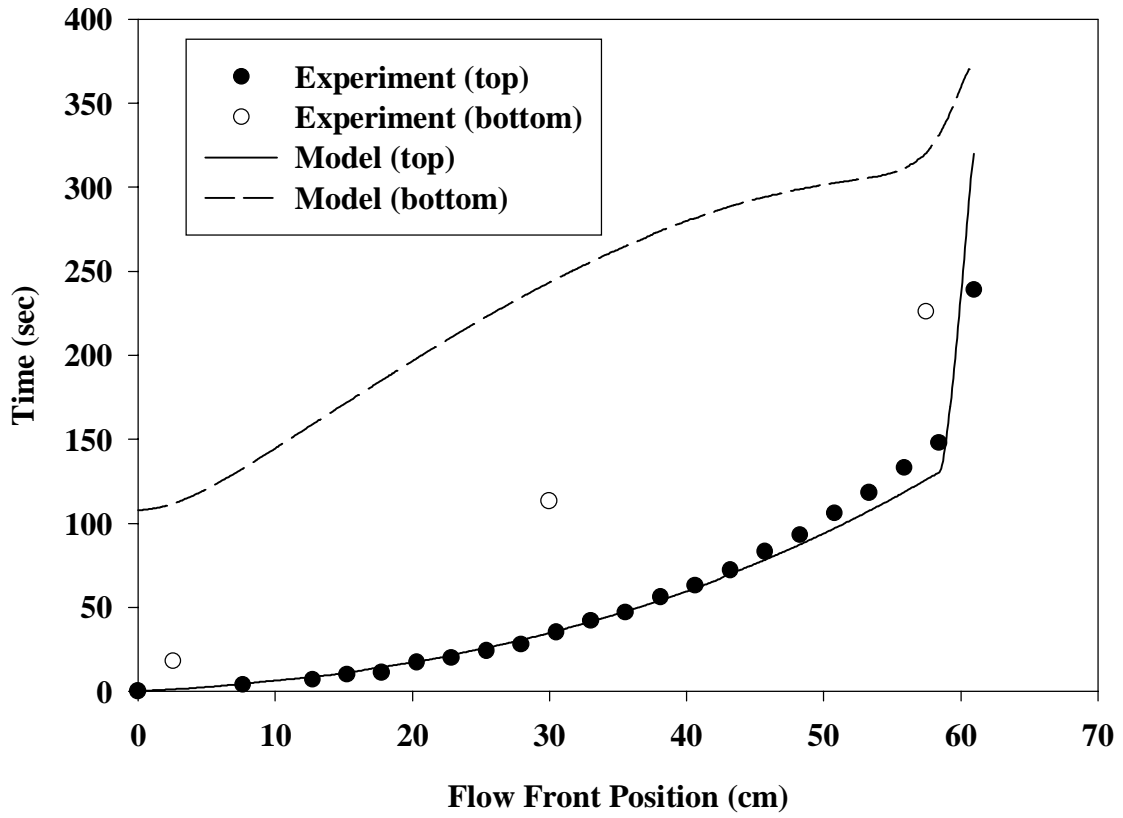
Figure 5.18: Flow front comparison between simulation and experiment for Panel 2
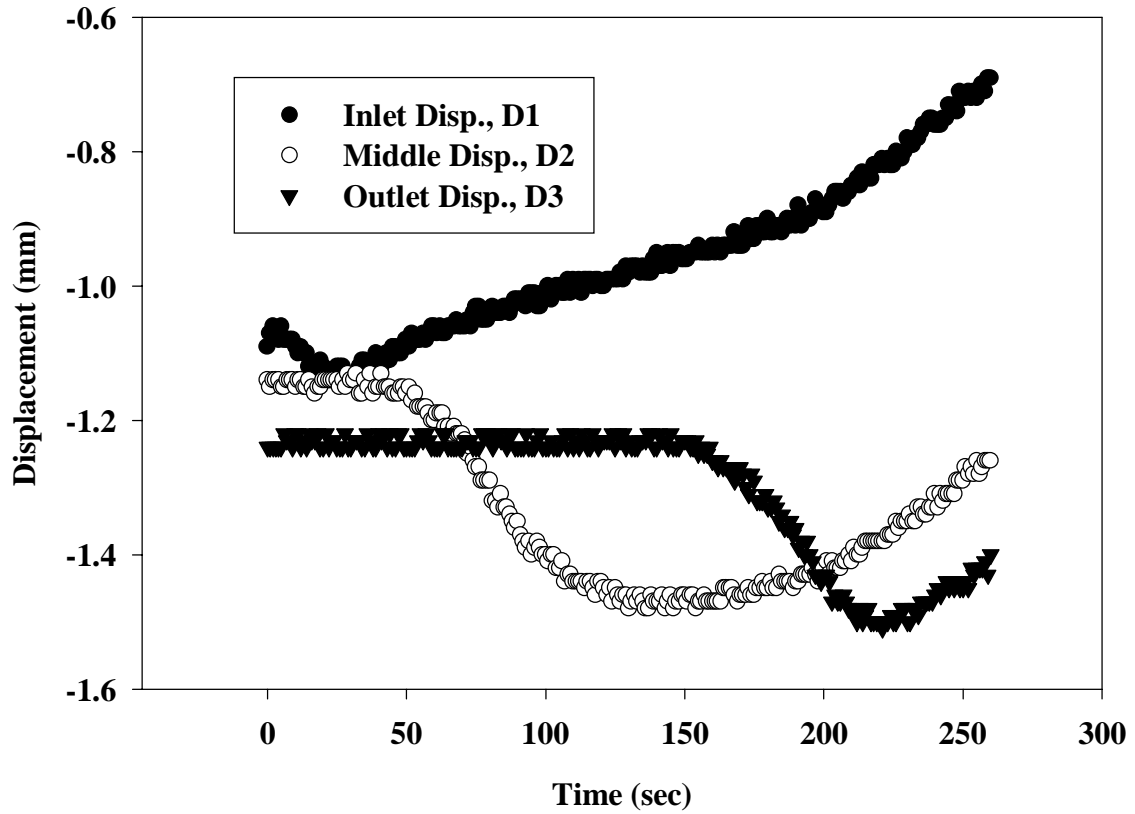
Figure 5.19: Measured displacements of Panel 2
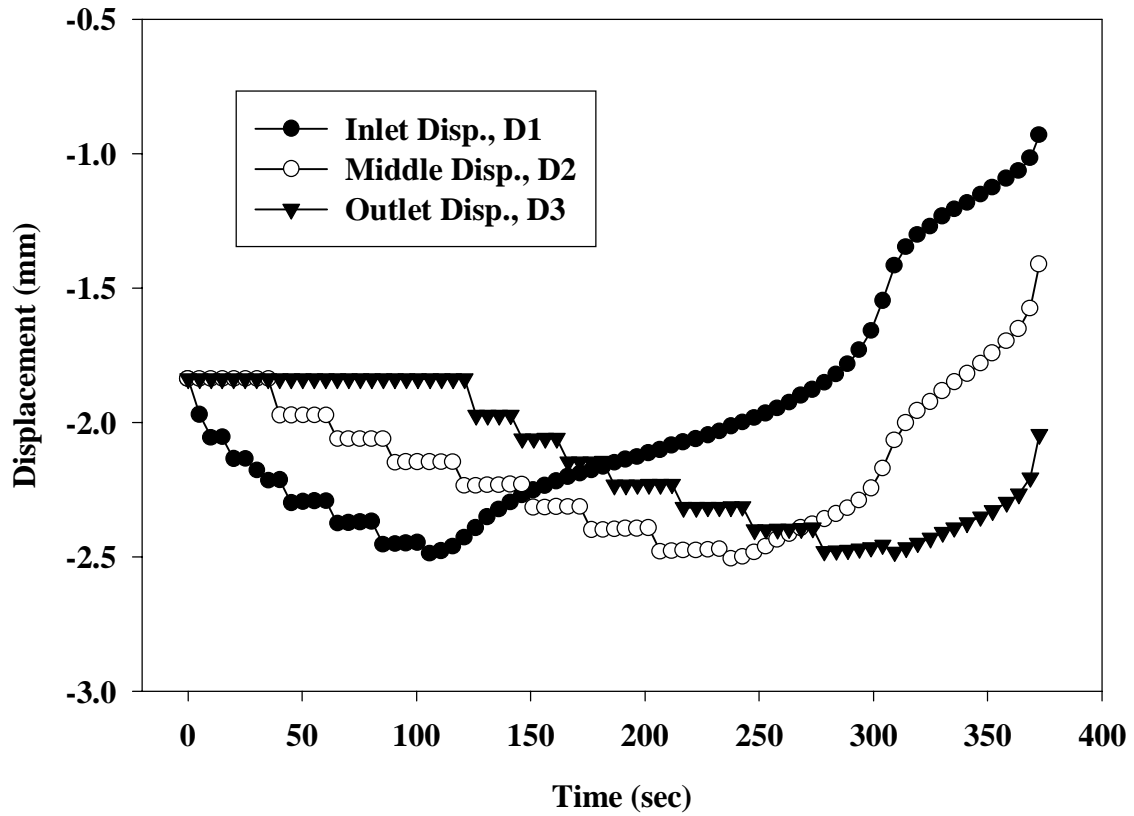
Figure 5.20: Predicted displacements of Panel 2

Chapter 6

VARTM of Sandwich Structures

Sandwich structures are being considered for use in primary aircraft structures due to their light weight and good resistance to shearing. NASA Langley Research Center is investigating a new form of sandwich structures that contain through-the-thickness reinforcement. Recent studies [47] have shown that transverse stitchings can improve damage tolerance of these structures, making them better suited for service in structural applications. It is envisioned that the stitched foam core preform could be resin infused by the VARTM process.

The primary objective in developing the VARTM process of stitched foam core sandwich structures is the complete filling of the preform with adequate wetting of the fibrous media. Thus, it is very important to investigate the details of the resin flow through the stitched foam core preforms. The VARTM simulation model developed in Chapter 3 (3DINFIL 5.0) was employed to simulate the flow field during VARTM of the stitched foam core panels. The simulation results were verified by experiments. The effect of the stitching density on the filling time and infiltration pattern was examined.

6.1 Material Characterization

The stitched foam core composite panels consisted of SAERTEX carbon fiber multiaxial warp knit face sheets attached to a Rohacell 31 IG polymethacrylimide (PMI) foam core. The face sheets and foam core were stitched together in the transverse direction using a 1600 denier Kevlar/PVA thread. The resin used in this study was a room temperature cure Dow Derakane 510A-40 vinyl ester. A plain weave nylon screen was used as the high-permeable distribution medium. The porosity and permeability of the carbon fabric and nylon screen, and the resin viscosity are required inputs for the computer model.

6.1.1 Porosity and Permeability

The SAERTEX multi axial warp knit carbon fabric contains seven layers of unidirectional carbon fibers laid up in a quasi-isotropic stacking sequence. The seven layers are knitted together, and the knitted unit is referred to as a 'stack'. The permeability of the fabric was measured using the steady-state measurement technique in a previous study [48]. The fiber samples used in the permeability tests contain 8 stacks of the carbon fabric, which were stitched together through the thickness using a modified lock stitch and Kevlar thread. The stitch rows were 5.08 mm apart, and the stitch step was 3.75 mm. Assuming that the material has orthotropic flow properties, permeability measurements were made in the three mutually perpendicular principal directions. For the stitched carbon fabric, these directions are in-plane parallel to the stitching, in-plane normal to the stitching, and transverse to the stitching (TTT) direction. The permeability of the carbon fabric varies with fiber volume fraction. The power law equation was used to fit the permeability data in each direction:

$$S = a(V_f)^b \tag{6.1}$$

where S is the permeability in m^2, V_f is the fiber volume fraction, and a and b are fit constants. The fit constants are listed in Table 6.1, and Fig. 6.1 shows the power-law fit

Table 6.1: Fit constants in the permeability model for stitched SAERTEX carbon fabric [48]

	a	**b**
‖ to stitching	9.03×10^{-15}	-12.18
⊥ to stitching	3.27×10^{-15}	-12.53
TTT	1.26×10^{-14}	-7.95

curves for the permeability parallel, normal, and transverse to the stitching as a function of fiber volume fraction.

The permeability model was coded into the material database of the computer simulation package, 3DINFIL 5.0. With given fiber volume fraction, the permeability of the carbon face sheets could be calculated by the code. In this study, the fiber volume fraction (V_f) of the carbon face sheets were assumed to be constant and took the value of 0.53. Accordingly, the porosity (ϕ) of the carbon fabric was calculated to be 0.47 using the following equation:

$$\phi = 1 - V_f \tag{6.2}$$

Sayre [40] measured the porosity and permeability of the nylon screen used as the distribution medium. By examining the geometry of the distribution medium and calculating the ratio of the open cross-sectional area to the total cross-sectional area, the porosity of the nylon screen was determined to be 0.51. In the permeability measurement, a radial flow, advancing front technique with a center-port injection was first used to determine the orientation of the in-plane principal directions for the permeability tensor. The circular flow patterns were observed in the radial infiltration test and this indicated that the nylon screen is in-plane isotropic. One-dimensional advancing front technique was then used to measure the in-plane permeability of the distribution medium, which was found to be $2.92E - 09 \ m^2$.

The nylon screen is very thin and thus, the transverse direction fills immediately as the fluid flows in the in-plane directions. This condition prohibits that any realistic transverse permeability measurements be performed. Therefore, the transverse permeability was
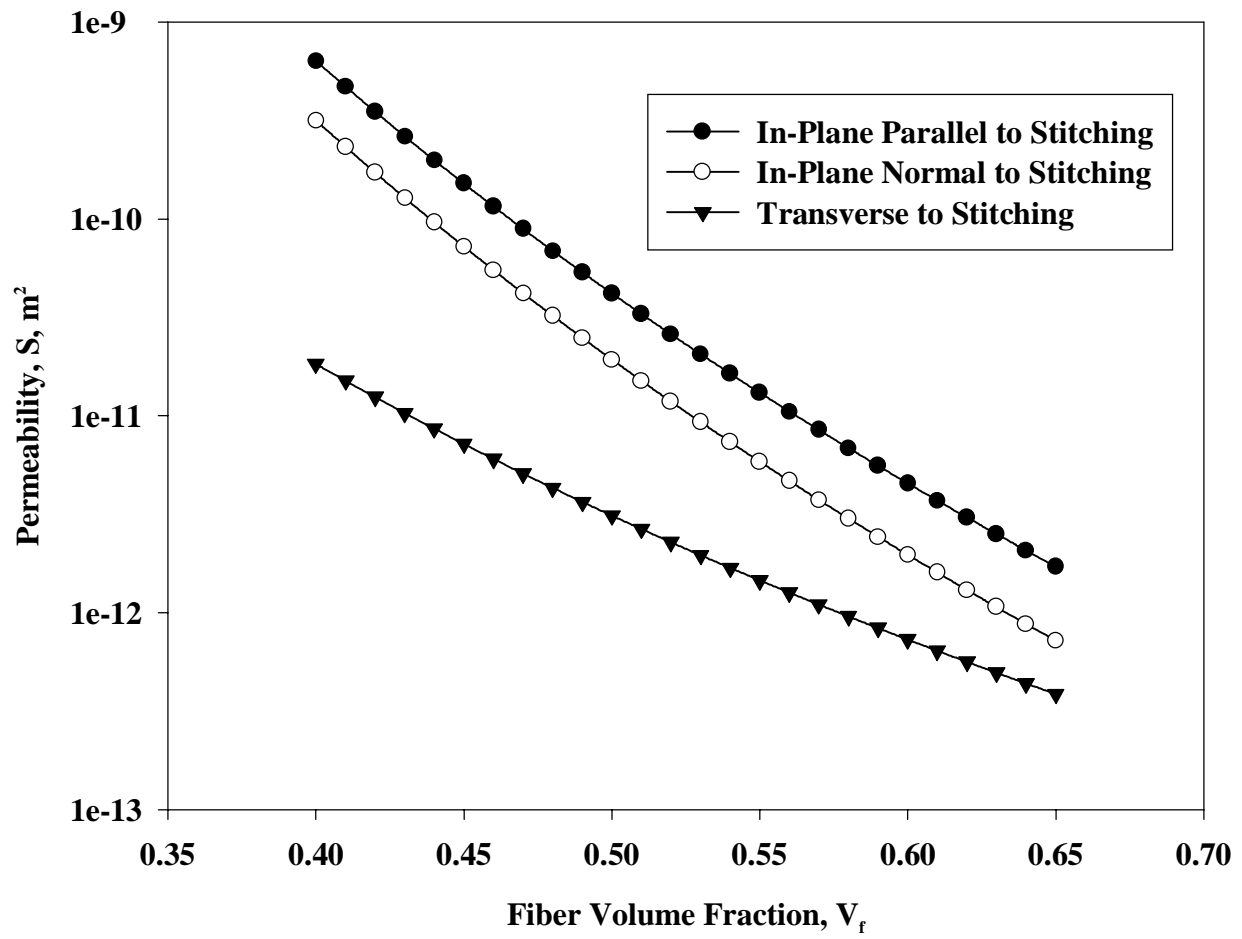
Figure 6.1: Permeability of stitched SAERTEX carbon fabric

arbitrarily assumed to be $1.0E - 08 \ m^2$ [40].

6.1.2 Resin Viscosity

As described in Chapter 3, the resin viscosity (μ) is often characterized as a function of temperature (T) and degree of cure (α):

$$\mu = f(T, \alpha) \tag{6.3}$$

The degree of cure (α) of the resin varies with temperature (T) and time (t):

$$\alpha = g(T, t) \tag{6.4}$$

Substituting eqn. 6.4 into eqn. 6.3 yields

$$\mu = f(T, g(T, t)) \tag{6.5}$$

Therefore, the resin viscosity (μ) can be modeled as a function of temperature (T) and time (t):

$$\mu = \mu(T, t) \tag{6.6}$$

Because injection of the sandwich panels with 510A-40 vinyl ester was performed at room temperature, the resin temperature is assumed to be constant during the VARTM process. Thus, the resin viscosity model used in the study can be further simplified and takes the form of the following relation:

$$\mu_r = \mu_r(t) \tag{6.7}$$

where μ_r is the resin viscosity at room temperature.

Experiments were conducted to determine the viscosity model of the Dow Derakane 510A-40 vinyl ester. The viscosity measurements were made with a Brookfield Model DV-
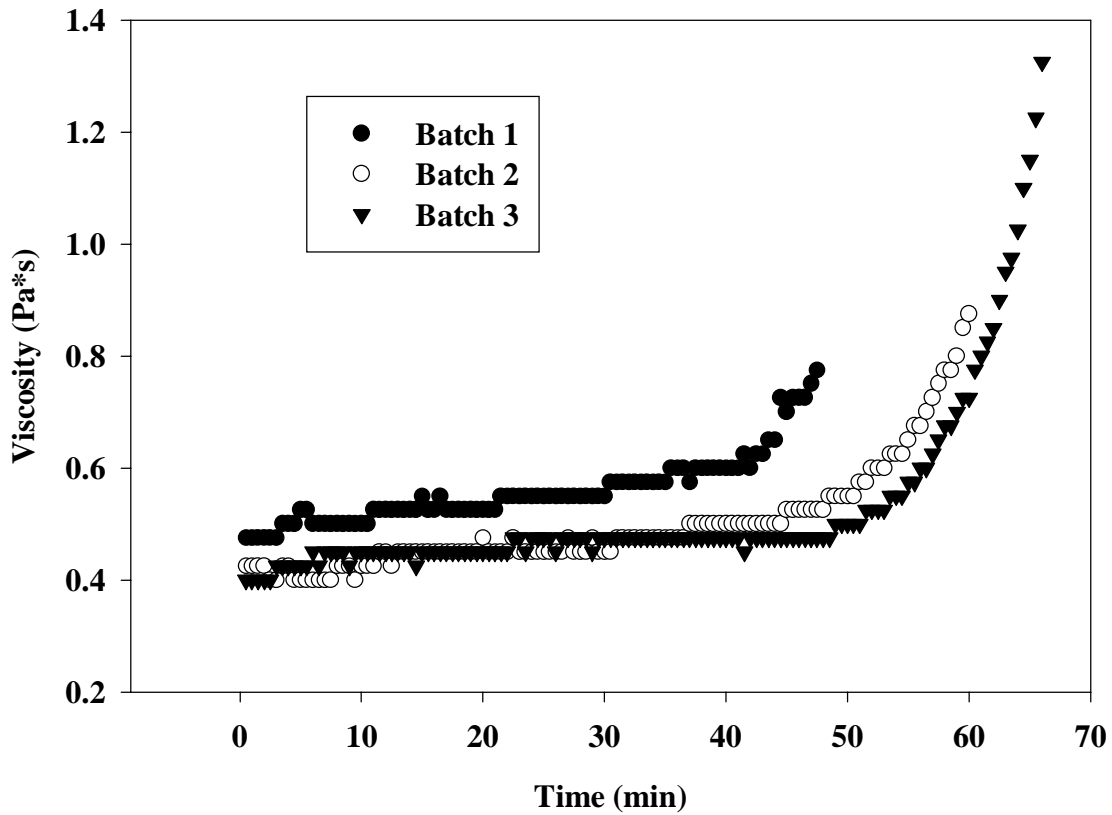
Figure 6.2: Viscosity trace of Derakane 510A-40 resin with 0.2% CoNap and 1.0% MEKP

III Concentric Cylinder Digital Rheometer. Isothermal measurements at room temperature were conducted. The vinyl ester resin was mixed with a cobalt napthenate catalyst at 0.2 weight % and a methyl ethyl ketone peroxide (MEKP) promoter at 1.0 weight %. Three different batches of the vinyl ester were used in the VARTM of the sandwich structures. Each has a subtle difference in the resin viscosity, and thus the viscosity of each batch was evaluated. Fig. 6.2 shows the measured viscosity as a function of time for the three batches of 510A-40 vinyl ester resin. The initial viscosities for the three batches were $0.475\,Pa \cdot s$, $0.425\,Pa \cdot s$, and $0.4\,Pa \cdot s$, respectively. The resin gelled after approximately 45 minutes. To avoid incomplete impregnation of the preform, the mold must be filled before the resin gels.

6.2   Experiment

A dry, stitched foam core preform consists of two 3mm thick carbon face sheets attached to a polymerthacrylimide (PMI) foam core by stitching through the thickness of the preform with a 1600 denier Kevlar/PVA thread. Three preforms with different stitch row spacings were resin injected to evaluate the effect of the stitch density on the filling time and infiltration pattern. These included stitch row spacings of 6.25 mm, 12.7 mm, and 25.4 mm. The pitch was held constant at 4 stitches per 25.4 mm. All the preforms were approximately 30.5 cm wide and 64.5 cm long and used a 12.7 mm thick foam core.

A VARTM process for resin infiltration of stitched foam core preforms was developed. The stitched foam core preform was placed on a glass tool plate. The tool plate was treated with a release agent over the area on which manufacturing took place. The glass plate was set on a transparent polycarbonate table. The glass tool plate and transparent polycarbonate table were selected in order to observe resin infiltration into the lower face sheet of the preform. A porous peel ply was placed directly on top of the preform. Then, a nylon high-permeable distribution medium was placed on top of the peel ply and aligned with the injection edge of the panel. The distribution medium was cut to leave approximately a 25.4 mm space between the edge of the medium and the vacuum edge of the preform and 12.7 mm from the sides of the medium and the sides of the preform. A resin distribution tube was placed on top of the distribution medium at a distance of 25.4 mm from the edge. The resin distribution tube was prepared by drilling 3.18 mm diameter holes 25.4 mm apart. The number of holes was determined by the width of the panel. One end of the tube was plugged with a brass fitting. A typical lay up of the VARTM experiment is shown in Fig. 6.3.

After the lay-up was completed, glass bleeder/breather material was cut to the same width as the preform and placed on the tool plate at the end opposite to the resin tube. The entire assembly was then sealed in a vacuum bag. A vacuum port was centered on the bleeder/breather materials. The other end of the resin tube was plugged and a vacuum was applied to expel any air. The entire assembly is shown in Fig. 6.4.
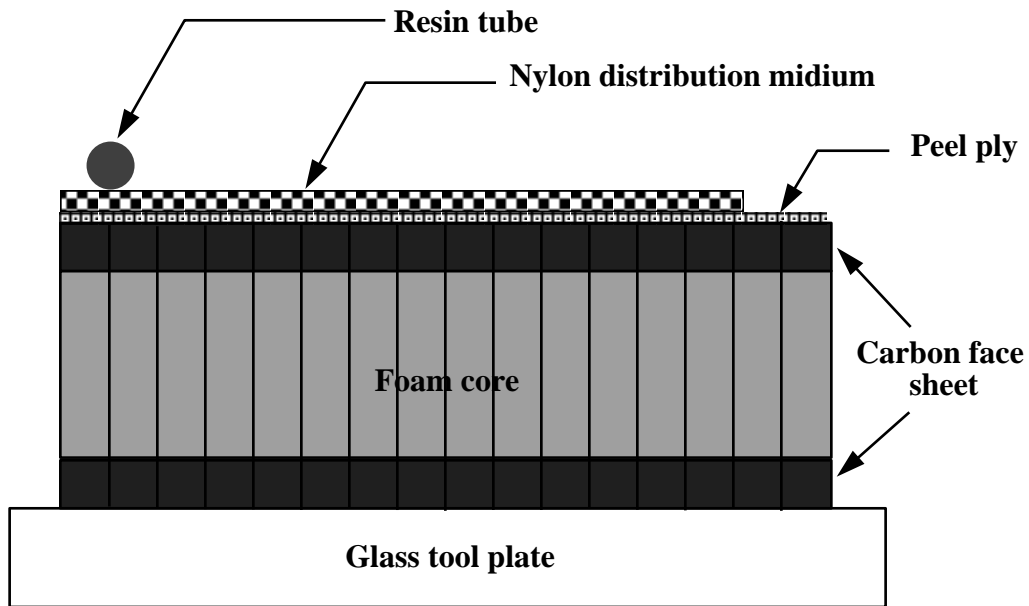
Figure 6.3: Schematic diagram of the VARTM lay-up for the infiltration of the stitched foam core sandwich panel
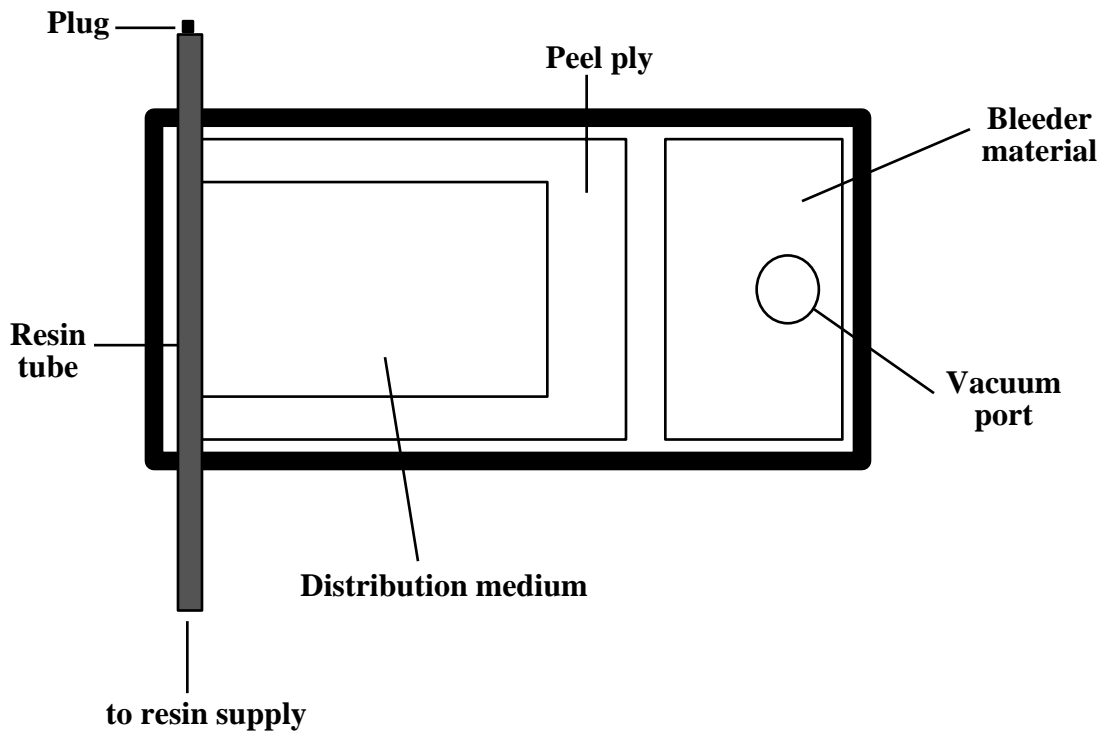

Figure 6.4: VARTM processing set-up for a stitched foam core composite panel

Derakane 510A-40 vinyl ester resin was used in this study. Approximately 1300g resin was used to inject the 30.5 cm x 64.5 cm panels. The vinyl ester resin with 1.0 % MEKP and 0.2 % cobalt napthanate has a processing time of approximately 45 minutes at room temperature. Prior to injection, the resin was allowed to degas. Once the system was equilibrated and all air leaks were eliminated, the resin tube was placed into the resin source and the infusion process began. After the preform was completely infiltrated, the resin distribution tube was clamped off while the vacuum source was left on until the part completely gelled. The panel was then cured at room temperature for 24 hours before removing from the mold.

Flow visualization experiments were conducted to record the flow front positions in the upper and lower carbon face sheets. In order to measure the flow front position in the upper and lower carbon face sheets, straight lines were drawn at measured intervals on the surface of the vacuum bag and on the bottom surface of the glass tool plate, respectively. The complete preform layup with grid markings is shown in Fig. 6.5. Visual observations were made in two ways. On the top surface, a digital camera was used to capture images of the flow front as a function of time. A minute/second timer was used to record the infiltration time. The timer was started when the resin filled the resin distribution tube. Then, as the flow reached a grid mark, the time was recorded and a digital image was captured. Using an angled mirror, the images from the bottom surface were reflected and recorded using a video camera. Subsequent flow front position versus time readings was determined from review of the videotape.

6.3 Simulation Model

The resin infiltrates the preform in two ways. First, the resin moves across the high-permeable distribution medium, infiltrates the top face sheet, flows through the non-porous foam by 'leaking' through the holes created by the needle penetrations of the stitching, and finally infiltrates the bottom face sheet. Therefore, in order to simulate resin infiltration of
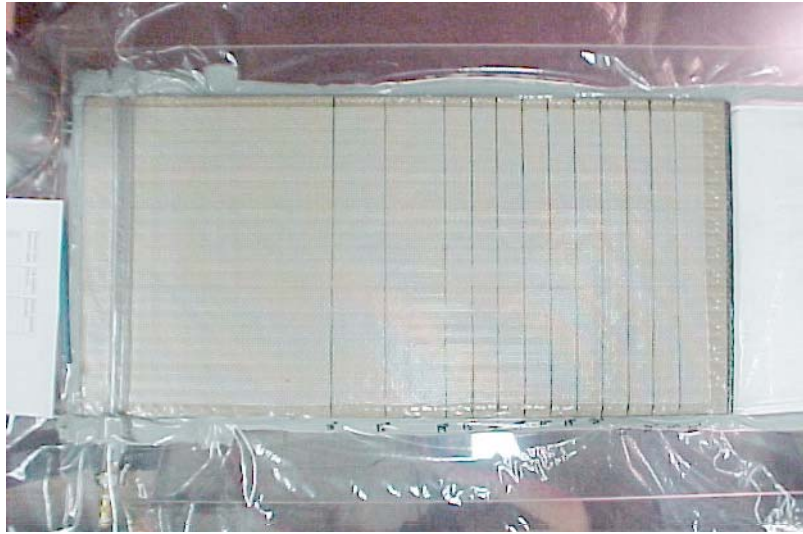
Figure 6.5: Experimental setup of a stitched preform. The grid marks are used to determine the flow front location as a function of time

stitched foam core sandwich structures, a finite element mesh was created including a high-permeable distribution medium, and two porous multiaxial warp knit face sheets connected by the transverse stitches. The closed-cell nature of the PMI foam core makes it impervious to fluid, thus the foam core is excluded from the resin flow model.

6.3.1   Model of the Resin Flow along the Transverse Stitching

Resin leaks through the needle penetrations of the stitching to infiltrate the preform in the transverse direction. The resin path along the stitches from the upper face sheet to the lower face sheet can be seen in a cross-sectional view of the stitching in Fig. 6.6. Therefore, the resin flow along each transverse stitch can be regarded as one-dimensional flow and 1-D rod elements can be used to model the stitches. This type of finite element model was named as 'the channel model', where the needle penetrations in the foam core were described by a series of channels that permit 1-D resin flow from the upper to the lower face sheet. However, the finite element mesh for the channel model is very large and results in expensive computational coast. For example, a panel of the dimension 30.5 cm $\times$ 64.5 cm with the

stitch row spacing of 6.25 mm and the pitch of 4 stitches per 25.4 mm contains about 4365 transverse stitches, and requires more than 10000 nodes in the whole finite element mesh. Therefore, a 'strip model' was proposed to simulate the resin flow in the stitched sandwich panel more efficiently. In the strip model, instead of modeling the single stitches using the 1-D rod elements, a two-dimensional strip encompassing the transverse stitching was used to represent one row of stitching. The channel model and strip model are compared in Fig. 6.7. By setting the permeability normal to the transverse stitching threads to be zero, these strips allow resin flow in the transverse direction of the foam core only.
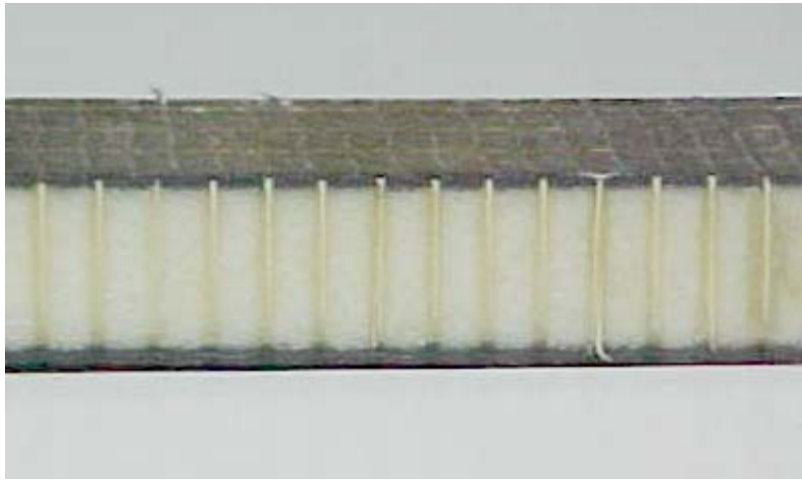
Figure 6.6: Cross sectional view of stitching, resin flow from top face sheet to bottom face sheet along the stitching

The strips have the same dimensions of 61.9 cm × 1.27cm. The thickness of the strips was assumed to be 1.60 mm, which is the diameter of the holes created by the needle penetrations of the stitching. With one strip representing one row of stitching, the panel with the 6.35 mm stitch spacing has a total of 44 strips, the panel with the 12.7 mm stitch spacing has a total of 23 strips, and the panel with the 25.4 mm stitch spacing has a total of 12 strips.

The porosity of each strip is determined by considering the ratio of the pore area to the total area of the strip as follows:

$$\phi = \frac{A_{pores}}{A_{strip}} \tag{6.8}$$
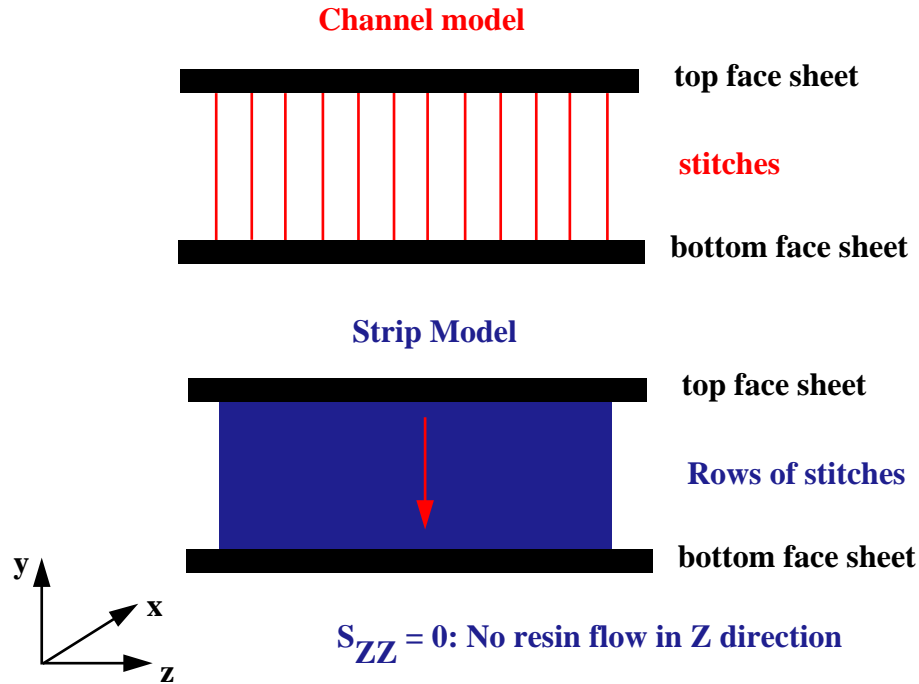
Figure 6.7: Schematic of the channel model and strip model

The area of the pores is calculated by considering the area of the hole made by the needle and subtracting the area of the stitching threads through the holes:

$$A_{pores} = n \times (A_{hole} - A_{thread}) \tag{6.9}$$

where, n is the total number of transverse stitches encompassed in one strip, A_{hole} is the area of the needle penetration and A_{thread} is the area of the reinforcing kevlar thread. Using equations 6.8 and 6.9, the porosity of the strips was determined to be about 0.18.

It is difficult to measure the permeability of the porous region (i.e., strips) in the foam core by experiments. Therefore, a theoretical model, straight capillary model [49] was modified to estimate the transverse permeability of the strip. The model is illustrated in Fig. 6.8. The porous strip is represented by a bundle of straight parallel 'capillary unit'. The capillary unit is a circular hole holding a concentric cylinder in it as shown in Fig. 6.9. The radius of the cylinder, r_1, is less than the radius of the hole, r_2. The circular hole represents
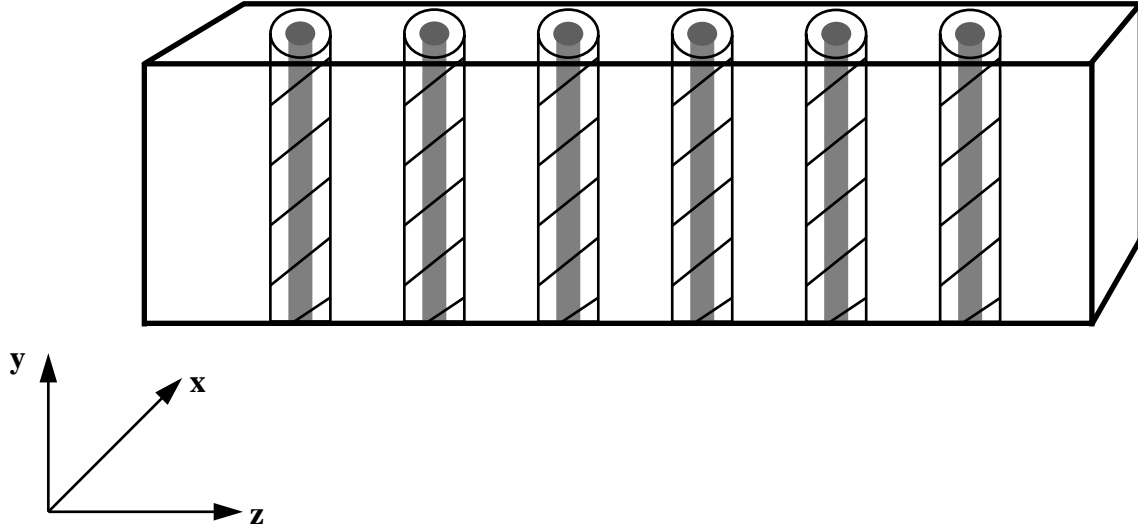
Figure 6.8: Modified straight capillaric model

the hole created by the needle penetration of the stitching and the cylinder represents the thread through the hole. The flow Q through a capillary unit is then given by solving the Navier-Stokes equations:

$$Q = -\bar{S}\frac{1}{\mu}\frac{dP}{dy} \tag{6.10}$$

where

$$\bar{S} = 2\pi \int_{r_1}^{r_2} (\frac{1}{4}r^3 + C_1 r \ln r + C_2 r) dr \tag{6.11}$$

C_1 and C_2 are defined as

$$C_1 = \frac{r_1{}^2 - r_2{}^2}{4(\ln r_2 - \ln r_1)} \tag{6.12}$$

$$C_2 = \frac{r_1{}^2 \ln r_2 - r_2{}^2 \ln r_1}{4(\ln r_1 - \ln r_2)} \tag{6.13}$$

μ is the viscosity and $\frac{dP}{dy}$ the pressure gradient along the capillary unit.

If there are n such capillary units in the strip, the flow per unit area of cross-section of the strip, q will be

$$q = -\frac{n\bar{S}}{A_{strip}}\frac{1}{\mu}\frac{dP}{dy} \tag{6.14}$$
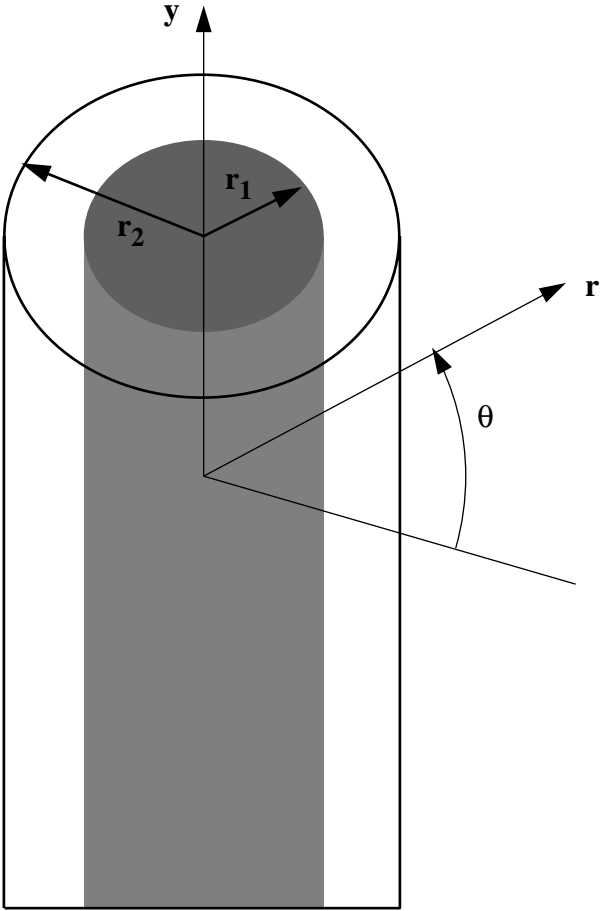
Figure 6.9: A capillary unit

As the flow can also be expressed by Darcy's law

$$q = -\frac{S}{\mu}\frac{dP}{dy}$$ (6.15)

It follows that

$$S = \frac{n\bar{S}}{A_{strip}}$$ (6.16)

The permeability of the strip in transverse direction was calculated to be $4.02E - 9\ m^2$.

6.3.2 Finite Element Mesh

The finite element meshes for the three sandwich panels are shown in Fig. 6.10, Fig. 6.11, and Fig. 6.12, respectively. 3-D hexahedral elements were used to discretize the distribution medium and carbon face sheets, and 2-D quadrilateral elements were used for the simulation of resin flow in the porous region (i.e., strips) of the foam core. Table 6.2 lists number of elements and nodes used in the simulation model.

Table 6.2: Number of elements and nodes used in the simulation models

Stitch row Spacing (mm)	Number of 2-D elements	Number of 3-D elements	Total number of elements	Number of nodes
6.35	2160	3744	5904	7934
12.7	1656	2600	4256	5558
25.4	864	2032	2896	4057
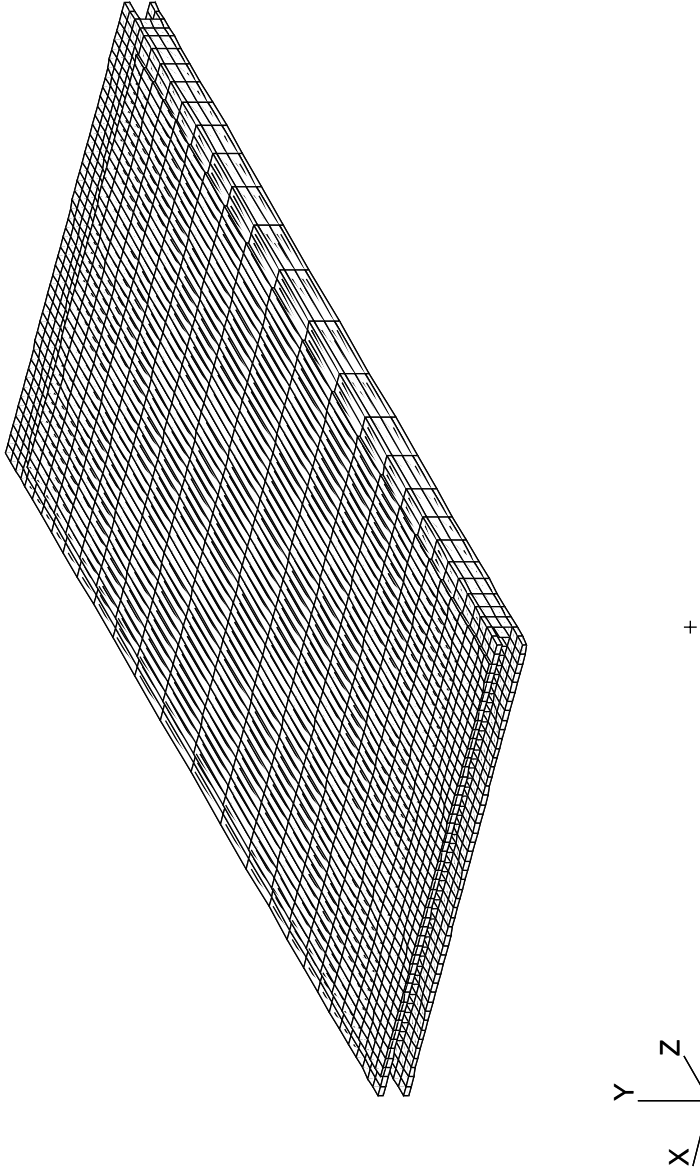
Figure 6.10: Finite element mesh for the stitched foam core preform with 6.35 mm stitch row spacing
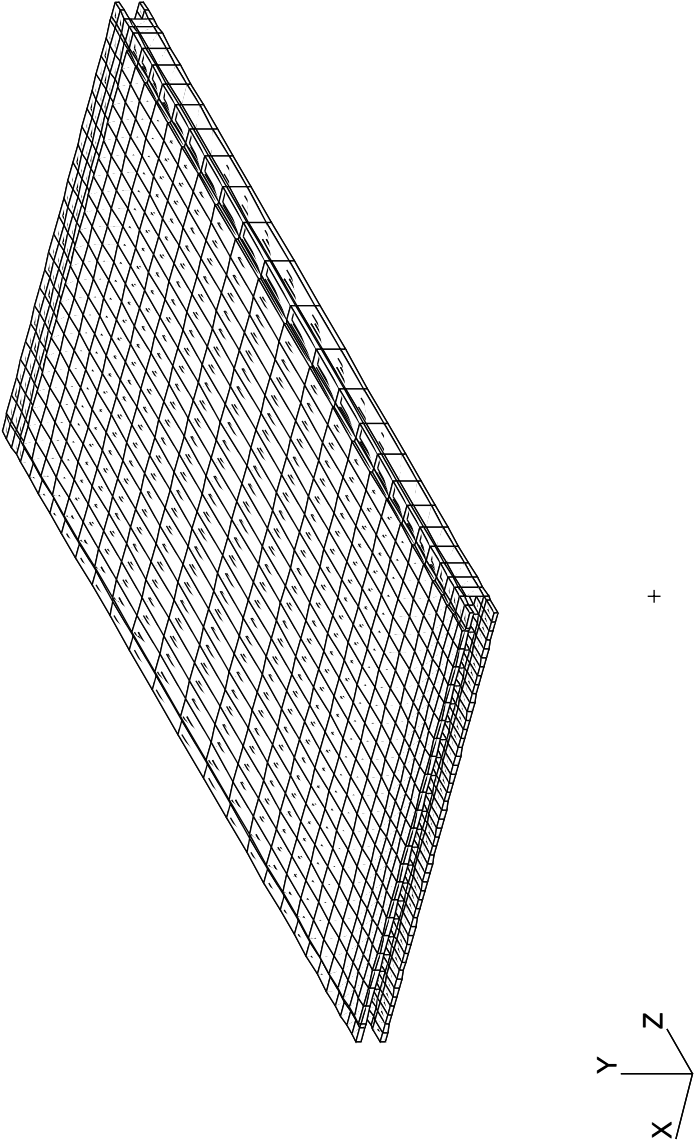
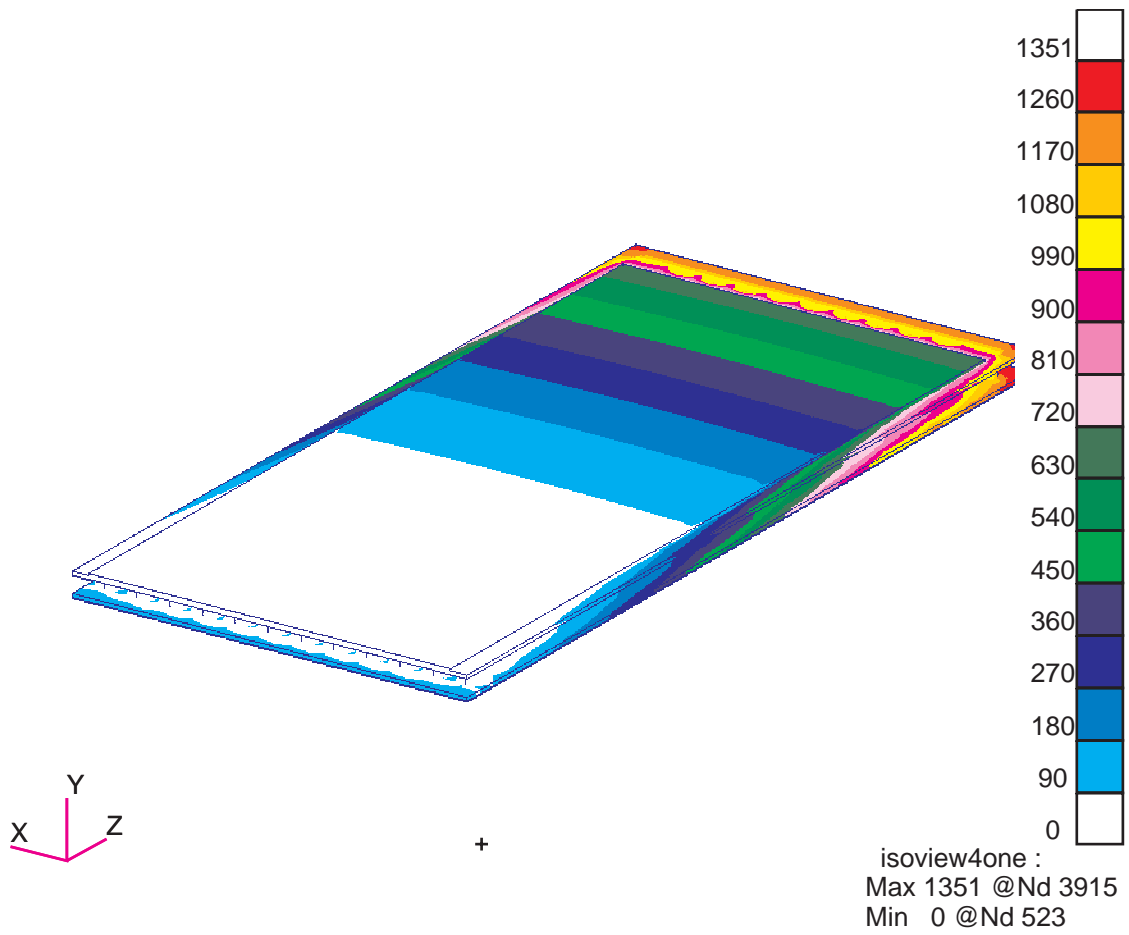Figure 6.11: Finite element mesh for the stitched foam core preform with 12.7 mm stitch row spacing
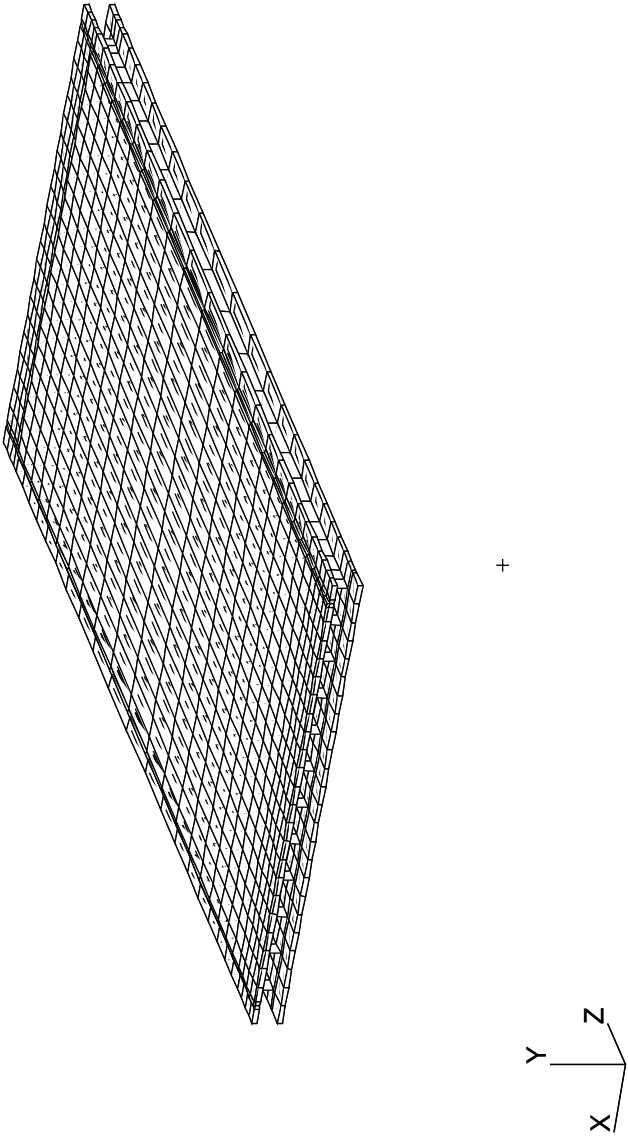
Figure 6.12: Finite element mesh for the stitched foam core preform with 25.4 mm stitch row spacing

6.4 Results

Three stitched preforms with different stitch row spacings were resin injected to examine the effect of the stitching density on the infiltration pattern and filling time. The stitch row spacings were 6.35 mm, 12.7 mm, and 25.4 mm, respectively.

The predicted flow front locations for the three preforms are shown in Figures 6.13 – 6.15. In the figures, the color bands represent the flow front location at different times, and the units are in seconds. During the infusion process, the resin first moves across the high-permeable distribution medium and infiltrates the top carbon face sheets, and then 'leaks' through the stitch paths to wet out the bottom face sheets.
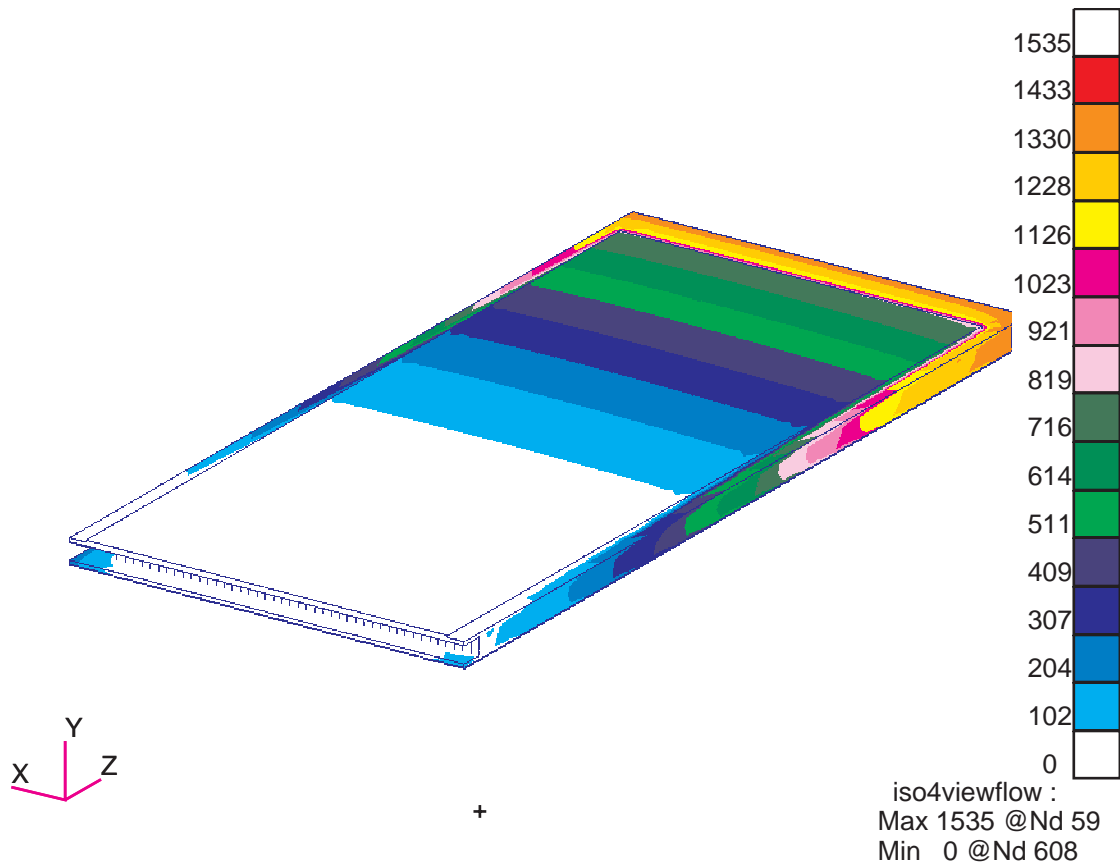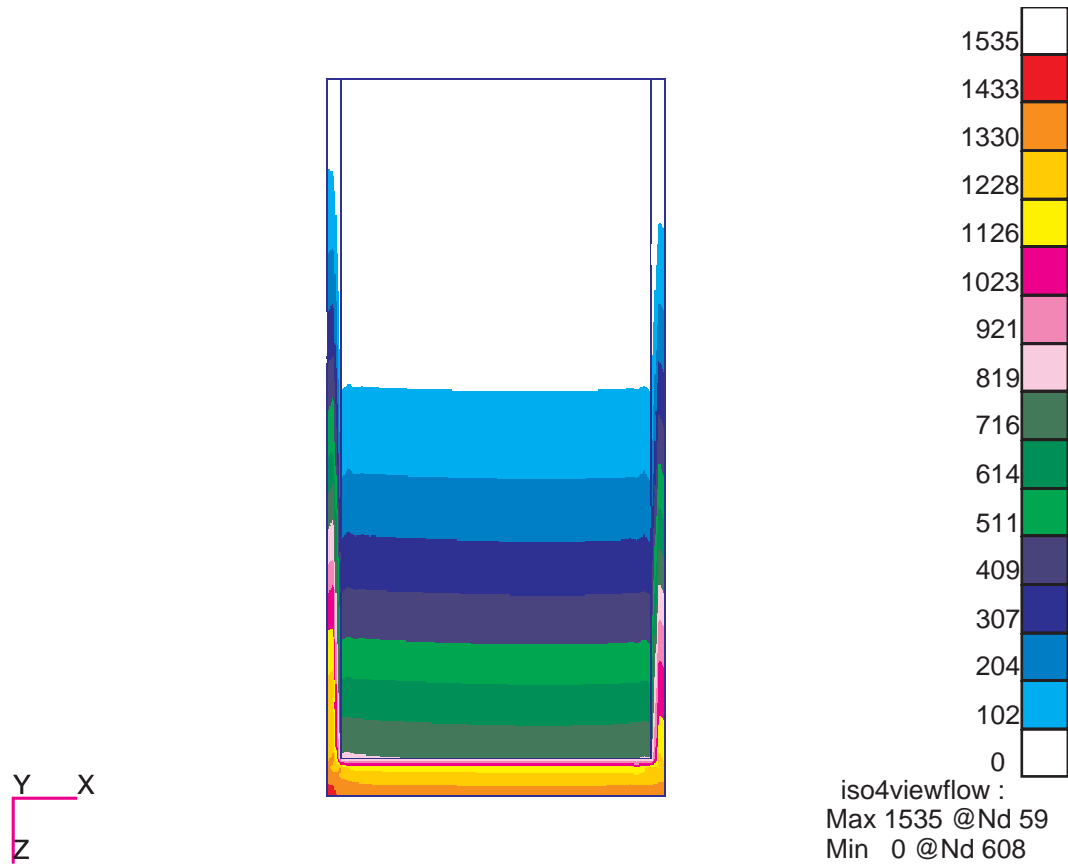

Figure 6.13: Predicted flow front progression in the stitched foam core preform with 6.35 mm stitch row spacing
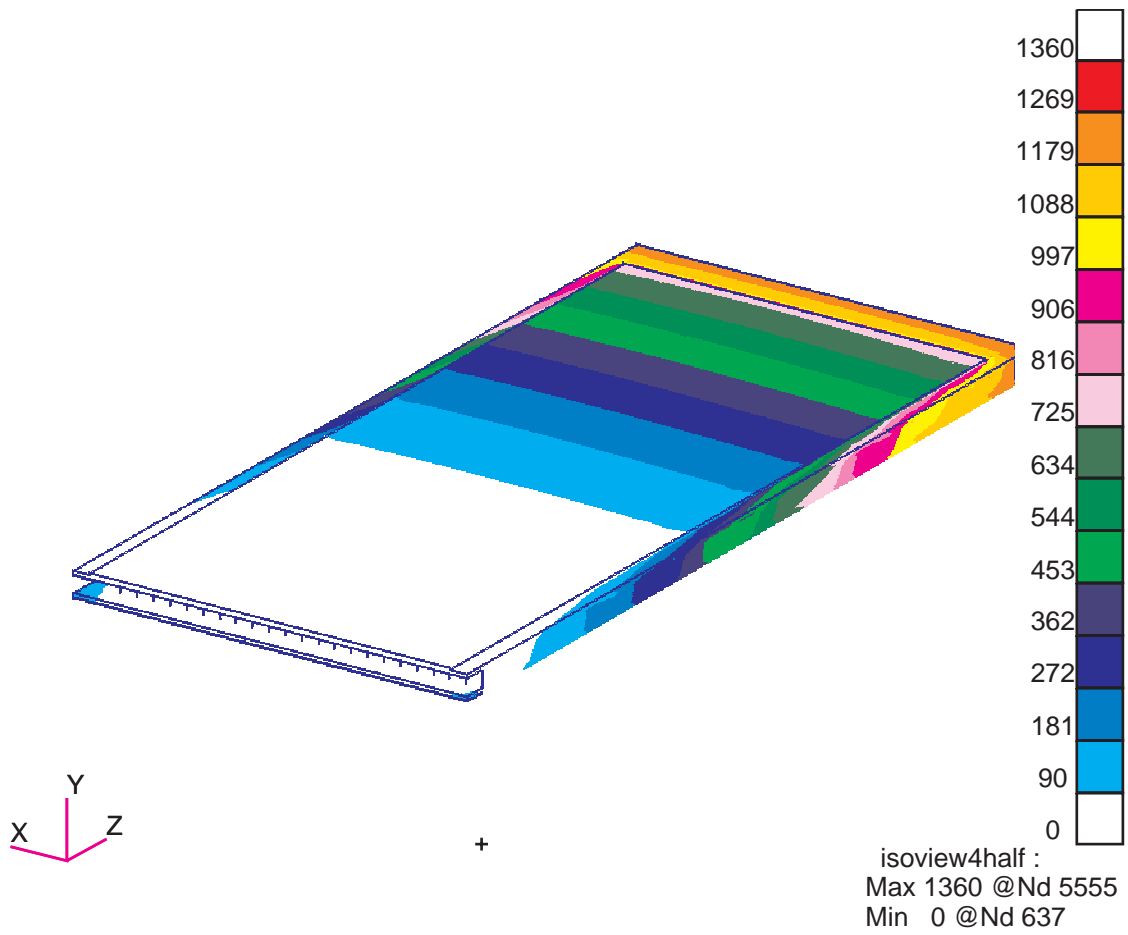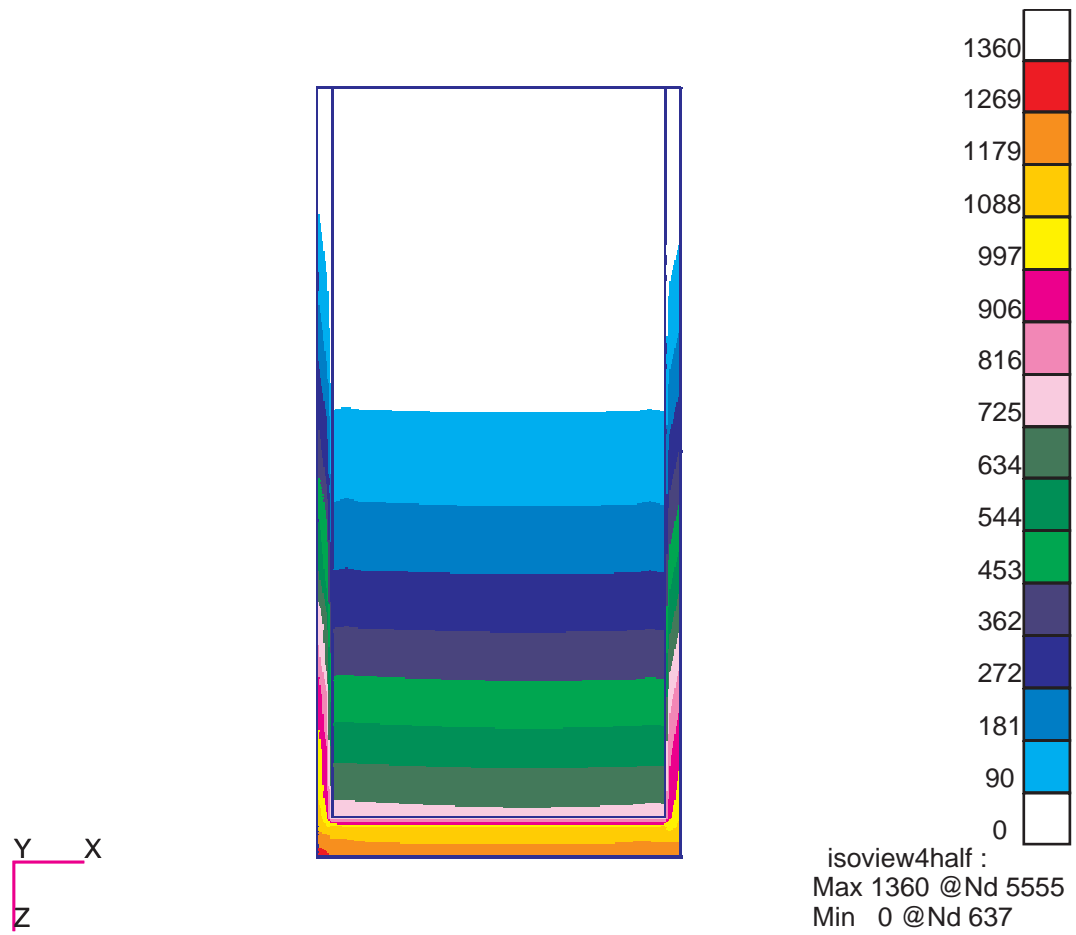
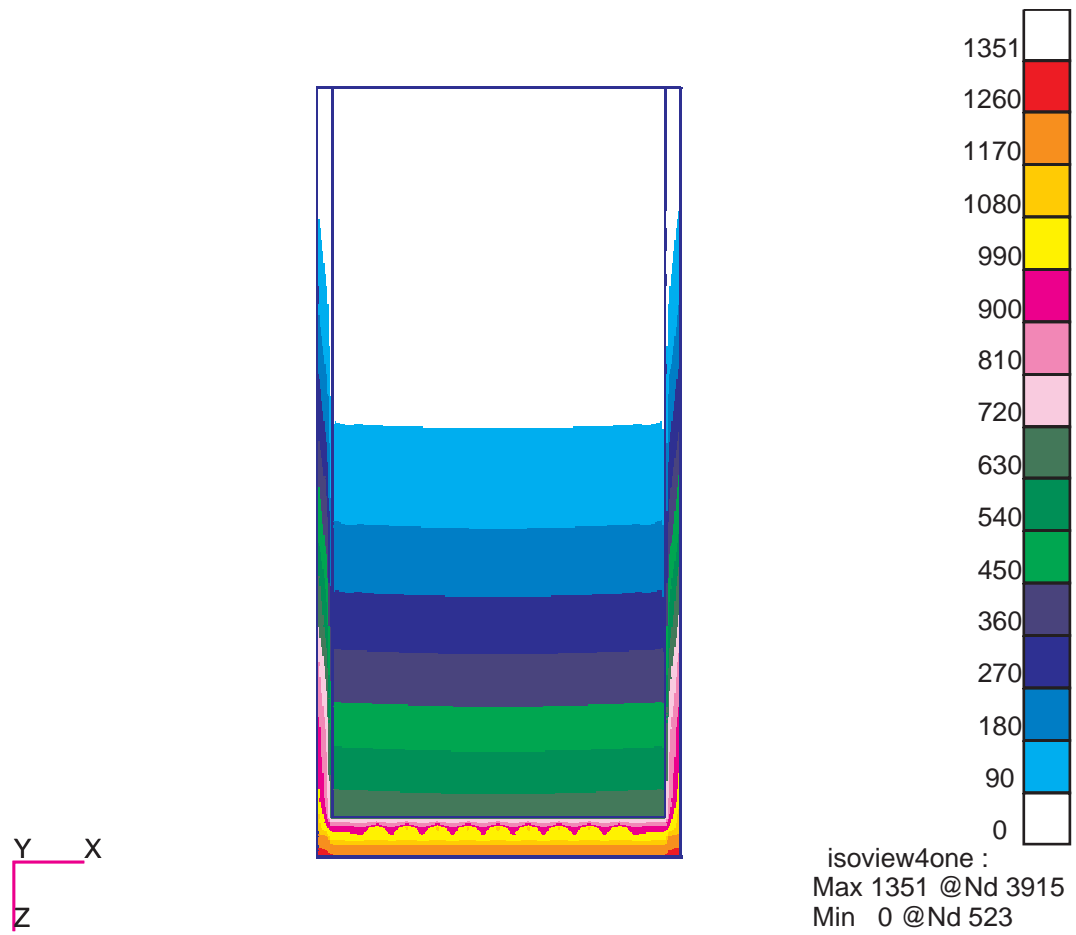Figure 6.14: Predicted flow front progression in the stitched foam core preform with 12.7 mm stitch row spacing

Figure 6.15: Predicted flow front progression in the stitched foam core preform with 25.4 mm stitch row spacing

Both the digital images captured in the experiment and the flow front fringe plot predicted by the simulation show that the infiltration pattern on the top surfaces of the preform are quite uniform for all the three panels with different stitch row spacings. The predicted infiltration pattern in the top surfaces of the three preforms are shown in Figures 6.16 – 6.18. Figures 6.19 through 6.26 show the experimentally observed progression of the flow front at the surface of the top face sheet of the preform with stitch row spacing of 12.7 mm. Note that the flow is much slower along the edges of the panels because there is no distribution medium. Shown in Figures 6.27 – 6.29 are comparisons between the measured and predicted flow front locations as a function of time for the top surfaces of the preforms. The model prediction agrees with the experimental results fairly well.

Figure 6.16: Predicted flow front progression in the top surface of the stitched foam core preform with 6.35 mm stitch row spacing

Figure 6.17: Predicted flow front progression in the top surface of the stitched foam core preform with 12.7 mm stitch row spacing

Figure 6.18: Predicted flow front progression in the top surface of the stitched foam core preform with 25.4 mm stitch row spacing
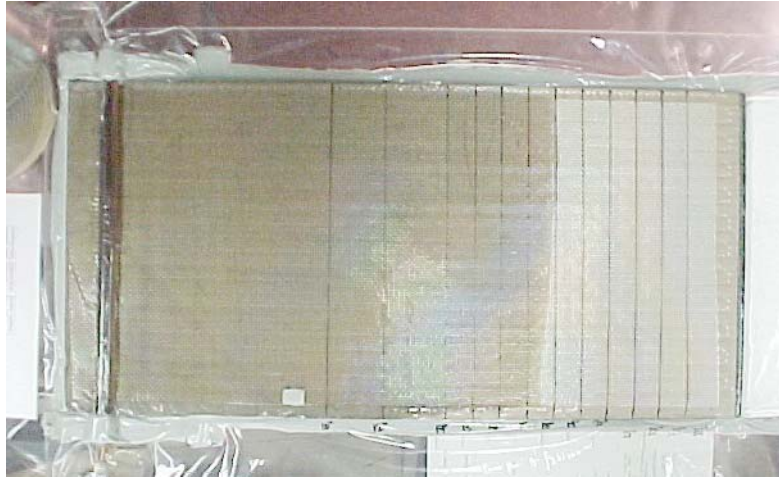
Figure 6.19: Top surface of stitched foam core preform with 12.7 mm stitch row spacing. Flow front is approximately 25.4 cm from injection edge
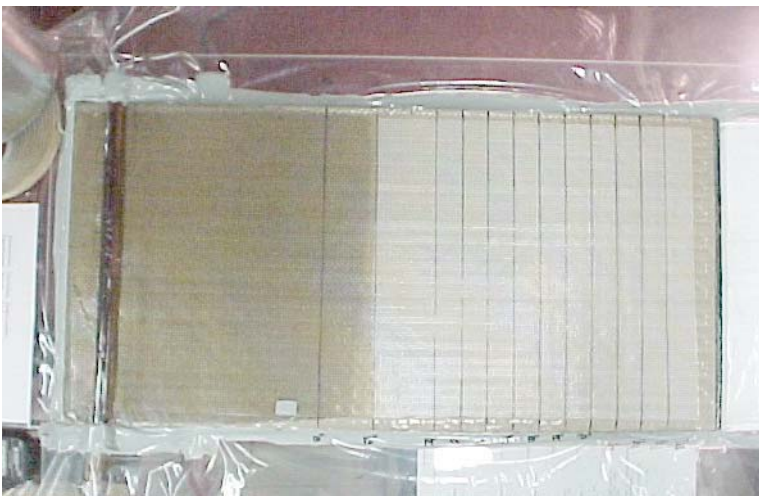
Figure 6.20: Top surface of stitched foam core preform with 12.7 mm stitch row spacing. Flow front is approximately 30.5 cm from injection edge
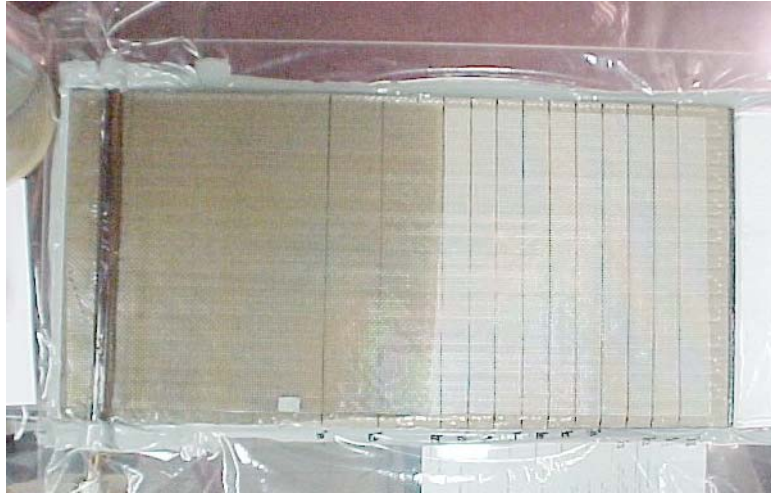
Figure 6.21: Top surface of stitched foam core preform with 12.7 mm stitch row spacing. Flow front is approximately 35.6 cm from injection edge
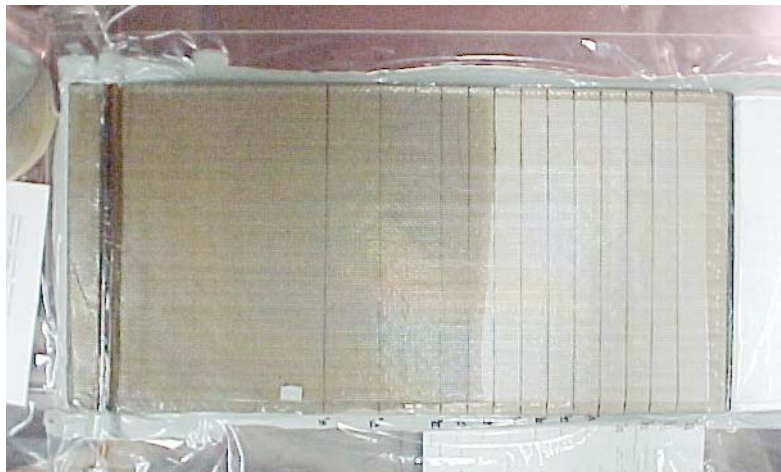
Figure 6.22: Top surface of stitched foam core preform with 12.7 mm stitch row spacing. Flow front is approximately 40.6 cm from injection edge

Figure 6.23: Top surface of stitched foam core preform with 12.7 mm stitch row spacing. Flow front is approximately 45.7 cm from injection edge

Figure 6.24: Top surface of stitched foam core preform with 12.7 mm stitch row spacing. Flow front is approximately 55.9 cm from injection edge

Figure 6.25: Top surface of stitched foam core preform with 12.7 mm stitch row spacing. Flow front is approximately 61.0 cm from injection edge

Figure 6.26: Top surface of stitched foam core preform with 12.7 mm stitch row spacing. The preform has been completely infiltrated
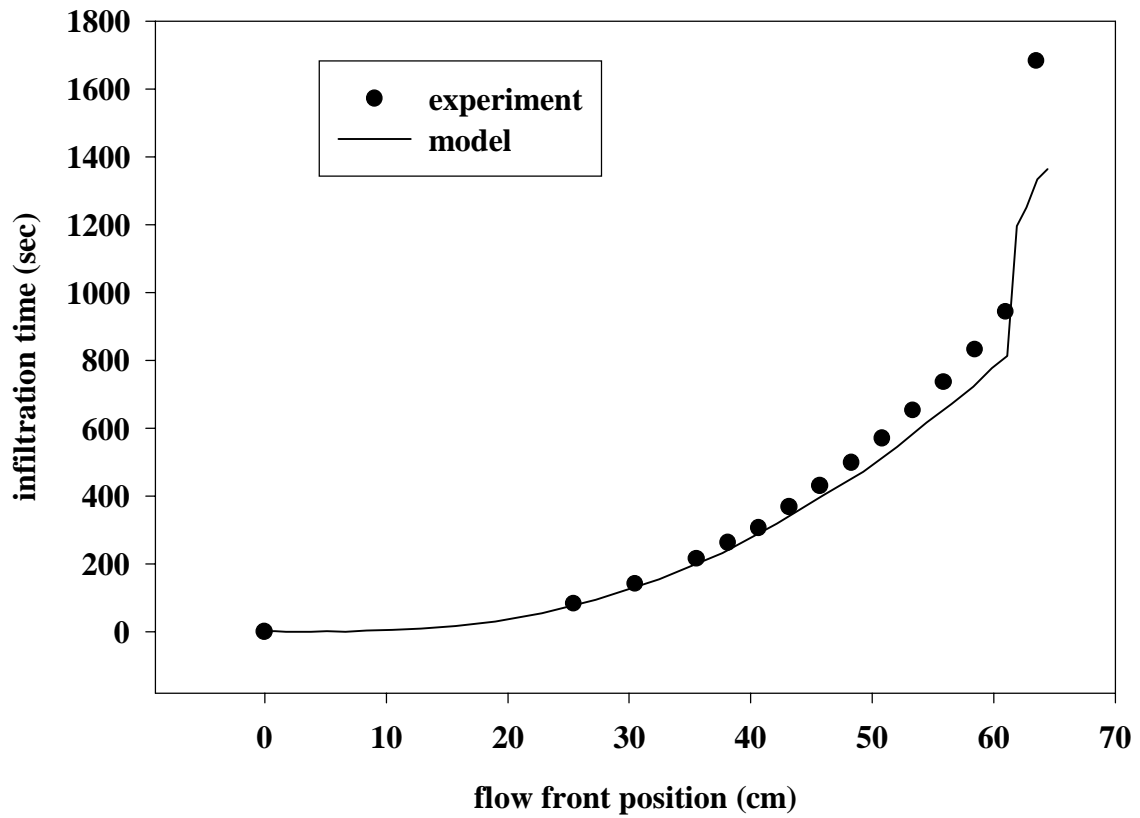
Figure 6.27: Measured and calculated flow along the top surface of the sandwich preform with 6.35 mm stitch row spacing
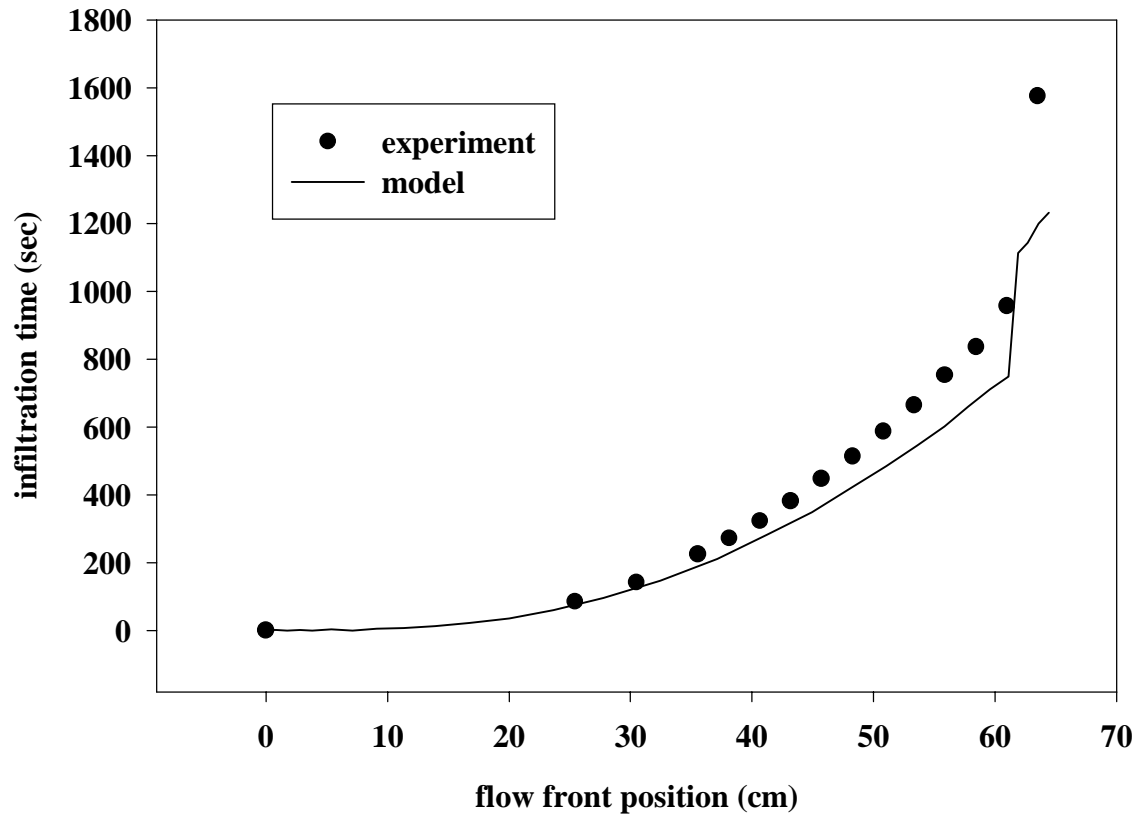
Figure 6.28: Measured and calculated flow along the top surface of the sandwich preform with 12.7 mm stitch row spacing
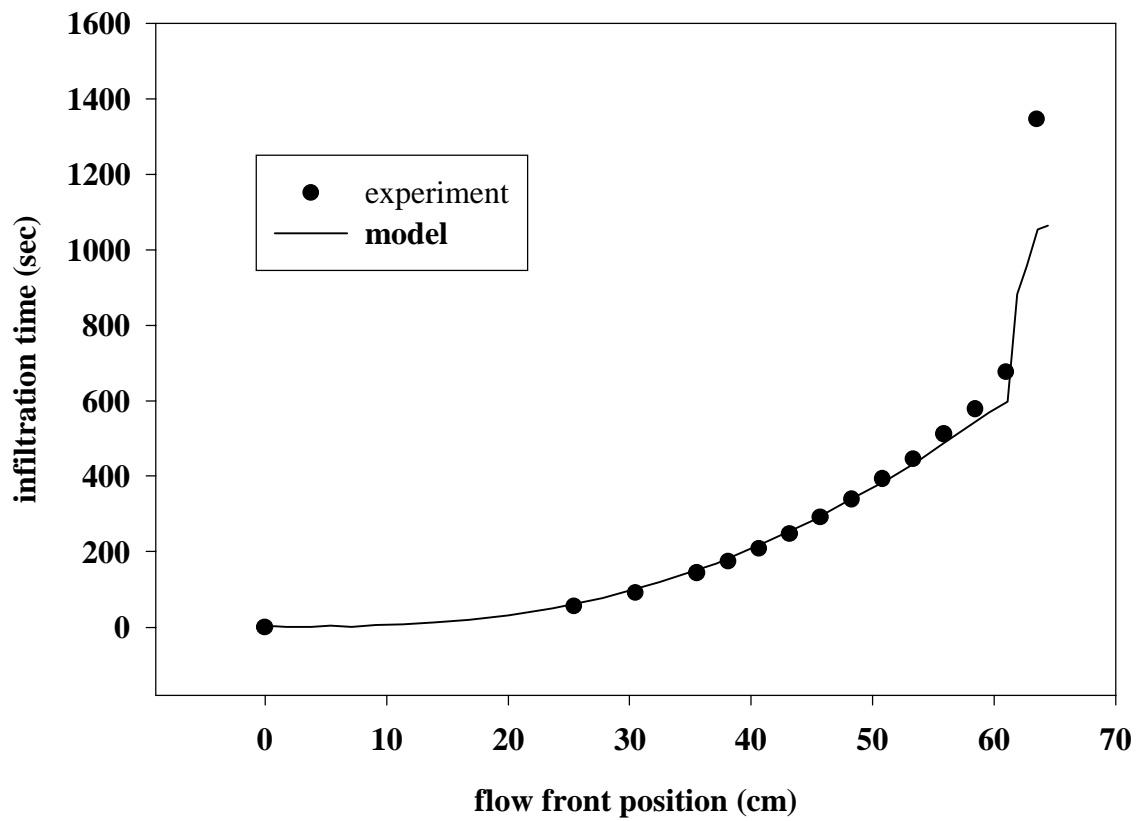
Figure 6.29: Measured and calculated flow along the top surface of the sandwich preform with 25.4 mm stitch row spacing

The lower face sheet resin infiltration patterns were observed quite different for the preforms with different stitch spacings. Figures 6.30 through 6.36 show the flow front progression along the bottom surface of the panel with the stitch row spacing of 6.35 mm, Figures 6.37 through 6.46 show the flow front progression along the bottom surface of the panel with the stitch row spacing of 12.7 mm, and Figures 6.47 through 6.51 show the flow front progression along the bottom surface of the panel with the stitch row spacing of 25.4 mm. Resin enters the lower face sheet through the vertical stitches and then permeates normal to the stitching direction to fill the areas between the stitches. This results in the resin flow along the stitching leading the flow in the regions between the stitches. For the preform of 6.35 mm stitch spacing, this lead-lag phenomenon is not evident and the flow pattern appears to be uniform due to the fact that the rows of stitches are close together and there is little lag in the area between the rows. When the row spacing increases, the lag length becomes larger and the infiltration pattern illustrates obvious nonuniformity.
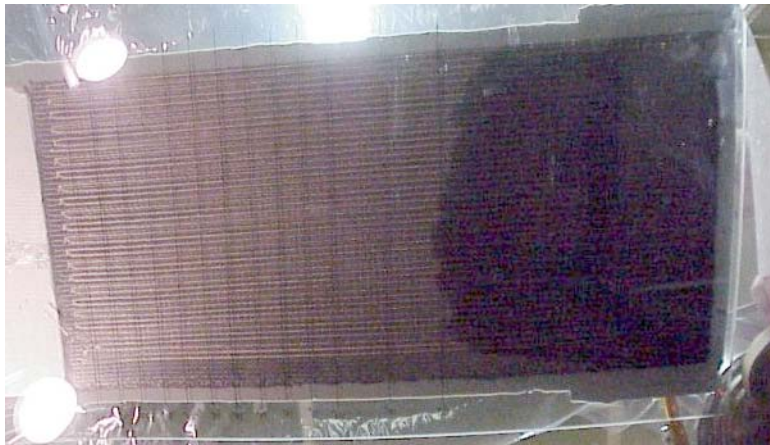

Figure 6.30: Bottom surface of stitched foam core preform with 6.35 mm stitch row spacing. Flow front is approximately 25.4 cm from injection edge
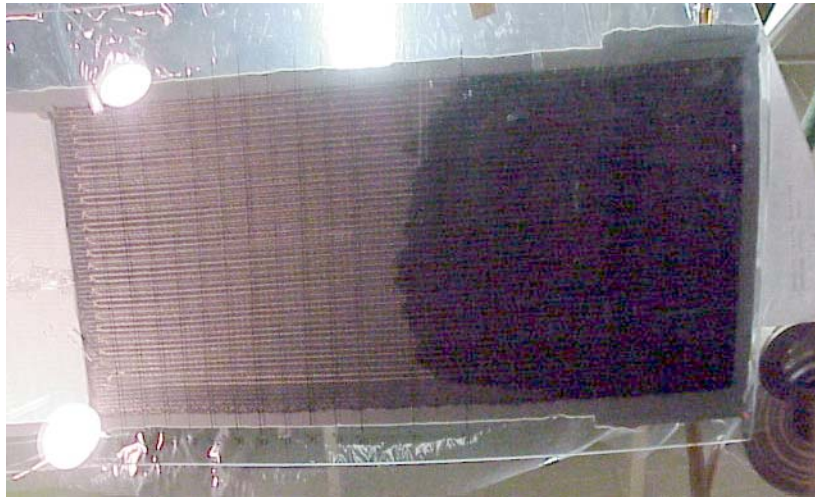
Figure 6.31: Bottom surface of stitched foam core preform with 6.35 mm stitch row spacing. Flow front is approximately 30.5 cm from injection edge
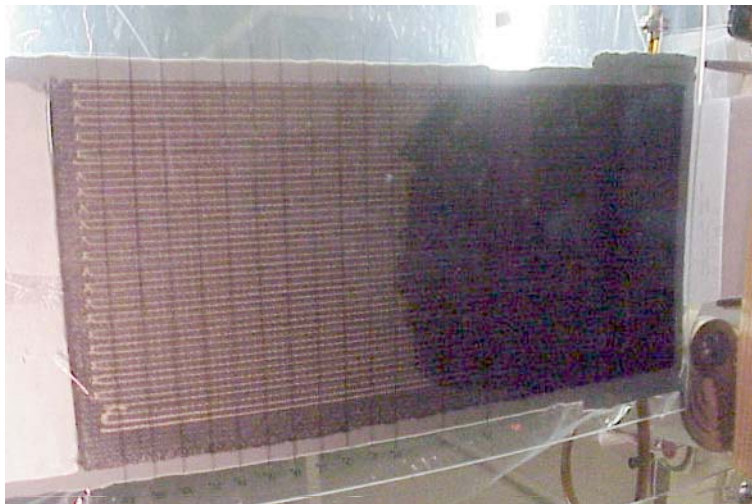

Figure 6.32: Bottom surface of stitched foam core preform with 6.35 mm stitch row spacing. Flow front is approximately 35.6 cm from injection edge
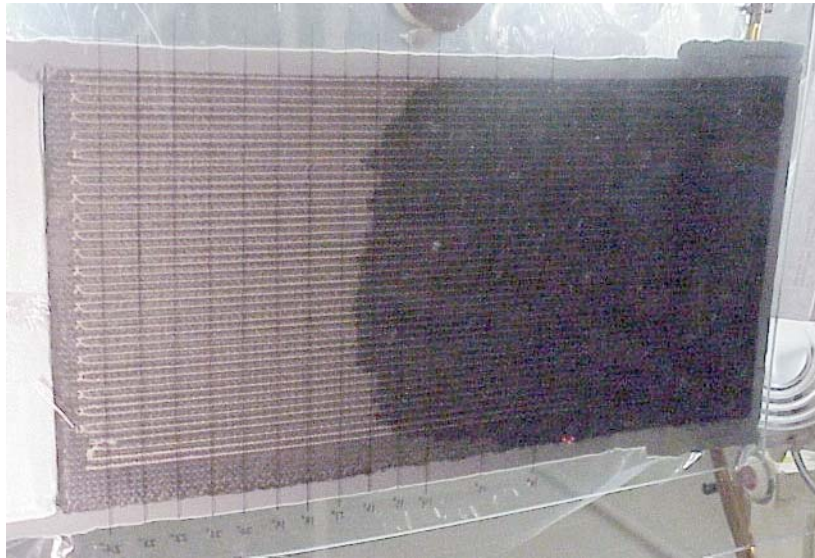
Figure 6.33: Bottom surface of stitched foam core preform with 6.35 mm stitch row spacing. Flow front is approximately 40.6 cm from injection edge
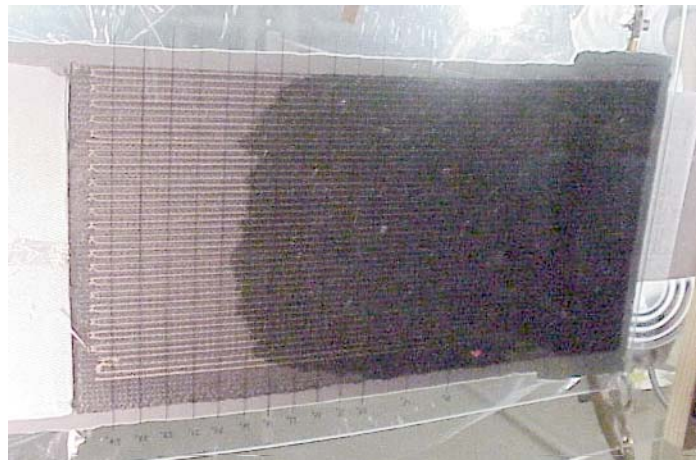

Figure 6.34: Bottom surface of stitched foam core preform with 6.35 mm stitch row spacing. Flow front is approximately 48.3 cm from injection edge
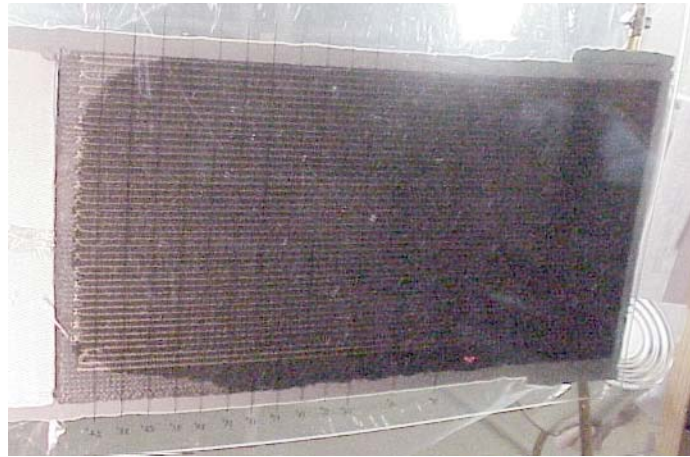
Figure 6.35: Bottom surface of stitched foam core preform with 6.35 mm stitch row spacing. Flow front is approximately 61.0 cm from injection edge
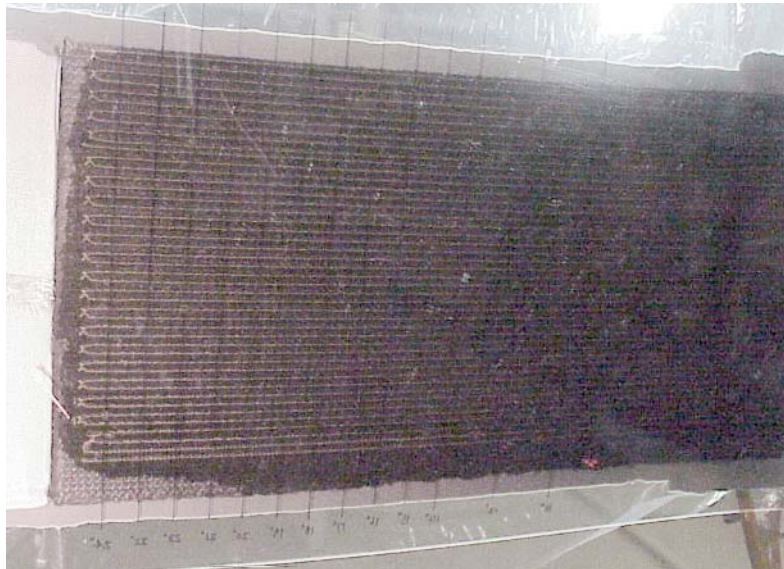

Figure 6.36: Bottom surface of stitched foam core preform with 6.35 mm stitch row spacing. The infiltration of the preform is nearly complete
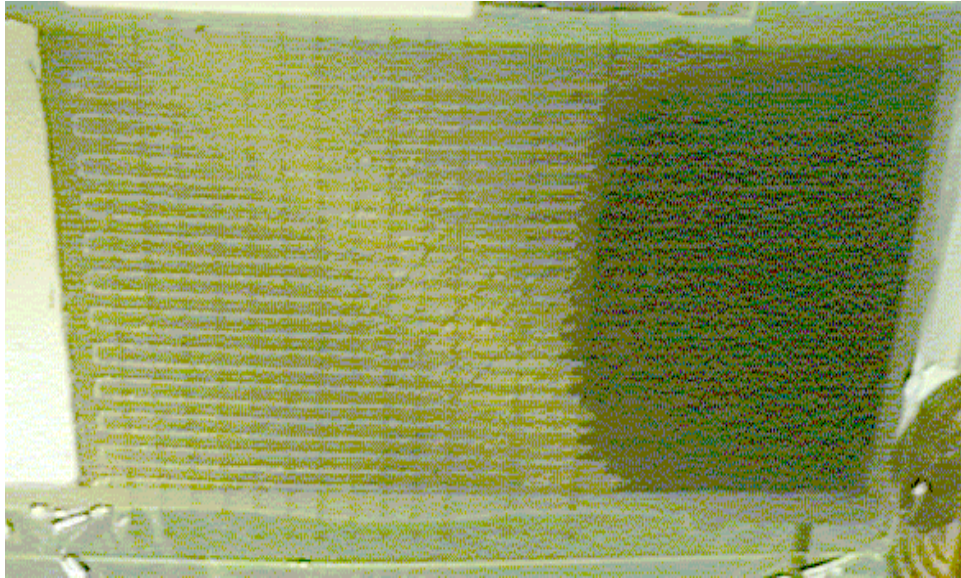
Figure 6.37: Bottom surface of stitched foam core preform with 12.7 mm stitch row spacing. Flow front is approximately 25.4 cm from injection edge

Figure 6.38: Bottom surface of stitched foam core preform with 12.7 mm stitch row spacing. Flow front is approximately 30.5 cm from injection edge

Figure 6.39: Bottom surface of stitched foam core preform with 12.7 mm stitch row spacing. Flow front is approximately 35.6 cm from injection edge

Figure 6.40: Bottom surface of stitched foam core preform with 12.7 mm stitch row spacing. Flow front is approximately 40.6 cm from injection edge

Figure 6.41: Bottom surface of stitched foam core preform with 12.7 mm stitch row spacing. Flow front is approximately 45.7 cm from injection edge
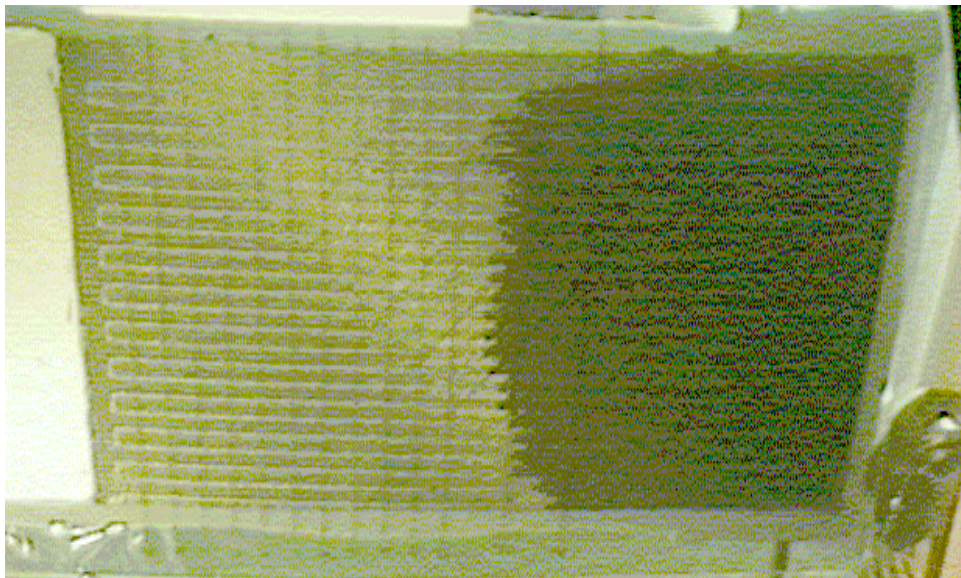

Figure 6.42: Bottom surface of stitched foam core preform with 12.7 mm stitch row spacing. Flow front is approximately 50.8 cm from injection edge
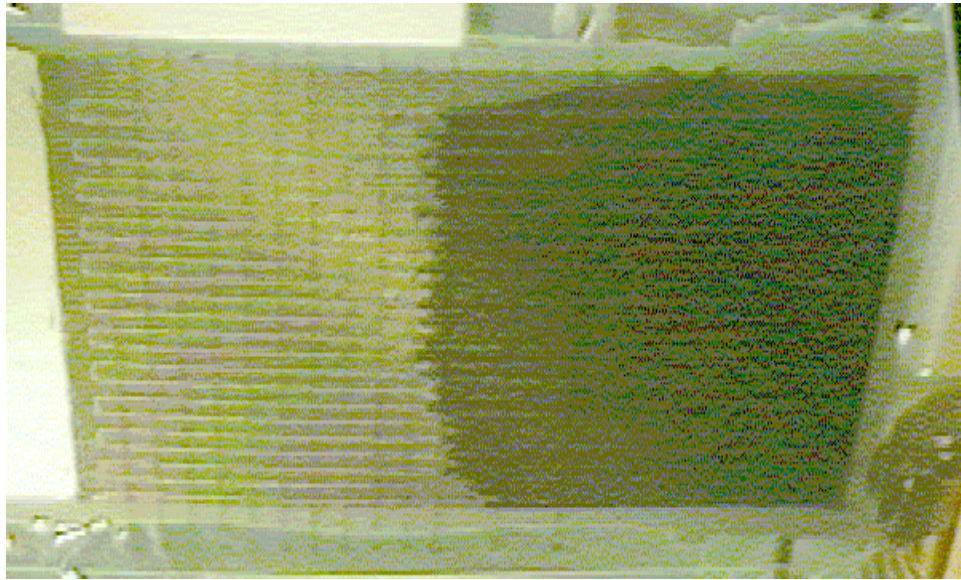
Figure 6.43: Bottom surface of stitched foam core preform with 12.7 mm stitch row spacing. Flow front is approximately 55.9 cm from injection edge
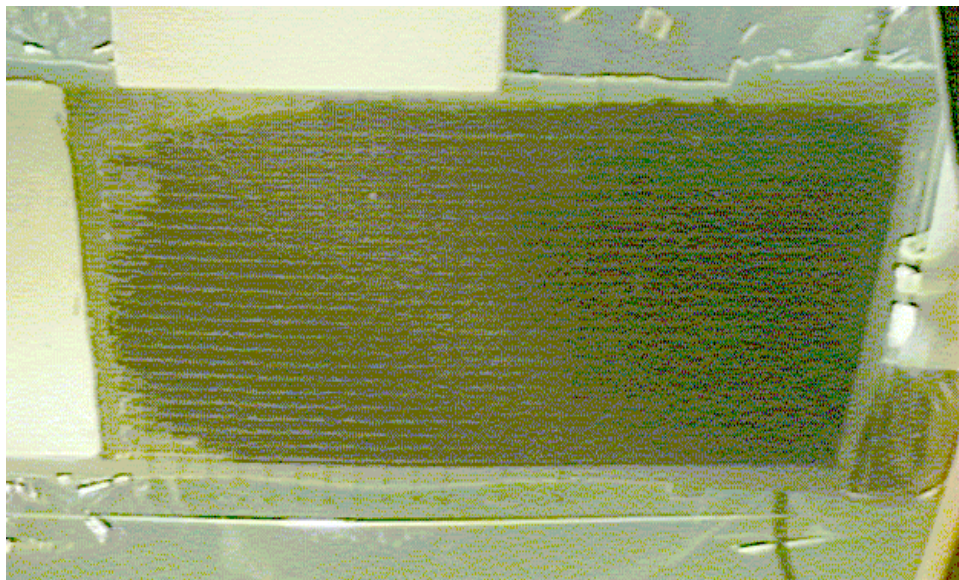
Figure 6.44: Bottom surface of stitched foam core preform with 12.7 mm stitch row spacing. Flow front is approximately 61.0 cm from injection edge
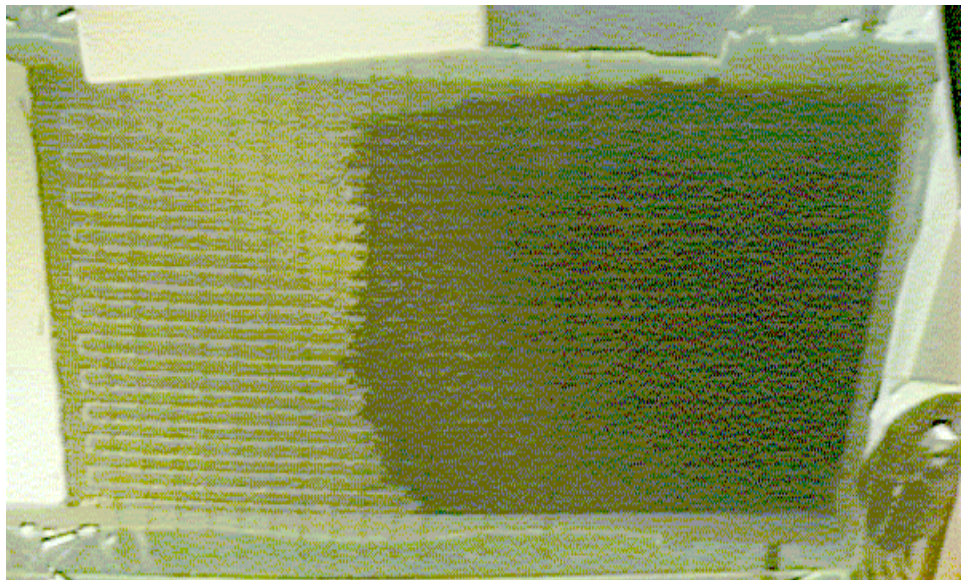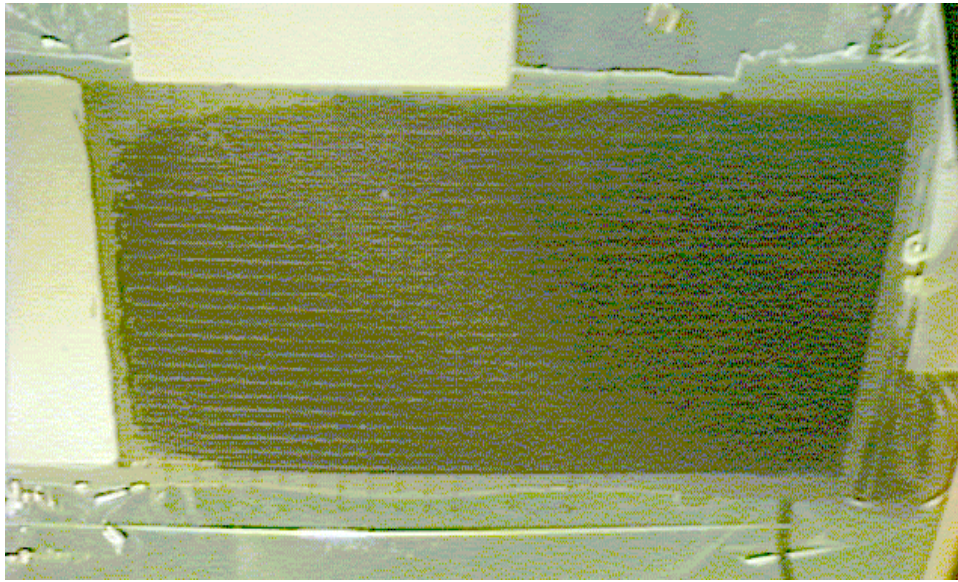
Figure 6.45: Bottom surface of stitched foam core preform with 12.7 mm stitch row spacing. Flow front is approximately 63.5 cm from injection edge
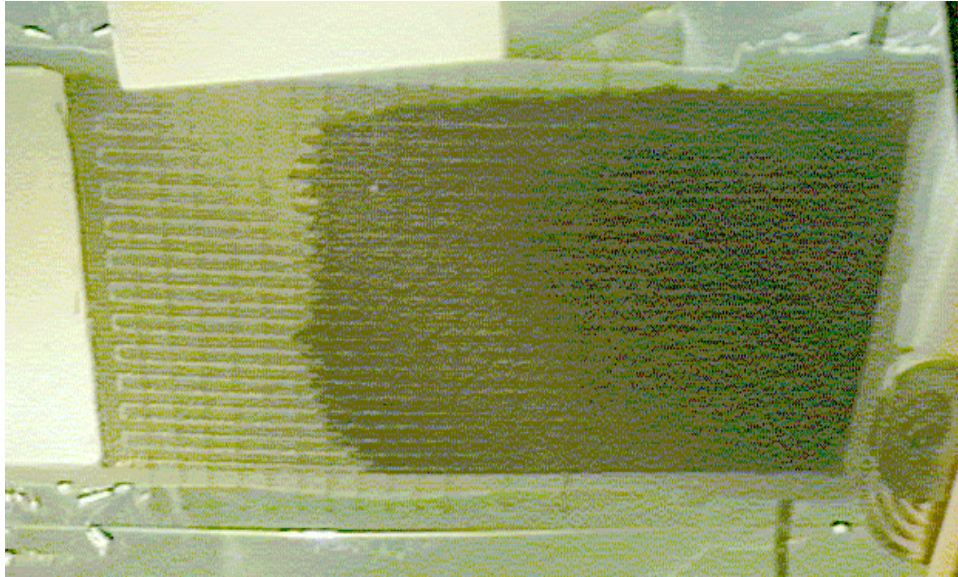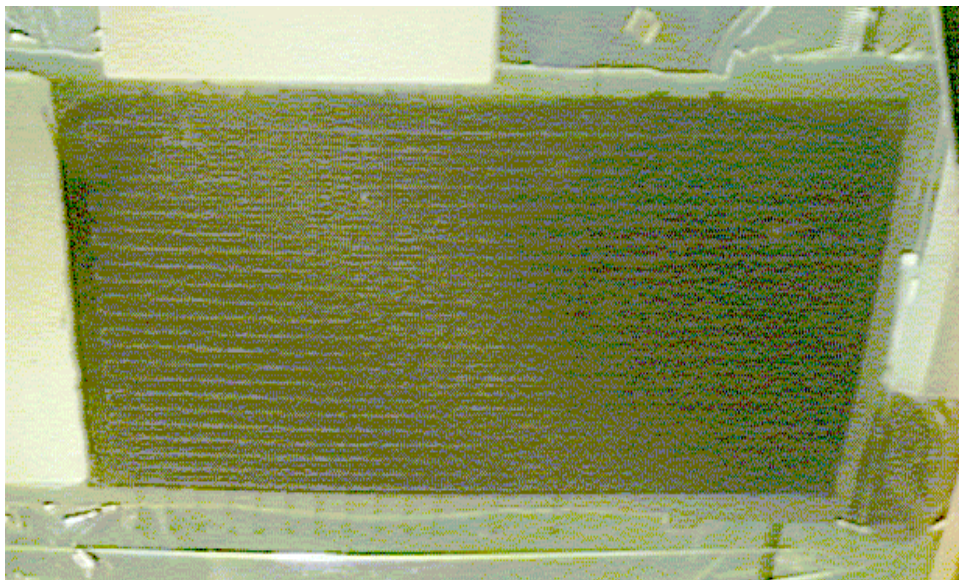

Figure 6.46: Bottom surface of stitched foam core preform with 12.7 mm stitch row spacing. The preform has been completely infiltrated
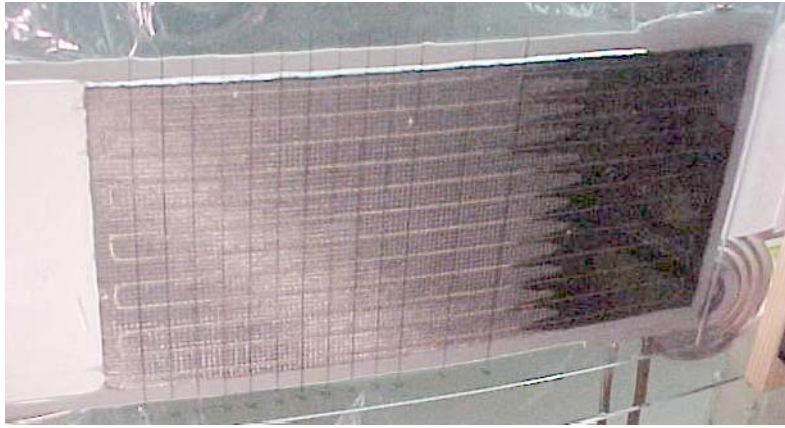
Figure 6.47: Bottom surface of stitched foam core preform with 25.4 mm stitch row spacing. Flow front is approximately 20.3 cm from injection edge

Figure 6.48: Bottom surface of stitched foam core preform with 25.4 mm stitch row spacing. Flow front is approximately 28.0 cm from injection edge
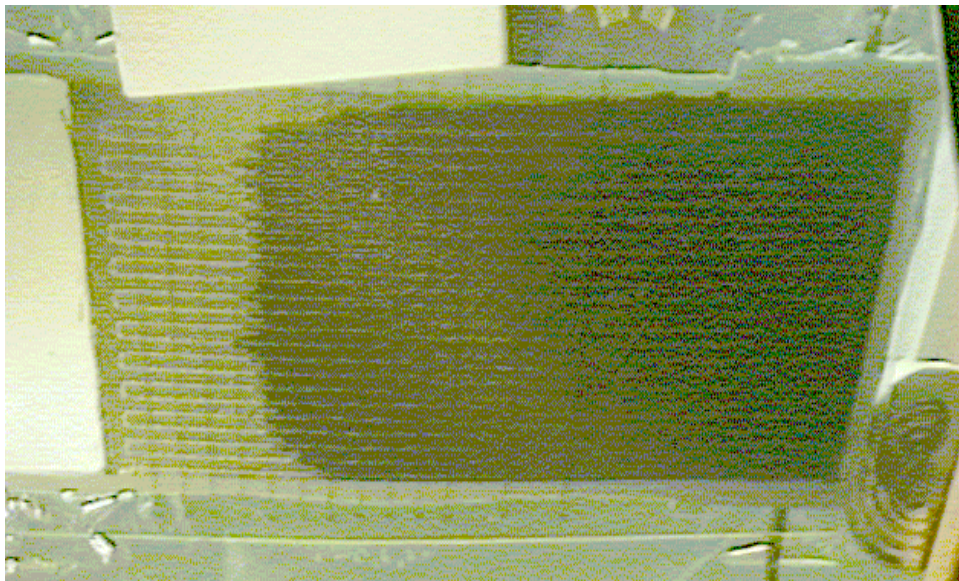
Figure 6.49: Bottom surface of stitched foam core preform with 25.4 mm stitch row spacing. Flow front is approximately 35.6 cm from injection edge
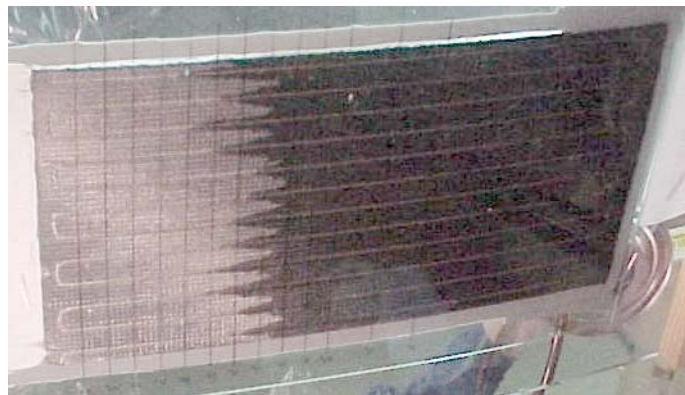
Figure 6.50: Bottom surface of stitched foam core preform with 25.4 mm stitch row spacing. Flow front is approximately 40.6 cm from injection edge
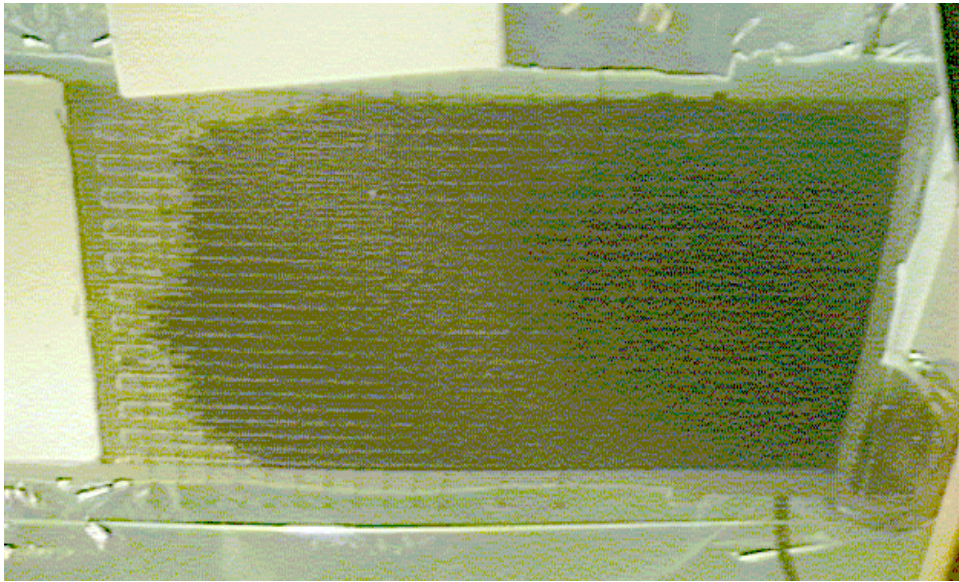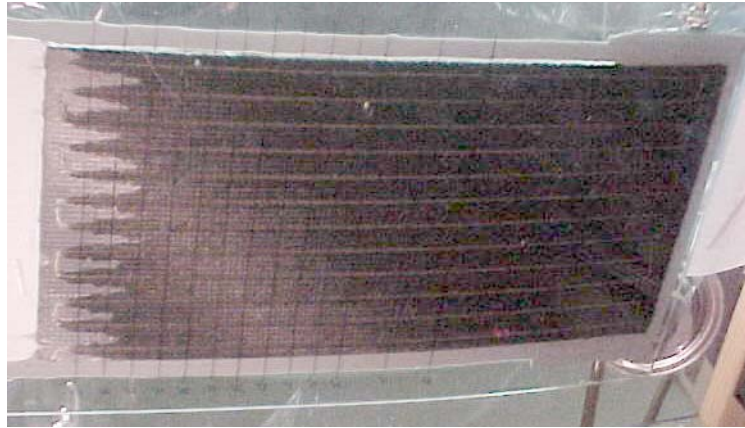
Figure 6.51: Bottom surface of stitched foam core preform with 25.4 mm stitch row spacing. Flow front is approximately 58.4 cm from injection edge
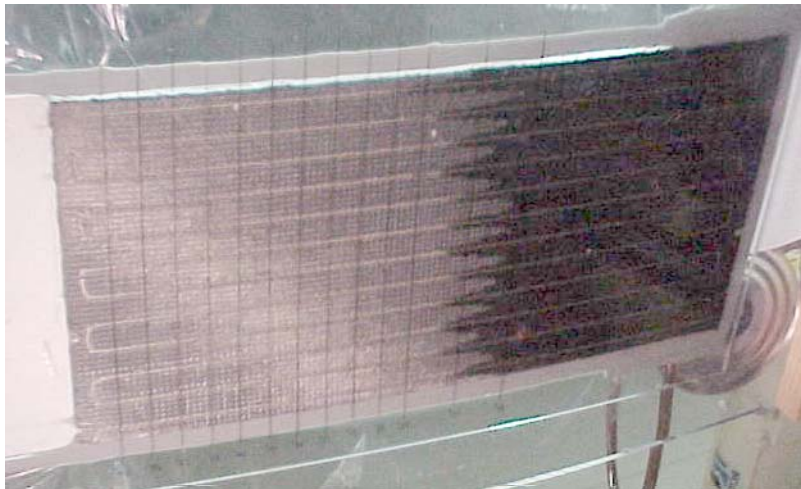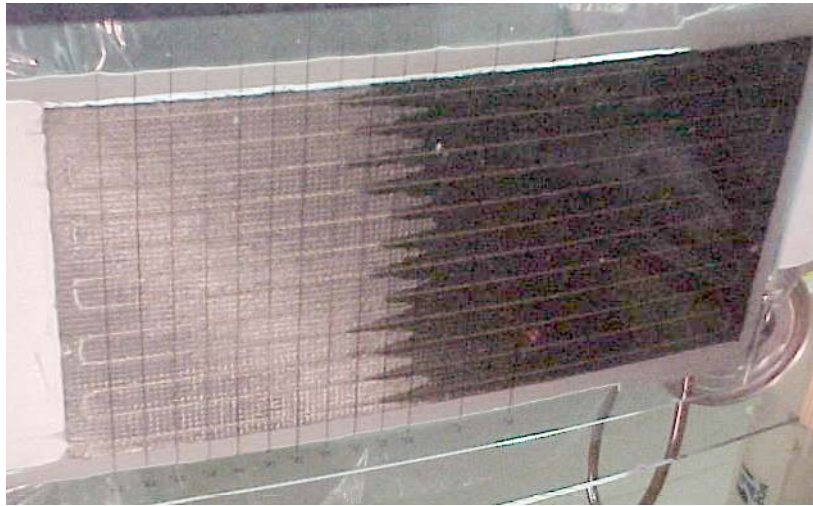
Figures 6.52 – 6.54 show the model predicted infiltration patterns in the lower face sheets of the three preforms. The model accurately predicted the resin infiltration patterns observed in the experiments. When the stitch row spacing increases, the flow front shape in the bottom face sheet becomes more nonuniform. Extreme nonuniformity of the flow front shape could result in the formation of voids (dry spots) during infiltration process. This void entrapment occurs because there is more than one flow front, and when these fronts meet up, they will coalesce forming voids via entrapment. The possible void locations on the bottom face sheet of the sandwich preform with the stitch row spacing of 25.4 mm are predicted as shown in Fig 6.55. Fig. 6.55 illustrates the flow front shapes on the bottom surface of the preform at different time. Note that there are some spots near the ends of the preform, which have different color from the area around. This indicates that the resin fills these locations from around. Therefore, the resin fronts meet at these locations and form voids via entrapment.

The measured and predicted total infiltration time for all the three preforms were compared in Table 6.3. Both the experiment and simulation show that the filling time increases with increasing stitch density. Initially one might assume that the preform with the highest stitch density will have the lowest infiltration time as a result of the large number of penetrations feeding resin to the lower face sheet. However, the panel with the highest stitch

Figure 6.52: Predicted flow front progression in the bottom surface of the stitched foam core preform with 6.35 mm stitch row spacing
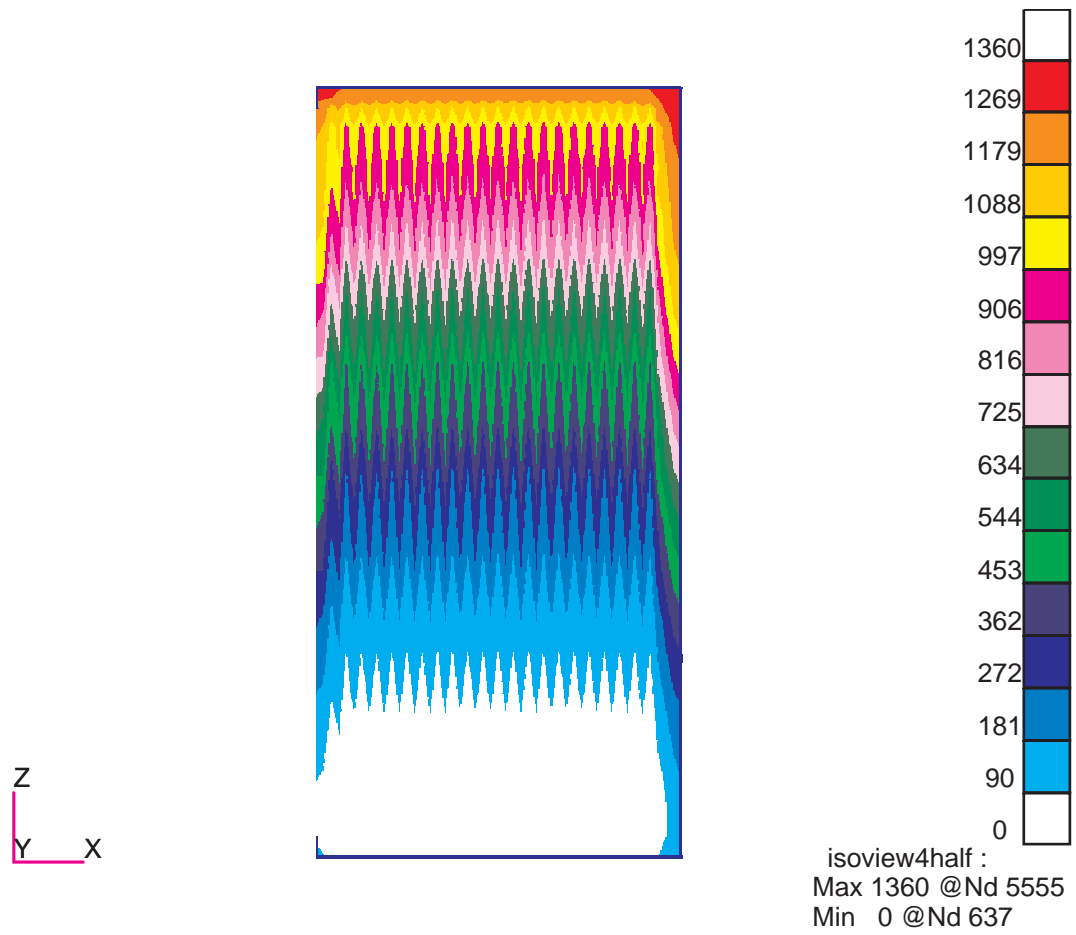
Figure 6.53: Predicted flow front progression in the bottom surface of the stitched foam core preform with 12.7 mm stitch row spacing
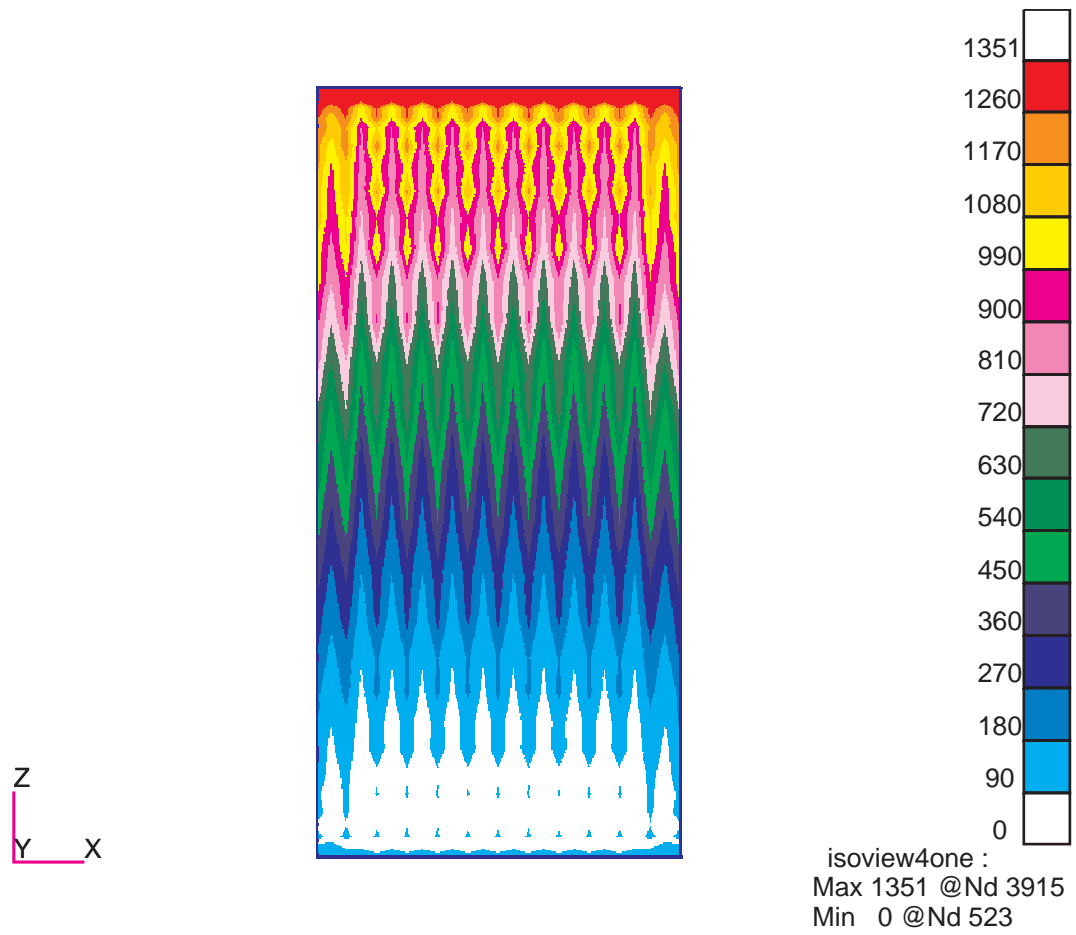
Figure 6.54: Predicted flow front progression in the bottom surface of the stitched foam core preform with 25.4 mm stitch row spacing
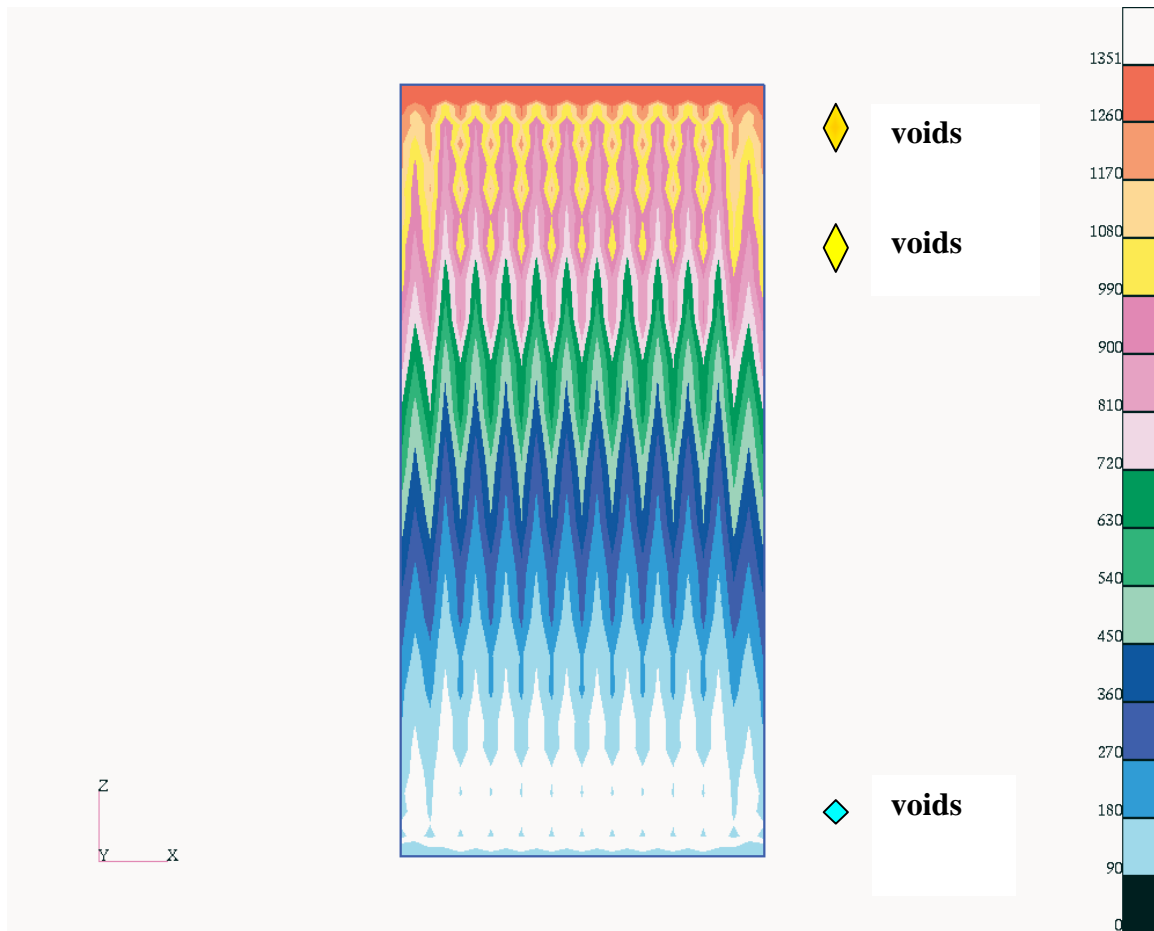
Figure 6.55: Predicted flow front progression in the bottom surface of the stitched foam core preform with 25.4 mm stitch row spacing. Note the voids near the ends of the preform

Table 6.3: Measured and predicted infiltration time

Stitch row spacing (mm)	Infiltration time (min)		
	Experiment measurements	Model prediction	% error
6.35	29.77	25.59	14.04
12.7	26.40	22.67	14.13
25.4	23.47	22.52	4.05

density also requires a greater volume of resin to fill the face sheets and the needle penetrations in the foam core, which increases the overall infiltration time. The prediction for the infiltration times underpredicted the measured filling time by 4 to 14%. Differences might be attributed to the inaccurate permeability values used for the carbon face sheets. The permeabilities of the Tenax multiaxial warp knit preform were taken from data obtained in a previous investigation for different stitch densities. On the other hand, the presence of the foam core might change the permeabilities of the carbon fabric. An accurate permeability model will be the subject of the further investigation.

6.5 Conclusions

Foam core sandwich preforms with through-the-thickness stitching were successfully resin infiltrated by the VARTM process. The through-the-thickness stitching permits resin infiltration of the entire preform by placing a single injection tube along one edge of the upper face sheet. The resin first travels along the distribution medium and through the thickness of the upper face sheet. Then the resin travels through the foam core along the stitch penetrations and into the lower face sheet. The stitch density affects both the resin infiltration patterns and the total infiltration time. The infiltration front was uniform across the width of the upper face sheet. However, the flow patterns on the lower face sheet are nonuniform and clearly depend on the stitching spacing. The flow front along the stitching leads the flow front between the stitches. The lag length increases with increasing stitch row spacing and results in more nonuniform infiltration pattern in the bottom face sheet of the sandwich preform. Extreme nonuniformity of the flow front shape could result in the formation of the voids (dry spots). The total infiltration time decreases when the stitch spacing increases.

The 3DINFIL computer code was used to simulate resin infiltration of the stitched foam core sandwich preforms. In the model, each row of stitches was described as a porous strip, in which the resin is only allowed to flow in through-the-thickness direction. The permeability of the strip was calculated analytically using a modified straight capillary model. Simulation results of the computer code were verified using flow visualization experiments. The model accurately predicted the resin infiltration pattern during VARTM of the stitched foam core preforms. The calculated total infiltration time underpedicted the measured filling time by 4 to 14%. The differences may be attributed to the permeability values that are input into the model for the carbon face sheets.

Chapter 7

Conclusions and Future Work

7.1 Conclusions

This investigation developed and verified a comprehensive Vacuum Assisted Resin Transfer Molding (VARTM) process simulation model. The model incorporates resin flow through the preform, compaction and relaxation of the preform, and viscosity and cure kinetics of the resin. The computer model can analyze the resin flow details, track the thickness change of the preform, predict the total infiltration time and final fiber volume fraction of the parts, and determine whether the resin could completely infiltrate and uniformly wet out the preform.

Flow of resin through the preform is modeled as flow through porous media. Darcy's law combined with the continuity equation for an incompressible Newtonian fluid forms the basis of the flow model. During the infiltration process, it is well accepted that the total pressure is shared by the resin pressure and the pressure supported by the fiber network. With the progression of the resin, the net pressure applied to the preform decreases as a result of increasing local resin pressure. This leads to the springback of the preform, and is called the springback mechanism. On the other side, the lubrication effect of the resin causes the rearrangement of the fiber network and an increase in the preform compaction. This

is called the wetting compaction mechanism. The thickness change of the preform is determined by the relative magnitude of the springback and wetting deformation mechanisms. In the compaction model, the transverse equilibrium equation is used to calculate the net compaction pressure applied to the preform, and the compaction test results are fitted to give the compressive constitutive law of the preform. The Finite Element/Control Volume (FE/CV) method is adopted to find the flow front location and the fluid pressure. The code features the ability of simultaneous integration of 1-D, 2-D and 3-D element types in a single simulation, and thus enables efficient modeling of the flow in complex mold geometries.

VARTM of two flat composite panels was conducted to verify the simulation model. The composite panels were fabricated using the SAERTEX multi-axial warp knit carbon fiber fabric and SI-ZG-5A epoxy resin. Panel 1 contained one stack of the carbon fabric, and Panel 2 contained four stacks of the fabric. The parameters verified included the flow front location and preform thickness change. For Panel 1, the flow front locations were accurately predicted while the predicted resin infiltration was much slower than measured for Panel 2. The disagreement is attributed to the permeability model used in the simulation, which failed to consider the interface flow in the unstitched preform containing more than one stack of the fabric under very low compaction force. The predicted transverse displacements agree well with the experiment measurement qualitatively, but not quantitatively. The reasons for the differences were discussed, and further investigations are recommended to develop a more accurate compaction model.

The simulation code was also used to investigate the VARTM of a new form of sandwich structure with through-the-thickness reinforcements, which is being considered for use in primary aircraft structure. The infiltration of three foam core sandwich preforms with different stitch densities was studied. The objective of the study was to determine whether the preforms could be completely infiltrated and how the stitch density affects the infiltration process. The visualization experiments were conducted to verify the simulation. The model accurately predicted the resin infiltration patterns. The calculated filling times underpredicted experimental times by 4 to 14%. The model revealed the resin flow details and found

that increasing the stitch spacing shortens the total filling time, but increases the nonuniformity of the flow front shape. Extreme nonuniformity of the flow front shape could result in the formation of the voids.

7.2   Future Work

Compaction and relaxation behavior of the preform was found to be very complex, nonlinear and loading history dependent. The compressive constitutive relation obtained by the compaction test conducted in the quasi-static state was found not accurate enough to model the compaction behavior of the preform during the VARTM process. Further investigations are recommended to find a more accurate constitutive law representing the compaction response of the preform. Based on this investigation, a more accurate compaction model should be developed to predict the thickness change of the preform during infiltration process quantitatively.

Bibliography

[1] Coulter J. P., Smith B. F., and S. I. Guceri (1988). Experimental and numerical analysis of resin impregnation during the manufacturing of composite materials. Proceedings of the American Society for Composites, Second Technical Conference, 209-217.

[2] Friedrichs B. and S. I. Guceri (1995). A Hybrid Numerical Technique to Model 3-D Flow Fields in Resin Transfer Molding Process. Polymer Engineering and Science 35(23), 1834-1851.

[3] Yoo, Y.-E. and W. I. Lee (1996). Numerical Simulation of the Resin Transfer Mold Filling Process Using the Boundary Element Method. Polymer Composites 17(3), 368-374.

[4] Wang H. P. and H. S. Lee (1989). Fundamental of Computer Modeling for Polymer Processing, Chapter 8, ed. C. L. Tucker. Hanser Publishers.

[5] Fracchia C. A., J. Castro and C. L. Tucker (1989). A Finite Element/Control Volume Simulation of Resin Transfer Mold Filling. Proceedings of the American Society for Composites, Fourth Technical Conference, 157-166.

[6] Bruschke M. V. and S. G. Advani (1990). A Finite Element/ Control Volume Approach to Mold Filling in Anisotropic Porous Media. Polymer Composites 11(6), 398-405.

[7] Lin R. J., Lee L. J., and M. J. Liou (1991). Nonisothermal Mold Filling and Curing Simulation in Thin Cavities with Preplaced Fiber Mats. International Polymer Processing 6(4), 356-369.

[8] Lin R. J., Lee L. J., and M. J. Liou (1993). Mold Filling and Curing Analysis in Liquid Composite Molding. Polymer Composites 14(1), 71-81.

[9] Calhoun R. D., Yalvac S., Wetters D. G., Wu C.-H., Wang T. J., Tsai J. S., and L. J. Lee (1996). Mold Filling Analysis in Resin Transfer Molding. Polymer Composites 17(2), 251-264.

[10] Lim S. T. and W. II Lee (2000). An Analysis of the Three-Dimensional Resin Transfer Mold Filling Process. Composites Science and Technology 60(7), 961-975.

[11] Phelan R. F. JR (1997). Simulation of the Injection Process in Resin Transfer Molding. Polymer Composites 18(4), 460-476.

[12] Chan A. W. and R. J. Morgan (1992). Sequential Multiple Port Injection for Resin Transfer Molding of Polymer Composites. SAMPE Quarterly. October 45-49.

[13] Kang M. K., Jung J. J., and W. II Lee (2000). Analysis of Resin Transfer Molding Process with Controlled Multiple Gates Resin Injection. Composites: Part A 31, 407-422.

[14] Kang M. K. and W. II Lee (1999). A Flow Front Refinement Technique for the Numerical Simulation of the Resin Transfer Molding Process. Composites Science and Technology 59, 1663-1774.

[15] Bruschke M. V. and S. G. Advani (1994). A Numerical Approach to Model Nonisothermal Viscous Flow through Fibrous Media with Free Surfaces. International Journal for Numerical Methods in Fluids 19, 575-603.

[16] Joshi S. C., Lam Y. C., and Liu X.-L. (2000). Mass Conservation in Numerical Simulation of Resin Flow. Composites: Part A 31, 1061-1068.

[17] Parnas R. S., J. G. Howard, T. L. Luce and S. G. Advani (1995). Permeability Characterization Part 1: A Proposed Standard Reference Fabric for Permeability. Polymer Composites 16(6), 429-445.

[18] Parseval Y. D., K. M. Pillai, and S. G. Advani (1997). A Simple Model for the Variation of Permeability due to Partial Saturation in Dual Scale Porous Media. Transport in Porous Media 27, 243-264.

[19] Babu B. Z. and K. M. Pillai (2001). New Experimental Findings on Resin-Impregnation Process for Woven, Stitched or Braided Fiber Mats in Liquid Composite Molding.

[20] Pillai K. M. and S. G. Advani (1998). A Model for Unsaturated Flow in Woven Fiber Preforms during Mold Fillings in Resin Transfer Molding. Journal of Composite Materials 32(19), 1753-1783.

[21] Pillai K. M. and S. G. Advani (1998). Numerical Simulation of Unsaturated Flow in Woven Fiber Preforms during the Resin Transfer Molding Process. Polymer Composites 19(1), 71-80.

[22] Williams C., J. Summerscales, and S. Grove (1996). Resin Infusion under Flexible Tooling (RIFT): a review. Composites Part A 27A, 517-524.

[23] Seemann W. H. (1990). U. S. Patent 4,902,215.

[24] Seemann W. H. (1991). U. S. Patent 5,052,906.

[25] Seemann W. H. (1994). U. S. Patent 5,316,462.

[26] Tari M. J., Imbert J.-P., Lin M. Y., Lavine A. S., and H. T. Hahn (1998). Analysis of Resin Transfer Molding with High Permeability Layers. Journal of Manufacturing Science and Engineering 120, 609-615.

[27] Hsiao K.-T., Mathur R., Advani S. G., Gillespie J. W. Jr., and B. K. Fink (2000). A Closed Form Solution for Flow during the Vacuum Assisted Resin Transfer Molding Process. Journal of Manufacturing Science and Engineering 122, 463-475.

[28] Sun X.-D., S. Li, and L. J. Lee (1998). Mold Filling Analysis in Vacuum-Assisted Resin Transfer Molding. Part I: SCRIMP Based on a High-Permeable Medium. Polymer Composites 19(6), 807-817.

[29] Rigas J. E., T. J. Mulkern, S. M. Walsh, and S. P. Nguyen (2001). Effects of Processing Conditions on Vacuum Assisted Resin Transfer Molding Process (VARTM). Army Research Laboratory Report ARL-TR-2480.

[30] Williams D. C., Grove M. S. and J. Summerscales (1998). The Compression Response of Fiber-Reinforced Plastic (FRP) Plates during Manufacture by the Resin Infusion under Flexible Tooling (RIFT) method. Composites: Part A 29A, 111-114.

[31] Kim R. Y., S. P. McCarthy, and J. P. Fanucci (1991). Compressibility and Relaxation of Fiber Reinforcements during Composite Processing. Polymer Composites 12(1), 13-19.

[32] Robitaille F. and R. Gauvin (1998). Compaction of Textile Reinforcements for Composites Manufacturing I: Review of Experimental Results. Polymer Composites 19(2), 198-216.

[33] Robitaille F. and R. Gauvin (1998). Compaction of Textile Reinforcements for Composites Manufacturing II: Compaction and Relaxation of Dry and H_2O- Saturated Woven Reinforcements. Polymer Composites 19(5), 543-557.

[34] Robitaille F. and R. Gauvin (1999). Compaction of Textile Reinforcements for Composites Manufacturing III: Reorganization of the Fiber Network. Polymer Composites 20(1), 48-61.

[35] Chen B., Cheng A. H.-D., and T.-W. Chou (2001). A Nonlinear Compaction Model for Fibrous Preforms. Composites: Part A 32, 701-707.

[36] Hammami A. and B. R. Gebart (2000). Analysis of the Vacuum Infusion Molding Process. Polymer Composites 21(1), 28-40.

[37] Han K., S. Jiang, C. Zhang, and B. Wang (2000). Flow Modeling and Simulation of SCRIMP for Composites Manufacturing. Composites: Part A 31, 79-86.

[38] MacRae J. D. (1994). Development and Verification of a Resin Film Infusion/Resin Transfer Molding Simulation Model for Fabrication of Advanced Textile Composites. Master thesis, Virginia Polytechnic Institute and State University.

[39] Caba C. A. (1998). Verification of a Three-Dimensional Resin Film Infusion Process Simulation Model. Master thesis, Virginia Polytechnic Institute and State University.

[40] Sayre J. (2000). Vacuum Assisted Resin Transfer Molding (VARTM) Model Development, Verification and Process Analysis. Ph.D. Dissertation, Virginia Polytechnic Institute and State University.

[41] Gutowski T. G., T. Morigaki, and Z. Cai (1987). The Consolidation of Laminate Composites. Journal of Composite Materials 21(172).

[42] Dave R., J. L. Kardos, and M. P. Dudukovic (1987). A Model for Resin Flow during Composite Processing: Part 1-General Mathematical Development. Polymer Composites 8(29).

[43] Brian W. Grimsley, Pascal Hubert, Xiaolan Song, Roberto J. Cano, Alfred C. Loos, and R. Byron Pipes (2001). Flow and Compaction during the Vacuum Assisted Resin Transfer Molding Process. Proceedings of 33rd International SAMPE Technical Conference.

[44] Lee W. I., A. C. Loos, and G. S. Springer (1982). Heat of Reaction, Degree of Cure, and Viscosity of Hercules 3501-6 Resin. Journal of Composite Materials 16(510).

[45] Castro J. M. and C. W. Macosko (1982). Studies of Mold Filling and Curing in the Reaction Injection Molding Process. AICheE Journal 28(2), 250-260.

[46] Reddy J. N. (1993). An Introduction to the Finite Element Method. McGraw Hill, Inc., New York.

[47] Stanley L. E., S. S. Gharpure, and D. O. Adams (2000). Mechanical Property Evaluation of Stitched Composite Sandwich Panels. International SAMPE Symposium and Exhibition, 45(2): 1650-1661.

[48] Loos A. C., R. C. Batra, R. Dean, A. C. Caba, and T. Knott (1998). Process Model Development / Residual Stress Model Development. Final Report Prepared for the Boeing Company. Virginia Polytechnic Institute and State University.

[49] Scheidegger E. Adrian (1960). The Physics of Flow through Porous Media. University of Toronto Press.

[50] Brian W. Grimsley, Pascal Hubert, Xiaolan Song, Roberto J. Cano, Alfred C. Loos, and R. Byron Pipes (2002). Effects of Amine and Anhydride Curing Agents on the VARTM Matrix Processing Properties. SAMPE Journal 38(4):8-15.

Vita

Xiaolan Song was born on Feburary 22, 1976 in Shehong, China. She attended Tsinghua University at Beijing, P. R. China from September of 1992 until July of 1997, receiving her Bachelor of Science Degree in Engineering Mechanics. Upon graduation, she entered the department of Engineering Science and Mechanics at Virginia Polytechnic Institute and State University, and received the Master of Science degree in September of 2000. On April 14, 2003, she successfully defended her dissertation, to earn a Doctor of Philosophy degree in Engineering Mechanics from Virginia Polytechnic Institute and State University.